Surface plasmons for enhanced mid-infrared graphene photodetection

A thesis submitted in fulfillment of the requirements for the degree of

Doctor of Philosophy

Jingyang Peng

BSc Physics – Qufu Normal University, China

MSc Physics – Nankai University, China

School of Science

College of Science, Engineering and Health

RMIT University

April 2019

I would like to dedicate this thesis to my beloved parents.

Declaration

I certify that except where due acknowledgement has been made, the work is that of the author alone; the work has not been submitted previously, in whole or in part, to qualify for any other academic award; the content of the thesis is the result of work which has been carried out since the official commencement date of the approved research program; any editorial work, paid or unpaid, carried out by a third party is acknowledged; and, ethics procedures and guidelines have been followed.

The electric field plots of Figure 3.10 have been provided by Dr. Benjamin P. Cumming.

Jingyang Peng

School of Science

College of Science, Engineering and Health

RMIT University, Melbourne, Australia

April 2019

Abstract

Information photonics, which deals with the manipulation, detection, generation and transmission of light across a broad wavelength range has undoubtedly shaped and transformed our daily life, from mobile and communication devices to computing and the internet. Although the research and application of photonic devices based on silicon and other semiconductor materials have shown potentials towards the next information revolution, several intrinsic limitations have shown up, resulting from the common drawbacks of semiconductors, such as large footprint, limited absorption bandwidth and complex and expensive manufacturing process. Therefore, the exploration of new material is highly demanded and the integration with other research fields, such as electronics, is crucial.

Integrated optoelectronics, which bridges optics and electronics through manipulating, detecting and generating optical signals with electronic signals, provides the ability to tackle some of the existing challenges, because it not only inherits the mature processing protocols and theories from well-developed integrated electronics but also assimilates advantages from optics. Among integrated optoelectronics devices, photodetectors, devices that transduce absorbed photons into measurable electrical signals, are ubiquitous. They are the key components for optical communications, imaging, security, night-vision, spectroscopy and motion detection. Current commercial photodetectors have thrived on the development of band theory and the maturity of semiconductor growth and manufacturing; however, current mid-infrared photodetectors are intrinsically limited by high dark current, low working temperature and responsivity and expensive cost resulting from the narrow band gap of semiconductor alloys and restrictive materials growth process. Nevertheless, the mid-infrared wavelength plays a crucial role in the applications of spectroscopy, security and industry, chemical and biological sensing. Therefore, exploration and investigation of novel materials for mid-infrared photodetection is critical.

Graphene, a one-atom-thick layer of sp2-bonded carbon atoms tightly packed in a hexagonal lattice, has shown potential as a substitute material for silicon for the next information revolution because of its extraordinary optical, electronic, mechanical and thermal properties. These

exceptional properties make it a promising candidate for a comprehensive range of applications, such as energy and storage, electronics, biomedical, flexible and wearables, photonics and optoelectronics. For example, the intrinsic surface plasmons based on a graphene platform surpass conventional plasmons because of its exceptional characteristics including tuneability, adjustability and relatively low dissipation, which implies that novel manufactured devices based on graphene surface plasmons can operate with low power consumption and driving voltage, small footprint and unrivalled speed. Moreover, the broadband absorption from UV to THz, ultrafast carrier mobility and tuneable Fermi level are prominent for mid-infrared photodetection.

Common mid-infrared photodetection focuses on wavelength; if other states of light, such as polarisation and phase could be detected at same time, detection bandwidth could be broadened, and detection functionality increased. Compared with wavelength detection, the detection of circular polarisation states is much less explored, especially at the mid-infrared wavelength range. Chirality, a geometric property of a structure, can be utilised to detect polarisation states of light due to the reason that chiral structures behave differently for incident light with different circular polarisation states.

The main objective of this thesis is to explore both theoretically and experimentally new types of mid-infrared graphene photodetectors enhanced by surface plasmons to address the main drawbacks of mid-infrared photodetection, such as low working temperature, low responsivity, high costs and lacking detection of polarisation states. The primary achievements are summarised as follows:

To simultaneously detect the spin angular momentum states of mid-infrared region from 3 to 5 μm, we employ a photodetection structure that contains a zigzag chiral metal structure and a graphene layer. The localised surface plasmons can be excited within this designed photodetection structure to enhance the light absorption of graphene layer and distinct the spin angular momentum states by producing photocurrent with different direction. First, to understand how the nano-engineered chiral structure affects spin angular momentum and the potential size of the circular dichroism, we performed a detailed theoretical simulation of the hybrid structure and optimised all geometric parameters. To unveil the physical mechanisms behind the high graphene absorption and circular dichroism, we performed an electric field analysis of the left-handed and right-handed structure with left circularly polarised (LCP) and right circularly polarised (RCP) light at resonant wavelength. It is shown that the hybrid structures with different chirality resonant

differently for the incident light with left-circular polarised state and right-circular polarised state respectively. In addition, the circular dichroism originates from the different absorption for LCP and RCP because the zigzag chiral structures resonant differently.

Instructed by these theoretical investigations, we fabricated mid-infrared graphene photodetectors that contain a zigzag gold structure, graphene layer and SiO_2/Si substrate, via steps including graphene transfer, photolithography, electron beam lithography and electron beam deposition. To qualitatively and quantitatively characterise our fabricated devices, we performed characterisations with SEM; the error of all measured structure sizes was less than 3.1% compared with designed values, which proves the high precision and uniformity of the fabricated devices. Moreover, to characterise the optical properties of our fabricated devices, FTIR measurements were taken. Considering that incident light is not pure plane wave and not all the light is vertically illuminated on the devices, the simulated and measured extinction spectra and circular dichroism spectra were highly consistent.

To electrically characterise these photodetectors, we conducted photocurrent measurements with our home-made photocurrent characterisation system. Results show that responsivity of 0.36 μA/W was achieved for left-handed (LHD) structure with LCP light illumination (0.33 μA/W for right-handed (RHD) structure with RCP light illumination) and the circular dichroism was approximately 75% both LHD and RHD structures. Most importantly, photocurrent with different circulation direction was produced when the incident light possessed different circular polarisation states, which is the novel contribution of our proposed simultaneous mid-infrared spin angular momentum photodetector.

Surface plasmons supported by a gold chiral structure possesses a parasitic absorption problem. Moreover, chirality originates from the chiral structure and the monolayer graphene only acts as a transport layer for the photodetector. Hence, to fully implement the potential of graphene and take advantage of its exceptional optical and electrical properties, we investigated a mid-infrared photodetector based on a grapheme nanomesh (GNM) structure. Tuneable intrinsic graphene plasmons is introduced to enhance light absorption (i.e., to enhance the responsivity of device). Further, band gap engineering was utilised to improve the electron-hole separation efficiency and restrict dark current.

To fully understand the impacts of geometric size and graphene properties on band gap engineering and intrinsic graphene plasmons and investigate whether they can work side by side, we performed a thorough theoretical analysis of this proposed GNM structure. First, we calculated the band gap of four representative types of GNM structures and their dependence on the period length of the unit cell and diameter of the hole. Then we investigated the impact of these two parameters on absorption magnitude of the GNM layer and resonant wavelength of photodetectors. The band gap energy of the GNM is larger than the energy of thermal fluctuation at room temperature implying the opened band gap can effectively restrict dark current. As it was smaller than graphene plasmons energy, this proves that incident mid-infrared light at resonant wavelength can be absorbed and excited electrons can jump from valence band to conduction band. Thus, this proves that band gap engineering and graphene plasmons can work side by side to improve performance.

Experimentally, GNM structures with period length of 100 nm and hole diameters from 40 nm to 80 nm were achieved. The geometric characterisation results show that the experimental size was within ± 5% of the design size. The resistance change under different back-gate voltages proved the tuneability of fabricated devices. Most importantly, the shifted resonant peaks shown on extinction spectra manifested the resonant graphene local surface plasmon supported by the GNM platform and the tunability of the Fermi level of the GNM layer.

In summary, this thesis demonstrates novel research on mid-infrared photodetection and offers two significant contributions. The first is the increase in detector functionality by simultaneously detecting the LCP and RCP light. The second is the improvement in performance of mid-infrared photodetectors by boosting responsivity and restricting dark current. A simultaneous mid-infrared spin angular momentum photodetector was proposed, theoretically investigated and experimentally achieved. Furthermore, a mid-infrared photodetector based on GNM was thoroughly explored. Band gap engineering and graphene plasmons were introduced and investigated and it was proved they can work side by side to improve responsivity and restrict dark current. Moreover, the device was fabricated and characterised according to geometric, electrical and optical aspects. All these contributions form the basis for future advances.

Acknowledgements

After spending almost four years, I am moving towards the completion of my PhD now. By recalling the past old days, it is always not easy to judge whether the decision was right or not. These four years is a rather long journey, I have gained a lot while I lost something as well during this path.

First of all, my thanks goes to my principle supervisor, Prof. Min Gu, who has provided me a wonderful research environment and outstanding resources, an exciting and challenging research project and all the instruction and supervision over the past four years. I really appreciate all the education he provided and the detailed conversation we shared about research which promotes me from a layman to a research starter. He acts as a mentor and guider to teach me how to cruise this PhD sea and how to do research although I didn't comprehend too much at that time. Due to the reason of scholarship, I was assigned a research project which is totally new for our group and I am the only person who is working on this research direction. At the beginning, I was disappointed and very unconfident considering the facts of new research field and especially my theory research background. With his mentoring, I gradually accepted the project and started to enjoy it. Right now, I have gained a lot of experience on nanofabrication and many knowledges on how to do research after been tortured for several years. And I feel grateful that I have been working on the graphene-related projects and had been one part of the CUDOS project. Thanks goes to Prof. Min Gu for guiding me along my PhD journey with wisdom and competence.

I would like to thank my associate supervisor Dr. Benjamin P Cumming, for the detailed instruction and discussion, the shared expertise and experience and his supervision all through the past four years. I started my PhD study without any experimental experience. So most of my experimental skills and habits are gained from him, especially the laser-related systems and compatible softwares. Now, I start to regrate that I did not spent enough time with him to learn how to build up laser systems. I was astonished at not only his rich experience and proficiency in facilities but also his understanding and opinion of physics. Two of the most important things that I have learnt from him are problem-solving ability and the way to analyse problem and verify with experiments. Furthermore, I also admire his attitude of research and enthusiasm of work. What he educated me and what I have learnt from him will certainly benefit me a lot.

I also would like thank Prof. Xiangping Li. Although we did not spend too much time together, his help and support did change my life four years ago. He is the first person I contacted for this PhD study and one of the main persons who decided to give me an offer. I really appreciate what he had done for me and I wish him all the best.

I thank Dr. Qiming Zhang, Dr. Xi Chen, Dr. Litty Thekkekara, Dr. Haoran Ren, Dr. Elena Goi, Dr.Brian Yang, Mr. Haitao Luan, Mr. Simone Lamon, Mr. Haoyi Yu, Mr. Baokai Wang, Mr. Le Gao, all currently from the Laboratory of Artificial Intelligence Nanophotonics (LAIN) at RMIT University, and some old friends, Dr. Muntasir Hossain, Dr. Zengji Yue, Dr. Haibo Ding, Dr. Gaolei Xue, Dr. Shuo Li. Thank all of them for the meaningful discussion, the help and support, the friendship and the past days we have experienced.

Since I started my PhD study at Centre for Micro-Photonics (CMP) Swinburne University and spent one year and three months, I met a lot of friends and colleagues there. There are too many to be listed here, so I just want to say thank you all for your help and support. All of you made my life colourful and my study easy. Here, I would like to mention a few of them, thanks to Ms. Barbara Gillespie and Ms. Jia Lou for their administrative work, thanks to Dr. Xijun Li for his professional technical support (actually he introduced me to the nanofabrication field and gave me a lot of professional trainings), and thanks goes to Mr. Riaan Lourens for his support and all the relax and happy casual talks.

I would like to thank all the friends and colleagues I met when I transferred to RMIT university. Thanks to Dr. Edwin Mayes, Dr. Matthew Field and all other staff from RMMF centre, and to Mr. Yuxun Cao, Dr. Jie Tian, Mr. Frank Antolasic and all other technical staff from MNRF and to Dr. Gediminas Gervinskas, Dr. John Zhu, Dr. Fatima Eftekhari and all other staff from MCN. I would like to thank Prof. Lan Wang and his student Mr. Cheng Tan as well. Thank them for the helpful discussion and some research facilities shared to me. There are a lot of friends I need to say thanks. Instead of mentioning everyone, here, I would like to express my thanks to all of you. Here, I would like to give a special thanks to my friend and schoolmate, Dr. Aizhu Wang. No matter what I had suffered both in life and research, she always believes me and encourages me. She is kind, enthusiastic, diligent and trustworthy. Sometimes, she like the navigation light which guides me towards the right end of one journey. I'm proud of what she has achieved now. I sincerely wish her all the best.

Finally, the biggest and the most special thanks go to my big family and upcoming small family. Thank my parents and sister for their support and understanding for my endless schooling time, especially these four years I spend abroad. All the love, care, support, help and understanding from family members are the origins of strength, faith and confidence, without which I would not achieve what I have now.

Jingyang Peng

Melbourne, Australia

13th March 2019

Table of contents

List of abbreviations

1D	One-dimensional
2D	Two-dimensional
3D	Three-dimensional
AFM	Atomic force microscope
CD	Circular dichroism
CDA	Coupled dipole approximation
CMOS	Complementary metal–oxide–semiconductor
CVD	Chemical vapour deposition
DFG	Difference frequency generation
DFT	Density functional theory
E-beam	Electron beam evaporation
EBL	Electron beam lithography
EBPG	Electron beam pattern generator
FEM	Finite element method
FOM	Figures of merit
FTIR	Fourier-transform infrared
GNM	Graphene nanomesh
GNR	Graphene nanoribbon
GQD	Graphene quantum dots
h-BN	Hexagonal Boron Nitride

IR	Infrared
LCP	Left-circular polarised
LED	Light emitting diodes
LH	Left-handed
MIR	Mid-infrared
NDFG	Non-collinear Difference Frequency Generator
PV	Photovoltaic
PVD	Physical vapor deposition
FET	Field effect transistor
PTE	Photo-thermoelectric
PB	Photo-bolometric
R	Responsivity
RCP	Right circular polarised
RH	Right-handed
RIE	Reactive ion etching
SPP	Surface plasmon polariton
SEM	Scanning electron microscope
TMDCs	Transition metal dichalcogenides

Chapter 1

Introduction

1.1 Information photonics

Information photonics, including sensing, imaging, storage, interconnects, switching and communications, plays a vital role in daily life. It possesses the ability to collect and transmit information of things. In our information society, how to efficiently collect, process and transmit signals is very important, both for military and civil applications. For example, sensors installed in the airport and other public buildings are the key to enable explosive detection, while the LIDAR system installed on the car is very helpful to lower road fatalities and reduce the accidents. Thus, information photonics contributes to the convenience, safety and efficiency.

Although the electronics that have been developed based on semiconductors has evolved the way we live, there are several problems in communication and computing. However, optics has the potential to solve some of these, due to its abilities, including crosstalk-free interconnects with originally unlimited bandwidth, long-distance data transmission without distortion, parallelism and efficient algorithm implementation, such as the Fourier transformation[1].

Thus, integrated optoelectronics, the combination of electronics and optics has solved many pressing issues. It offers a very good means of gaining information and possesses both the power of electronics and the high bandwidth, low loss and other advantages of optics.

Over the past few decades, integrated optoelectronics has greatly influenced both the academic and industrial worlds and daily life via the development and study of semiconductors (see figure 1.1). This intriguing research area bridges the fields of photonics and electronics by utilising the electronic signals to detect, source and control light. The core of optoelectronics devices that are mostly based on semiconductors and semiconductor compounds is the conversion between photons and electrons via photons absorption and emission from the platform materials. According to their function, optoelectronics devices include those that emit light (Light emitting diodes (LEDs) and light bulbs), channel light (fibre optic cables), detect light (photodiodes and photoresistors), or are controlled by light (optoisolators and phototransistors).

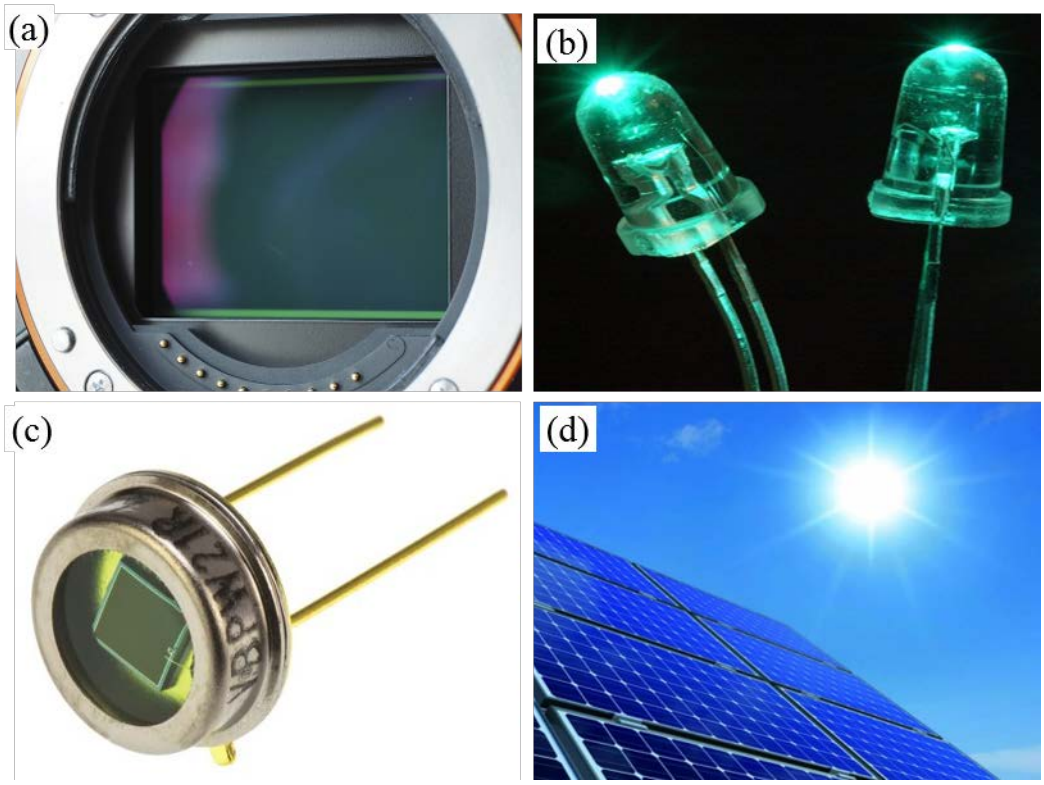

Figure 1.1 Macroscopic optoelectronic devices. (a) Complementary metal–oxide–semiconductor (CMOS) image sensor. (b) Light emitting diodes (LEDs). (c) Visible light Si photodiode. (d) Solar cell panel.

1.2 Mid-infrared photonics

Spanning the spectral range of 2-20 μm, the mid-infrared (MIR) has a crucial role in the application of spectroscopy, security and industry, chemical and bimolecular sensing and

materials inspection, as it contains information of the most common molecular vibrations[2] (see Figure 1.2). In addition, the two atmospheric transmission windows of 3-5 μm and 8-13 μm are also very important for industrial and atmospheric applications, such as security detection and remote sensing[3], because these electromagnetic spectra can transmit through the atmosphere without too much loss. However, the MIR has been a challenging spectral region for photodetectors, because the narrow-bandgap materials used for photodetection are intrinsically noisy and easy to subject to the temperature effect due to low photon energy. Hence, research on high-quality mid-infrared photodetectors is promising and important. Currently, most of the mid-infrared photodetectors are made with II-VI or III-V alloy; the drawbacks are that either the materials are hazardous, or the devices require low working temperature.

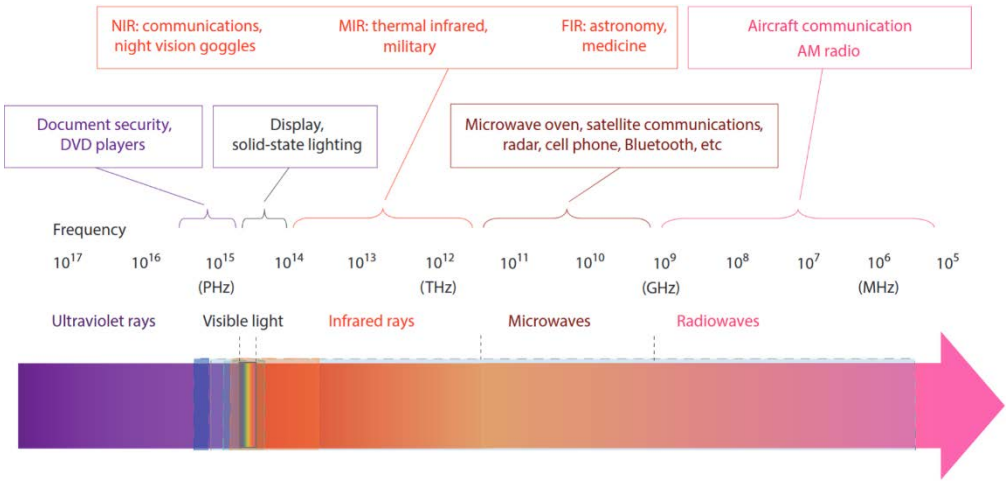

Figure 1.2 Electromagnetic spectrum and related applications for different spectral ranges. Image adapted from [4].

1.3 Photodetectors

Among the many optoelectronics devices, photodetectors, which range from the lowly sensors on automatically opening doors, to TV receivers and the CCD in a camera, to the far-infrared cell on an astronomical satellite, are one of the most ubiquitous types of technology. They are used to transduce absorbed photons into a measurable electrical signal; hence, they are key components for optical communications, imaging, security, night-vision, spectroscopy and motion detection.

1.3.1 Types and figures of merit

Two typical device architectures of photodetectors are field effect transistors (FETs) and Photodiodes (see figure 1.3). For the FETs, there have three terminals, source, drain and gate. While an external bias is added between source and drain terminals to drive current circulate through the device and separate the photogenerated electron-hole pairs, the gate terminal which is normally separated with an insulating layer is utilised to modulate the channel conductivity via field effect.

Different with FETs, a photodiode is based on a PN junction or PIN structure. A built-in electric field develops in the junction area/depletion region that between a p-doped and n-doped semiconductor due to the equilibrium between the diffusion of electrons and the static charge of the lattice ions[5]. The electron-hole pair occurs at the junction region when a photon with sufficient energy strikes and then can be separated due to the built-in electric field, producing a current without any external applied bias. The total current produced for both these two architectures is the sum of the dark current that is generated without light and photocurrent, hence the dark current must be minimized to improve the device quality.

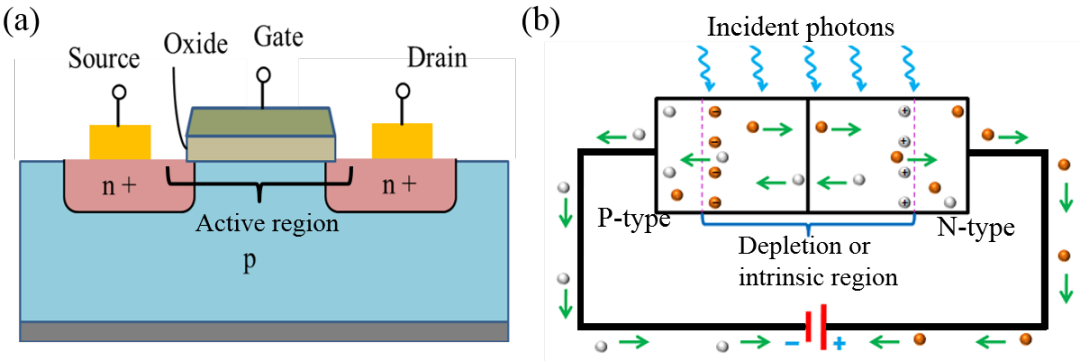

Figure 1.3 (a) Schematic of a field effect transistor (FET) type photodetector. (b) Schematic of a PN or PIN photodiode type photodetector.

In order to characterise the performance of one specific photodetector, firstly, we need to introduce some terminologies and its basic physical mechanism.

Assuming the incident light, with a photon energy E_{ph}, photon power P_{in} and light intensity I_0, impinges on the photodetector. The corresponding photo flux is $\Phi_{in}= P_{in}/ E_{ph}$, and the absorbed photon flux can be expressed as $\Phi_{abs}= \Phi_{in}A_{abs}$, with A_{abs} signify the absorbed fraction. However,

when there is no incident radiation, the photocurrent is defined as dark current I_{dark}. The external quantum efficiency (EQE) is used to describe the efficiency of incident light utilization. Hence, it's defined as the ratio of photocurrent I_{ph} (the discrepancy between current under and without illumination) and $q\Phi_{in}$.

$$\mathrm{EQE} = \frac{I_{ph}}{q\Phi_{in}} = \frac{h\upsilon}{q}\frac{I_{ph}}{P_{in}} \tag{1.1}$$

The counterpart of EQE is internal quantum efficiency (IQE) which is defined in a similar way except with the consideration of absorbed photon flux.

$$\mathrm{IQE} = \frac{I_{ph}}{q\Phi_{abs}} \tag{1.2}$$

The most important and commonly used figure of merit characterizing the photodetector's photorespond ability is responsivity, giving in the below form.

$$\mathrm{R} = \frac{I_{ph}}{P_{in}} \tag{1.3}$$

where R has the unit of A/W[6]. Another very important figure of merit is the response time τ corresponding to the duration time between photocurrent emerges and light impinges on the photodetector. And the response time limited bandwidth of the photodetector is given by[7]

$$\mathrm{f} = 3.5/2\pi\tau \tag{1.4}$$

Basically, the above parameters are most commonly used figure of merits to identify the photodetector. But in order to further represent the ability to detect radiation signal from noise, we can introduce another parameter detectivity (D)[8] that give in the below form.

$$\mathrm{D} = \frac{I_{ph}}{I_0\sqrt{2qI_{dark}}} \tag{1.5}$$

1.3.2 Disadvantages of current photodetectors

Photodetectors are usually wavelength specific; that is devices or constituent materials are chosen to work in a specific wavelength region. The two major working spectra for photodetectors are visible to near infrared and mid-infrared to far infrared. Silicon is the most

commonly used semiconductor material for photodetectors operating in the Vis-near IR spectra due to its complementary metal-oxide-semiconductor transistor (COMS) compatible advantage. However, silicon-based technology has its limitations[5]. According to band theory, silicon is an indirect bandgap semiconductor, with a bandgap of about 1.13 eV. This indirect band gap leads to two major intrinsic drawbacks: it reduces the efficiency of charge carriers' separation, which lowers responsivity across the entire visible part of the spectrum, and silicon-based photodetectors can only detect photons up to about 1100 nm due to the bandgap of 1.13 eV. This prevents silicon photodetectors from application in telecommunication and night vision. Moreover, the light penetration depth is very shallow (within 1 μm) for the photon of short wavelength (see Figure 1.4). Therefore, the generated charge carriers are easily affected by surface defects or surface states, which attenuate sensitivity per impinging photon. Finally, silicon is not suitable for the wearable or flexible devices because of its brittle nature.

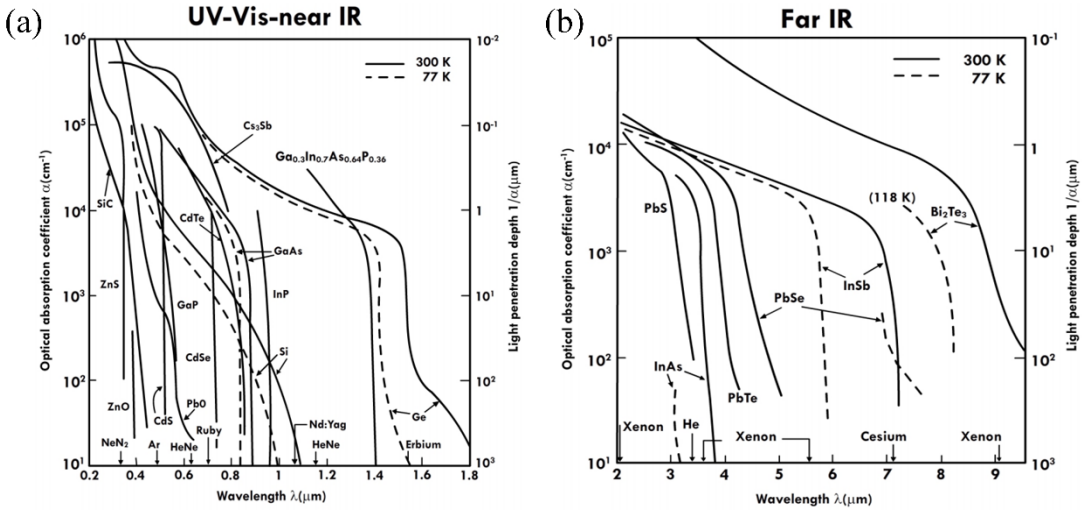

Figure 1.4 Optical absorption coefficients and light penetration depth for different semiconductors. (a) Optical absorption coefficients and light penetration depth for different semiconductors as a function of wavelength from UV to near infrared region. (b) Optical absorption coefficients and light penetration depth for different semiconductors as a function of wavelength at mid-infrared region. Images adapted from [9].

Regarding the mid-IR to far-IR spectrum, the choice of photodetection materials is more complex. The band gaps of the semiconductors or alloys need to be small enough compared with the energy of the incident photons; for instance, germanium-based photodetectors[10] have been studied and investigated for telecommunication wavelength applications because of their sizeable absorption coefficient and possible integration with silicon technology.

Furthermore, the II-VI group and IV-VI group compounds have also been investigated for infrared photodetection applications.

Type			Detector	Spectral response (μm)	Operating temperature (K)
Thermal type	Thermocouple · Thermopile Bolometer Pneumatic cell Pyroelectric detector		 Golay cell, condenser-microphone PZT, TGS, $LiTaO^3$	Depends on window material	300 300 300 300
Quantum type	Intrinsic type	Photoconduc-tive type	PbS PbSe InSb HgCdTe	1 to 3.6 1.5 to 5.8 2 to 6 2 to 16	300 300 213 77
		Photovoltaic type	Ge InGaAs Ex. InGaAs InAs InSb HgCdTe	0.8 to 1.8 0.7 to 1.7 1.2 to 2.55 1 to 3.1 1 to 5.5 2 to 16	300 300 253 77 77 77
	Extrinsic type		Ge : Au Ge : Hg Ge : Cu Ge : Zn Si : Ga Si : As	1 to 10 2 to 14 2 to 30 2 to 40 1 to 17 1 to 23	77 4.2 4.2 4.2 4.2 4.2

Figure 1.5 Types of infrared photodetectors and their characteristics. Image adapted from [11].

However, the main drawbacks of mid-IR to far-IR photodetectors based on current semiconductors or alloys are the small band gap which can produce high dark current/noise and the restricted materials growth process, as shown in Figure 1.5. Furthermore, the cost of growth of these materials is very expensive. Hence, exploration of novel materials for MIR photodetectors is crucial.

Plasmons[12], charge oscillations at the interface between a dielectric a metal, can be employed to resolve some limitations in the mid-infrared photodetector, since plasmons can raise a very strong localised electromagnetic field and can be guided along the interface in the form of a travelling wave. Furthermore, graphene plasmons[13] mode can be excited at the MIR spectra and have the advantages of higher confinement, longer propagating length and higher relaxation time compared with noble metal plasmons.

1.4 Surface plasmons

Generally speaking, the electron oscillation is the back and forth swings of electrons relative to the equilibrium position when they derived by the restoring force. We can obtain two solutions by solving the Maxwell equations, one is radiative mode and other one is collective mode. However, little attention has been paid on the collective mode until its remarkable

properties had been investigated in the recent years. And this branch has formed the subject of Plasmonics. Strictly speaking, the discovery of plasmon can trace back to 1902 in Wood's work of diffraction grating spectrum. But he did not demonstrate a plausible explanation about the phenomenon at that time and thus it was called Wood's anomalies. The theoretical explanation was given by Fano about 40 years later. He pointed out that the phenomenon is the excited Sommerfeld's type EM wave which possesses large tangential momentum on a metallic surface.

Overcoming the diffraction limit problem i.e. confining and controlling light at scales of subnanometer is required in the nanophotonics field. At present, surface plasmons is the most prominent strategy that can achieve this goal[14]. Surface plasmons (or more exactly surface plasmon polaritons, SPPs) are electromagnetic excitations that propagate along the interface between a metal and a dielectric medium[12]. Due to the very high loss, the plasmons in the direction perpendicular to the propagation are exponentially evanesced. But fortunately, it can propagate rather long distance compared with the incident wavelength. In the below section, I will give the theory derivation from Maxwell equations, its properties and the excited techniques.

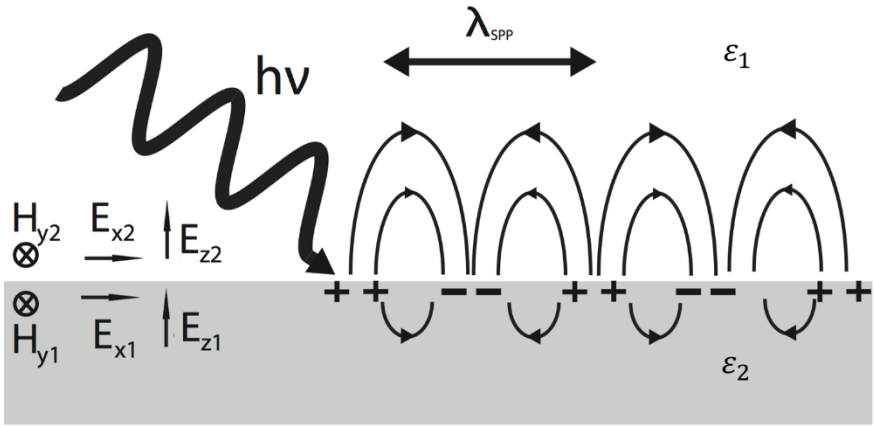

Figure 1.6 Schematic of the excitation of surface plasmon polaritons along a interface between a dielectric and a metal.

Assuming the light with angular frequency ω propagates along the interface between a dielectric (permittivity ε_1) and a metal (permittivity ε_2), as shown in figure 1.6. According to the boundary condition, we can obtain that:

$$D_{1,z} = D_{2,z}, B_{1,z} = B_{2,z} \tag{1.6}$$

$$E_{1,x/y} = E_{2,x/y}, H_{1,x/y} = H_{2,\frac{x}{y}} \tag{1.7}$$

And the classical Maxwell equations have the following form:

$$\begin{aligned} \nabla \cdot \mathrm{D} &= \rho \\ \nabla \cdot \mathrm{B} &= 0 \\ \nabla \times \mathrm{E} &= -\frac{\partial B}{\partial t} \\ \nabla \times \mathrm{H} &= \mathrm{J} + \frac{\partial D}{\partial t} \end{aligned} \tag{1.8}$$

If we verify the TE mode by substituting the components of E and H into the Maxwell equations, then we get a wrong deviation which means that the TE mode does not exist under these conditions. The TM mode has the below components as the light propagating along the x direction.

$$E_i = \left(E_{i,x}, 0, E_{i,y}\right) e^{i(\overrightarrow{k_i}.\vec{r} - i\omega t)} \tag{1.9}$$

$$H_i = \left(0, H_{i,y}, 0\right) e^{i(\overrightarrow{k_i}.\vec{r} - i\omega t)} \tag{1.10}$$

where the indices (1) and (2) indicate the dielectric and metal, respectively.

Substituting the TM components into Maxwell equations with absence of charges and currents and combing the boundary conditions, we can obtain the following relationship:

$$\frac{k_{1,z}}{\varepsilon_1} = \frac{k_{2,z}}{\varepsilon_2} \tag{1.11}$$

Now, we derive the dispersion relations of surface plasmon. The wave vector component along x axis is the propagation constant β and it can be obtained from the equation below.

$$\vec{k}_i^2 = \varepsilon_i k_0^2 = \beta^2 + k_{i,z}^2 \tag{1.12}$$

here, k_0 is the vacuum wave vector of light. Combing equations 1.11 and 1.12, then we can obtain the propagation constant of surface plasmon:

$$\beta = \frac{\omega}{c}\sqrt{\frac{\varepsilon_1 \varepsilon_2}{\varepsilon_1 + \varepsilon_2}} \tag{1.13}$$

Propagation length δ (see figure 1.7 (a)), a very important value to characterise the damping strength is given by

$$\delta = \frac{1}{2Im(\beta)} \tag{1.14}$$

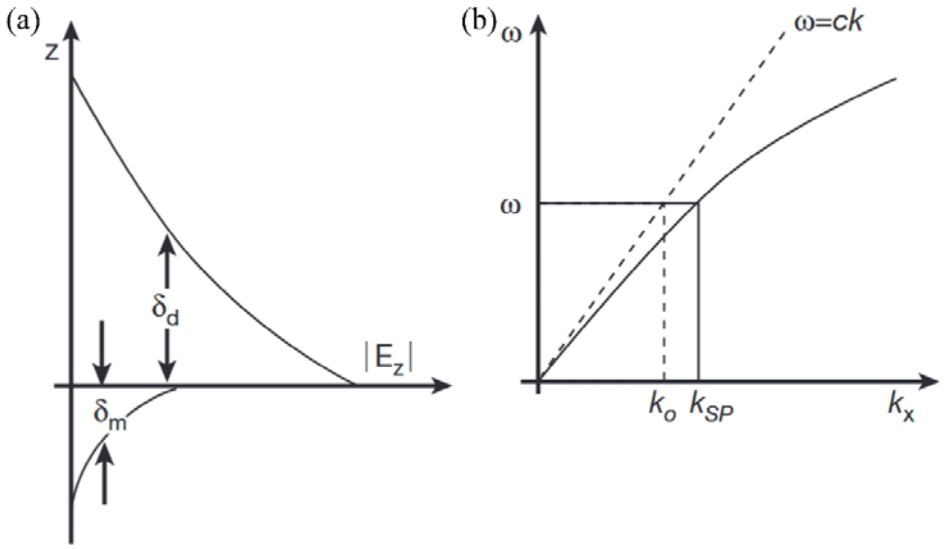

Figure 1.7 (a) Evanescent fields in the dielectric and metal regions. (b) Dispersion relation of surface plasmons compared to light in vacuum. Figures reproduced from [12].

As shown in figure 1.7 (b), the SP mode has a greater momentum than the one of in free space of the same frequency. Therefore, it's impossible to excite the SP mode by direct light beam unless techniques to achieve phase matching are employed. Usually, the methods used to overcome the phase mismatch problem are prism coupling, grating coupling and excitation using focused optical beams.

1.5 Graphene

Graphene is one layer of sp^2-hybridized carbon atoms with the pattern of a honeycomb lattice. Due to its remarkable properties, many of the unique capabilities and characteristics of graphene have been investigated over the past few years. The explosive study of graphene application follows consequently. As the first proposed and investigated 2D material, it has emerged as the candidate for the next generation of optoelectronics devices due to its

remarkable optical and electronics properties. First, the gapless nature of its energy band structure enables photon absorption and electron-hole pairs generation across an ultra-wide spectra from the UV to the terahertz[15]. Secondly, the linear dispersion relationship around Dirac cone with the electrons behaves as massless Dirac fermions contribute to the ultra-high charge-carrier mobility of > 10^5 $cm^2/V{\cdot}s$ for both electrons and holes at room temperature[16]. Another intriguing property is that the optoelectronic features can be dynamically tuned by changing its Fermi level via the external voltage or chemical doping[17] which give the graphene-based devices another freedom to alter the performance in real time.

1.5.1 Electronic properties of graphene

The four outer shell electrons hybridise and form three sp2 hybridized orbitals (σ bonds) which cause the honeycomb formation and one unhybridized $2p_z$ orbital (π bond) that lies perpendicular to the 2D plane. The unit cell of its lattice structure can be treated as triangular lattice with two atoms. The lattice vectors and reciprocal lattice vectors have the following form

$$\vec{a}_1 = \frac{a}{2}(3, \sqrt{3}), \qquad \vec{a}_2 = \frac{a}{2}(3, -\sqrt{3}) \tag{1.15}$$

$$\vec{b}_1 = \frac{2\pi}{3a}(1, \sqrt{3}), \qquad \vec{b}_2 = \frac{2\pi}{3a}(1, -\sqrt{3}) \tag{1.16}$$

where a≈1.42 is the lattice constant. The two points K and K' (named as Dirac points) at the corners of graphene Brillouin Zone (BZ) are of particular importance for the physics of graphene. They have the following form in the reciprocal space

$$\mathrm{K} = \left(\frac{2\pi}{3a}, \frac{2\pi}{3\sqrt{3}a}\right), K' = \left(\frac{2\pi}{3a}, -\frac{2\pi}{3\sqrt{3}a}\right) \tag{1.17}$$

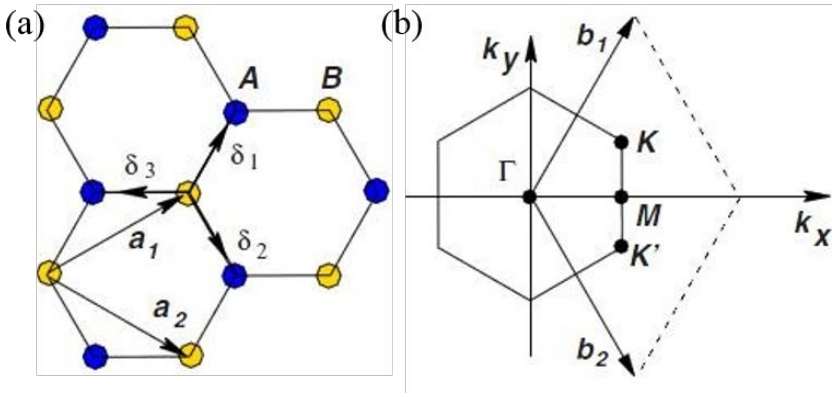

Figure 1.8 (a) Lattice structure of graphene. (b) Brillouin zone of graphene lattice. $\mathbf{a_1}$ $\mathbf{a_2}$ are the lattice unit vectors. Images adapted from [15].

When applying a tight-binding approach, the electrons in graphene can only hop to nearest- and next-nearest-neighbour atoms. The energy bands can be derived from the Hamiltonian and have the form

$$E_{\pm}(\vec{k}) = \pm t\sqrt{3 + f(\vec{k})} - t' f(\vec{k}) \tag{1.18}$$

where $\vec{k}$ is the wave vector, the plus sign and minus sign applies to the upper (named as π^* band) and lower band (named as π band) respectively. t and t' are the nearest-neighbor and the next nearest-neighbor hopping energy, respectively, and

$$f(\vec{k}) = 2cos(\sqrt{3}k_y a) + 4cos\left(\frac{\sqrt{3}k_y a}{2}\right) cos\left(\frac{\sqrt{3}k_x a}{2}\right) \tag{1.19}$$

It is easy to discover that the obtained two bands are symmetric around zero energy if t'=0. While for finite values of t', the electron-hole symmetry is broken. The two bands touch each other at the Dirac point and their structures are cone-like in the region close to the Dirac point. This dispersion close to the Dirac point ($\vec{K} or\ \vec{K}'$) can be derived by expanding the full band relation at small wave vector, as $\vec{k} = \vec{K} + \vec{q}$ with $|\vec{q}| \ll |\vec{K}|$.

$$\vec{E}_{\pm}(\vec{q}) \approx \pm v_F |\vec{q}| \tag{1.20}$$

here, $\vec{q}$ is the momentum relative to the Dirac points and $v_F$is the Fermi velocity which given by $v_F = 3ta/2$ equalled to the value $v_F \approx 1 \times 10^6 m/s$. This is a rather high value and it's striking different with the usual case for it doesn't depend on the energy or momentum.

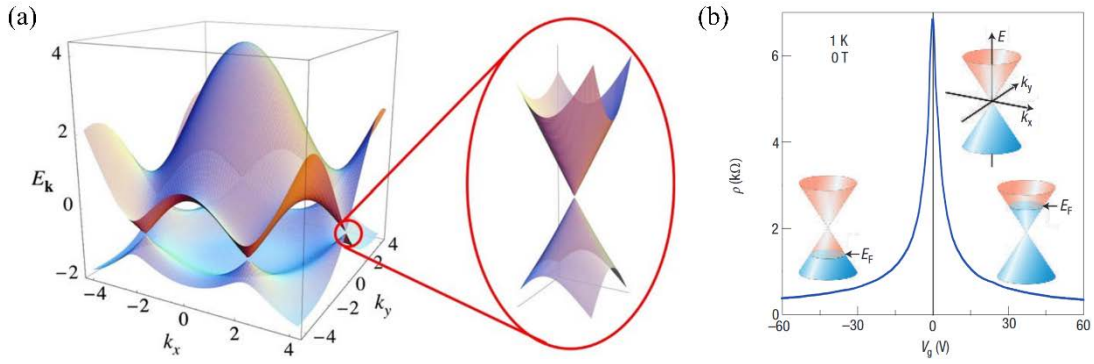

Figure 1.9 (a) The conical band structure of graphene. Inset is the band structure around Dirac point. (b) The resistance of monolayer graphene as function of back gate voltage. Insets show the position of Fermi level and Dirac point of graphene with different back gate voltage. Images adapted from [15, 18].

For pristine graphene, Fermi level E_F is equal to the energy at Dirac point. However, when the graphene is doped or applied by external gate, the Fermi level can shift upward or downward. The shift of Fermi level can tune its conductivity and hence have an extensive application in many aspects.

From the conical band structure (see figure 1.9), the energy and momentum have a linear relationship which different from the quadratic relationship of most materials over a wide range of energies around the Dirac point. Thus, the electrons behaved like massless relativistic particles called Dirac fermions. At the low energy range, there are two parts, intraband transition and interband transition, contributing to graphene's conductivity. The formula derived from Kubo equation[19] given in the following form,

$$\sigma(\omega,\mu_c,\Gamma,T)=\sigma_{intra}+\sigma_{inter}$$

$$=-\frac{ie^2(\omega+i2\Gamma)}{\pi\hbar^2}\left[\frac{1}{(\omega+i2\Gamma)^2}\int_0^{\infty}E\left(\frac{\partial f(E)}{\partial E}-\frac{\partial f(-E)}{\partial E}\right)dE\right.$$

$$\left.-\int_0^{\infty}\frac{f(-E)-f(E)}{(\omega+i2\Gamma)^2-4\left(\frac{E}{\hbar}\right)^2}dE\right] \qquad (1.21)$$

where ω,μ,Γ and T are frequency of incident light, chemical potential, scattering rate and temperature respectively.f(E) $=1/\left(1+exp((E-\mu_c)/k_BT)\right)$ is Fermi distribution function. By substituting Fermi distribution function into the conductivity, we can obtain a simple form at the prerequisite of high doping or electrical gating i.e. $|\mu_c|\gg k_BT$ and $\hbar\omega\gg k_BT$.

$$\sigma_{intra} = i\frac{e^2 k_B T}{\pi\hbar^2\left(\omega + \frac{i}{\tau}\right)}\left[\frac{\mu_c}{k_B T} + 2ln\left(e^{-\frac{\mu_c}{k_B T}} + 1\right)\right] \quad (1.22)$$

$$\sigma_{inter} = i\frac{e^2}{4\pi\hbar} ln\left[\frac{2|\mu_c| - \hbar(\omega + i/\tau)}{2|\mu_c| + \hbar(\omega + i/\tau)}\right] \quad (1.23)$$

Furthermore, the conductivity and permittivity have the following relationship

$$\varepsilon = \varepsilon_0\varepsilon_r + i\frac{\sigma_v}{\omega} = \varepsilon_0\varepsilon_r + i\frac{\sigma_s}{\omega\Delta} \quad (1.24)$$

where σ_v, σ_s are volume conductivity and surface conductivity respectively; Δ is the thickness of graphene; ε_r=1 is the relative permittivity.

1.5.2 Optical properties of graphene

Two different types of mechanisms, intraband transitions and interband transitions, contribute to the optical absorption of graphene. Moreover, their relative importance depends largely on the spectral range of illuminated light. In the far infrared region, the optical absorption is dominated by interband transitions and it can be fitted well in a Drude model[20]. In the near infrared to visible spectral range, the optical response is primarily attributed to the interband transitions. This response is famous for the universal optical conductivity[21, 22] which is only determined by the fine-structure constant in pristine graphene. But the response can be tuned via chemical doping or external gating which shifts the Fermi energy and correspondingly induces the Pauli blocking of the optical absorption[23, 24]. In the ultraviolet region, the response exhibits signatures of excitonic effects because of the increasement of interband transitions[25]. However, the situation is more complex in the mid-infraed wavelenght region. This is because that although the optical absorbance in this region is primarily attributed to interband transition[26, 27], Fermi level also have an effect on the optical absorbance.

In the following content, I will give the explanation of intraband transitions and interband transitions.

Intraband transition can't directly absorb a photon due to momentum conservation restrictions. To conserve momentum, additional scattering with defects or phonons is required to ensure that momentum is conserved. In this situation, a Drude model was employed to describe the frequency-dependent sheet conductivity,

$$\sigma_\omega = \frac{ie^2|E_F|}{\pi\hbar^2(\omega + i/\tau)} \tag{1.25}$$

here, τ is the electron relaxation time.

Interband absorption dominates at frequencies near the infrared and visible region and contributes to the direct optical transitions between valance and conduction bands. In this region, the tight-binding model was used to depict the performance of optical sheet conductivity from interband transitions. For pristine graphene, the conductivity at zero temperature is independent of frequency.

$$\sigma(\omega) = \pi e^2/2h \tag{1.26}$$

In the spectra range of mid infrared, neither intraband nor interband can dominate the optical conductivity. Hence, we should consider the contribution attribute both of them when we deal with the mid infrared spectra problems.

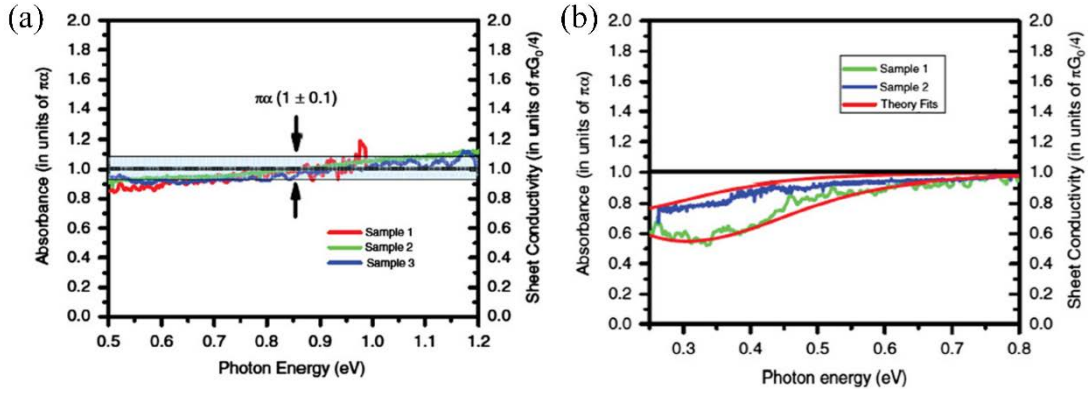

Figure 1.10 (a) Optical sheet conductivity and absorbance of three graphene samples as function of photon energy range from 0.5 to 1.2 eV. (b) Sheet absorbance of two graphene samples with different Fermi level over photon energy from 0.25 to 0.8 eV. The theory fits correspond to theory considering of both finite doping and finite temperatures. Images adapted from [27].

1.5.3 Band gap engineering

A band gap is the energy range in a solid where no electron states can exist. Band gap opening is the procedure of opening or altering the band gap of materials. Insulators have a much larger band gap than semiconductors and metals that do not have a band gap, as the valance bands and conduction bands overlapped. Semiconductor crystals have fixed band gaps owing to continuous energy states (see Figure 1.11). However, in quantum dot crystals, the band gaps are size dependent and can be tuned to produce a range of energies between valance bands and conduction bands. This phenomenon is known as the quantum confinement effect.

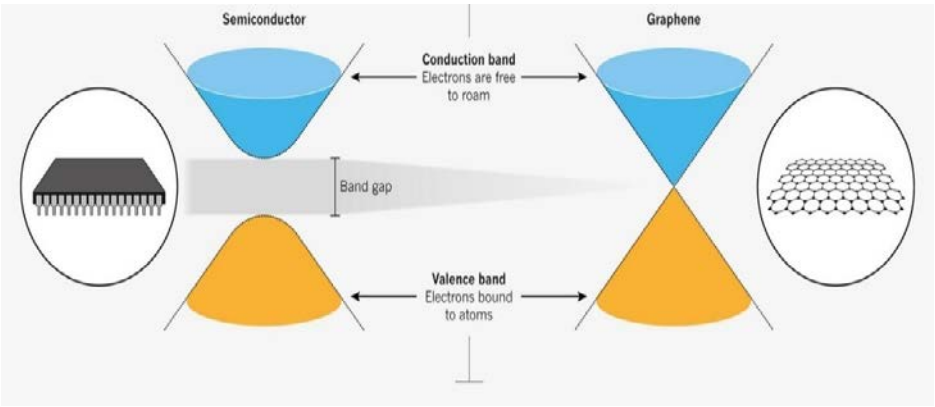

Figure 1.11 Schematic of an energy band for graphene and semiconductor materials. Image adapted from [28].

Graphene is a semimetal of which the valance bands and conduction bands touch each other at single points: the Dirac points. Thus, graphene is gapless which can lead to both advantageous and disadvantageous effects in the fields of light harvesting, photodetection and optical sensing, among others. The positive effect is that graphene can absorb across an extremely broad wavelength range. The negative effect is that large dark currents can also be produced, lower photocurrents are generated, and there is no spectral selectivity. Hence, opening the bandgap of graphene can produce benefits in many graphene applications. Currently, the main method of opening a band gap is by patterning graphene. Graphene nanoribbons have a ribbon-width-dependent band gap[29]. Graphene discs can also have a band gap when the diameter of the discs is in the scale of nanometre, and the same applies for graphene quantum dots. Graphene nanomesh (GNM)[30-32], another graphene pattern, can have a tunable band gap as well. Therefore, we hope to introduce a bandgap in our photodetector structure to avoid large dark current and enhance the light harvesting, to boost responsivity.

1.5.4 Graphene surface plasmons

Different from the conventional surface plasmons which can only support the TM mode, graphene plasmons can both support TM and TE mode. Just like the derivation of conventional surface plasmons' dispersion relationship, I will give the dispersion relationship of graphene plasmons in TM mode.

Assuming the graphene was placed between the dielectrics with permittivity of ε_{r1} and ε_{r2} and the TM mode propagates along the z axis as depicted in Figure 1.12. Thus, it has the following electric field form[33]

$$\begin{aligned} \vec{E} &= \left(Ae^{iqz-Q_1x}, 0, Be^{iqz-Q_1x}\right), \ for\ x > 0 \\ \vec{E} &= \left(Ce^{iqz+Q_2x}, 0, De^{iqz+Q_2x}\right), \ for\ x < 0 \end{aligned} \tag{1.27}$$

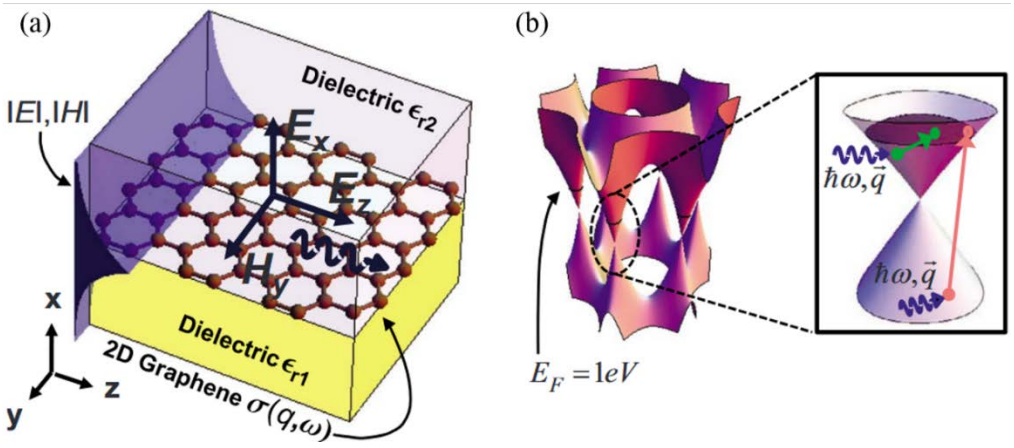

Figure 1.12 (a) Schematic of TM graphene plasmons in graphene system. (b) Electronic band structure of graphene layer. Inset: The sketch of interband (red arrow) and intraband (green arrow) transition. Images adapted from [34].

By substituting the equations into Maxwell equations and combing the boundary conditions, we can obtain the dispersion relationship

$$\frac{\varepsilon_{r1}}{\sqrt{q^2 - \frac{\varepsilon_{r1}\omega^2}{c^2}}} + \frac{\varepsilon_{r2}}{\sqrt{q^2 - \frac{\varepsilon_{r2}\omega^2}{c^2}}} = -i\frac{\sigma}{\omega\varepsilon_0} \tag{1.28}$$

The above dispersion relationship can be simplified for the nonretarded regime i.e. when $q \gg \omega/c$

$$q \approx Q_1 \approx Q_2 \approx \varepsilon_0 \frac{\varepsilon_{r1}+\varepsilon_{r2}}{2} \frac{2i\omega}{\sigma} \tag{1.29}$$

In the same way, the dispersion relationship of TE mode can also be deprived by substituting the components of TE mode into the Maxwell equations and matching the boundary conditions. For the reason that there is momentum mismatch between graphene plasmons and light in free space, the excitation of graphene plasmons is still very difficult in experiment. However, the development of scanning near field optical microscopy gives us the opportunity to directly imagine the propagating and localised graphene plasmons. Recently, the researchers from UCLA[35, 36] and ICFO[37] successfully excited and nanoimaged the infrared graphene plasmon in gated graphene on silica substrate as illustrated in figure 1.13. To solve the momentum mismatch problem, they illuminated the tip of AFM with the focused infrared beam of 11.2 μm. As the radius of curvature is about a=25 nanometre, it imparted the momentum of order 1/a for the graphene plasmons. The excited graphene plasmons propagate along the graphene sheet and they will be reflected, damped and interfaced when they encounter the edges, defects and boundaries of different layers. The standing wave pattern was formed when the propagating graphene plasmon interfered with the reflected ones. Thus, we can obtain the wavelength of 200 nm which is consistent with the theory value demonstrated by equation 1.29.

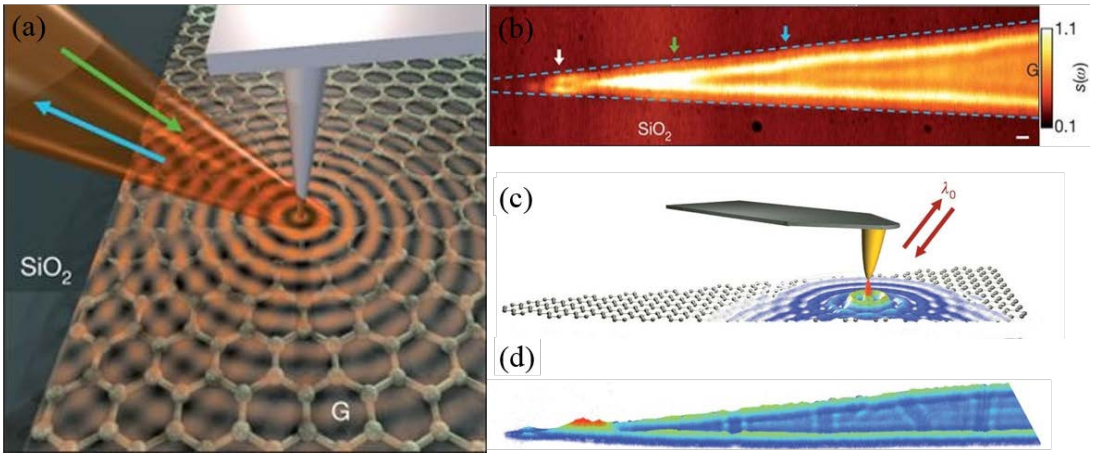

Figure 1.13 (a) Diagram of an infrared nano-imaging experiment at the surface of graphene on SiO_2. The excitation wavelength is 11.2 μm. (b) Image of Normalised infrared amplitude after excitation. Scale bar is 100 nm. (c) Diagram of launching and detecting propagating surface plasmons in graphene ribbon (12 μm long and 1 μm wide) on 6H-SiC. The excitation wavelength here is 9.7 μm. (d) Image of near-field amplitude image obtained for a tapered graphene ribbon. Figure (a) and (b) adpated from [36]. Figure (c) and (d) adapted from [37].

1.6 Chirality

Wavelength is only one property of light and other properties are preferable to utilise for detection to encode additional data channels or increase collection efficiency; for example, in telecommunication systems, wavelength, time division, frequency division and phase have been used. This is available and achievable in the visible and telecommunication wavelength range; however, it is difficult for the MIR, because MIR sources are difficult to produce and there is a lack of cheap, well-functioning MIR photodetectors.

Chirality refers to a geometric property of a structure such that the mirror image cannot be translated or rotated back on itself. This property exists in many forms in nature, such as molecules, proteins and crystals. The most common example of a three dimensional (3D) chiral object is human hands (see Figure 1.14).

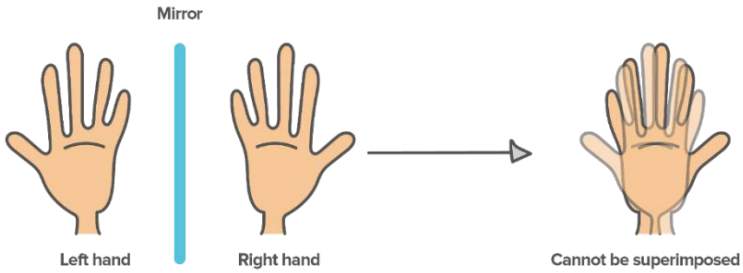

Figure 1.14 Example of a chiral object: human hands.

Chiral geometries can produce intriguing chiral-optical effects, such as circular dichroism, which is widely used in optical rotators, optical isolators and biological spectroscopy. Circular dichroism (CD) is the differential absorption of left-handed polarised (LCP) and right-handed polarised (RCP) light; however, this CD is very weak in nature materials/structures, and therefore, the chiral effect is detectable only when the optical path length is much larger than the wavelength of light. This inhibits the development of compact chiral-optical devices.

The geometry of nano-engineered structures determines their physical properties and thus how light interacts with them. Hence, to design chiral structures that not only have high absorption but possess significant CD, we need to consider the chirality property of the chiral structure and the permittivity of the materials.

However, obtaining these functionalities with traditional materials, particularly in MIR, to achieve high performance is difficult. Hence, we explore the properties of graphene and its potential applications in MIR photodetectors.

1.7 Thesis objective

The objective of this thesis is to explore how surface plasmon resonances can be utilised to overcome the challenges of the mid-infrared graphene photodetection. In particular this thesis will investigate how chiral localised surface plasmon resonances can be used to enhance graphene responsivity whilst enabling detection of important properties of light such as spin angular momentum. The thesis will also explore how intrinsic localised surface plasmon resonances can further enhance photocurrent generation in graphene, whilst simultaneously providing reduced dark current via band-gap engineering and wavelength tuneability via fermi-level tuning.

This PhD thesis aims to complete this objective by completing the following tasks across three theoretical and experimental investigations:

A: Theoretical and experimental investigation of a novel photon-spin detecting scheme based on zig-zag chiral surface plasmon electrode photodetector (Chapter 3)

1. Design zig-zag chiral plasmonic structures that can simultaneously distinct the photon spin angular momentum states of incident light as the source and drain electrodes.

2. Numerically simulate the absorption of photodetector structure and graphene layer for each structural parameter under illumination of circularly polarised light and investigate the circular dichroism properties of this photodetector.

3. Experimentally fabricate zig-zag chiral surface plasmon electrode photodetectors and determinate their sizes and structural integrity via scanning electron microscopy.

4. Optically characterise the transmission spectra of fabricated photodetectors under the illumination of left and right circularly polarised light and then calculate the extinction spectra to compare with the numerical simulation results.

5. Electronically characterise the electronic properties of fabricated photodetectors by illuminating both the left-handed chiral electrode and right-handed chiral electrode with left and right circularly polarised light respectively. And compare with the simulation results.

6. Demonstrate direct detection of photon spin angular momentum by uniformly and fully illuminating both electrodes and the incident light is then oscillated between left circularly polarised light and right circularly polarised light whilst recording the measured responsivity.

B: Theoretical investigation of nanomesh arrays for simultaneous band-gap engineering and surface plasmon resonance absorption enhancement (Chapter 4)

1. Theoretically calculate the impact of the size of defect, the period of defect array and the array arrangement type on the band gap size.

2. Numerically simulate the effect of the period of defect size, the period of defect array and the Fermi level of graphene layer on the absorption magnitude and resonant wavelength of graphene plasmons.

3. Compare the energy of introduced band gap, thermal fluctuation at room temperature and the corresponding energy of resonant wavelength of graphene plasmons for the GNM structure to verify whether band gap engineering and graphene plasmons can simultaneously improve the absorption enhancement and restrict dark current.

C: Experimental development and optical characterisation of a nanomesh array graphene photodetector (Chapter 5)

1. Experimentally fabricate the GNM photodectors and determine their structural integrity via scanning electron microscopy.

2. Geometrically characterise their structural properties from the aspects of hole size, neck width, uniformity and roughness.

3. Electronically characterise the Fermi level of fabricated GNM photodetectors to compare with the simulation results in chapter 4.

4. Optically characterise the fabricated GNM photodetectors by measuring the transmission spectra under different back gate voltage (i.e. different Fermi level) and calculate the extinction spectra to compare with the simulation results in chapter 4.

1.8 Thesis outline

This thesis is structured as follows:

In Chapter 1, we introduced information photonics and its limitations in some applications and why optoelectronics can solve some of these existing problems. However, one important area of optoelectronics, photodetection, currently has serious limitations in mid-infrared wavelength because of high cost, thermal fluctuation and restricted growth conditions of materials; thus, we noted the need to explore and exploit research on mid-infrared photodetectors with new materials or designs. Following this, we introduced graphene, surface plasmons and graphene localised surface plasmons and why the combination of these can solve some mid-infrared photodetection problems. Last, we established our thesis objective and the outline of this thesis.

Chapter 2 explores past work and identifies areas requiring further research. We review the mechanisms of graphene photodetectors, published graphene photodetectors, absorption and photocurrent enhancement of graphene photodetectors by surface plasmons, graphene band gap engineering and chiral photodetection. The review of the graphene photodetector mechanism instructs us to take advantage of each mechanism when designing our photodetection structures. The first class of investigated graphene photodetectors was the metal-graphene-metal type, where a photocurrent was generated when the metal-graphene interfaces were illuminated with light. However, this type of design is limited by the submicrometric wide metal-graphene interface region where the photocurrent is produced. Therefore, many new designs have been proposed and investigated to improve the performance of graphene photodetectors. We classify these new architectures into two main types: photonic integration, such as waveguide, cavity and photonic crystal, and graphene nanostructure engineering, such as graphene nanoribbon, nanodots and nanomesh.

We then review graphene plasmons and enhancement for absorption and photocurrent to explain how localised surface plasmons can solve the low responsivity issue. Furthermore, band gap engineering is reviewed to solve the dark current issue. The last part of this chapter concerns chiral photodetection. We review all published work on circularly polarised light detectors and summarise their performs. After reviewing previous work on graphene photodetection and chiral detection, we find that there are large gaps in knowledge, poor performance and missing functionality; in response to these gaps, we propose and demonstrate our own work in the following chapters.

Chapter 3 focuses on the investigation of the direct detection of spin angular momentum detection by a graphene mid-infrared photodetector. As shown in Chapter 2, there is only one paper on mid-infrared photon spin angular momentum detection and this paper possessed very low efficiency (CD is only 10%). Therefore, we demonstrate the direct detection of photon spin angular momentum in the mid-infrared by a single surface-plasmon-enhanced graphene photodetector. We utilise chiral surface plasmon nanostructures as photodetector electrodes to generate a photocurrent of equal and opposite sign according to the incident photon spin. Our detector possesses a current CD of 60 % and a responsivity of 0.80 μA/W at a resonant wavelength of 3.8 μm. As the chirality and resonant wavelength of our photodetector results from the chirality and size of the surface plasmon electrodes and not the intrinsic properties of any of the materials, additional electrode geometries can be incorporated into a single device to expand the detection of other multiplexed states such as wavelength and orbital angular momentum.

Chapter 4 theoretically and numerically investigates the GNM structure as the platform of graphene photodetectors. Because the metal surface plasmons is parasitic, we exploit graphene plasmons supported by a GNM structure to improve the light absorption and photocurrent of the graphene photodetector in this chapter. Furthermore, band gap engineering was explored to investigate how to restrict dark current. The band gap and surface plasmons together determinate the concrete design of the GNM structure.

Chapter 5 realises the fabrication of a GNM photodetector and its related geometric, electronic and optical characterisation. Two types of graphene (exfoliated graphene and chemical vapour deposition (CVD) graphene) and two methods (focused ion beam (FIB) and electron beam lithography (EBL)) were utilised to fabricate the GNM photodetector. With optimised recipes, a GNM structure with diameter of 40 nm and neck with of 10 nm was successfully fabricated. Moreover, the fabricated structure is fully characterised by size, uniformity and roughness aspects. In addition, electronic tunability has been realised, which is the basis for the tunable property of GNM photodetectors. Lastly, graphene plasmons were experimentally observed via the resonant peaks and their shift with different back gate voltage from the extinction spectra.

Chapter 6 provides a summary and discussion of the outcomes of this thesis. We conclude by proposing future research based on the investigations of this thesis.

Chapter 2

Literature review

2.1 Introduction

As one of the most prominent applications of graphene, graphene photodetection promises significant advantages over state of art photodetectors based on semiconductors. Furthermore, graphene can also support surface plasmons directly, offering a unique single material platform for both the generation and enhancement of photodetection. In this chapter, I will review previous work in graphene, graphene photodetection, and graphene surface plasmons. This forms the basis of this work and has driven our investigation direction.

2.2 Mechanisms of graphene photodetection

In this sectoin, I begin with a short introduction to the photodetection mechanisms. I mainly discuss the three most important physical mechanisms in photodetection based on graphene including photovoltaic (PV) effect, photo-thermoelectric (PTE) effect and photo-bolometric (PB) effect.

The physical mechanism of the graphene photodetector was assumed to be similar to the conventional photodetection mechanism at first. However, following intensive research and development of new photodetector structures, unveiled physical mechanisms differ and are

more complicate than conventional ones. There is normally more than one mechanism in a specific structure, and any may dominate depending on the situation[38].

The PV effect was the first proposed and most intuitively obtained as compared with the previous 3D semiconductor photodetectors, such as gallium arsenide and silicon. In the first research period, the proposed structure was uniform graphene put between two different types of metals[39], or the same metals at different distance[40]. Another stucture involve laying metal electrodes on the graphene junctions in different doped regions[41-43]. The purpose of this design was to establish a built-in electric field from the different chemical potentials between metal electrodes or different doped regions of graphene. Hence, the excitons which are excited by incident photons, can be separated and propelled by the built-in electric field (see Figure 2.1). Though the same effect can be achieved by adding a source-drain bias voltage, this is normally avoided in graphene photodetectors because this can generate a large dark current due to its semimetal band structure. As the graphene's Fermi level can be tuned by external voltage, the potential discrepancy can be externally tuned, which is a very important property for photodetection.

Under this mechanism, the photocurrent can be written as

$$I_{ph} = q\mu VA\Delta n \tag{2.1}$$

where q and μ are the unit electron charge and charge carrier mobility, V is the potential discrepancy, A is the cross section area of the active layer, and Δn is the number of photo-induced carriers. It is evident that the photocurrent is proportional to the charge carrier mobility. Therefore, graphene is an ideal material for photodetection because of its high carrier mobility[44]. However, both the low absorption efficiency for the one layer of atoms interaction distance and short lifetime[45-47] of the excitons (in the order of tens of picoseconds) lead to responsivity of several mili ampere per watt. I demonstrate how to improve the responsivity performance later, in the review of graphene photodetectors section.

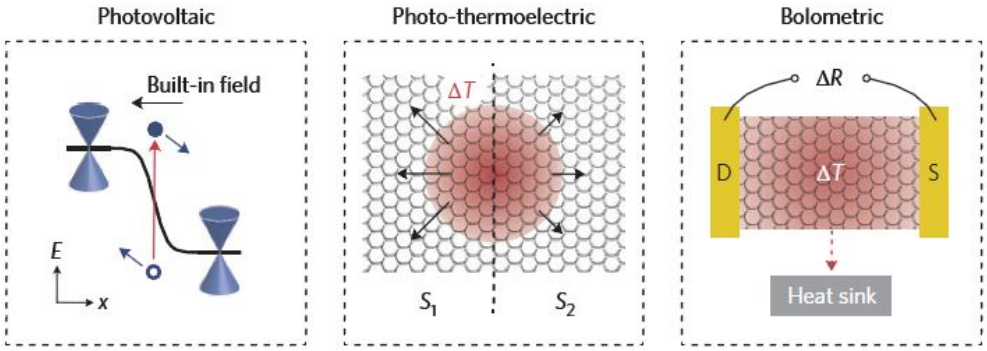

Figure 2.1 Schematic representation of the three photocurrent generation mechanisms. Images adapted from [38].

The PTE effect, thermoelectric effect induced by light illumination, was first revealed by Xu et al.[48] based on a very delicate single-layer graphene binary structure that was constructed by partially covering a single-layer graphene with another one. Thus, a single-bilayer graphene interface was formed. Because single-layer and bilayer graphene have a linear and quadratic energy-momentum dispersion relation respectively, the Fermi energy is not far from the Dirac point, $|E_F|$ of the single layer and is larger than that of the bilayer for the same charge density. This discrepancy leads to the built-in bias from the single-layer to the bilayer. However, on the other hand, hot carriers tend to diffuse from low DOS sites to high DOS sites according to the thermodynamics. The photocurrent generated by the PTE effect is given by

$$I_{PTE} = \frac{(S_2 - S_1)\Delta T}{R} \tag{2.2}$$

where R is resistance, ΔT is temperature difference and S is thermoelectric power (also called the Seebeck coefficient). The Seebeck coefficient related to the DOS and Fermi level has the below form

$$\mathrm{S} = \frac{\pi^2 k_b^2 T}{3q} \frac{1}{G} \frac{dG}{dE} \; E = E_F \tag{2.3}$$

where q is the unit electron charge, k_b is the Boltzmann constant, T is temperature and G is conductance.

According to their observation through photocurrent microscopy with radiation of 635 nm manifested the dominant role in the device. This effect has been corroborated by many later studies.

The PB effect is about the relationship between conductivity and temperature. The presence of incident light can lead to a change of conductance that may result from the following two mechanisms. One mechanism is the change of mobility due to the temperature change and the other is the change in number of carriers related to the photocurrent. More particular studies are necessary to investigate the PB effect for its subtle properties and yet to be studied thoroughly.

2.3 Graphene photodetectors

The first published graphene photodetector structure was constructed by depositing two different metal electrodes on one layer of graphene. The following studies were based on this idea, but as the development and expansion of 2D materials family progresses, photodetectors based on other 2D materials[49-51] or the heterostructure combining bilayer graphene[52] or graphene and other 2D materials[53-56] have also been extensively investigated. In this section, I review of graphene photodetectors based on one layer of graphene.

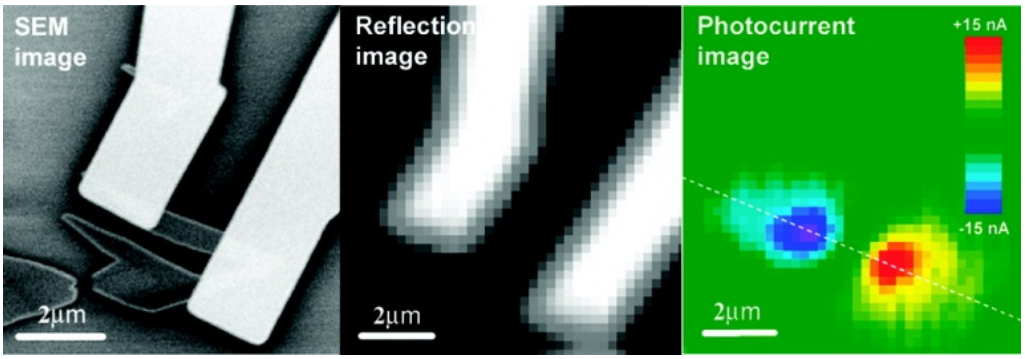

Figure 2.2 Scanning electron micrograph (SEM) of a graphene FET photodetector (left). Reflection image (middle). Photocurrent image(right). Images adapted from [57].

In the early stage, graphene field-effect transistor (FET) photodetectors[57-59] were performed to demonstrate the detection function (see Figure 2.2). When locally illuminating the graphene-metal interface, the photo-excited electron-hole pairs are separated by the built-

in electric field due to the different chemical potentials. This leads to a photocurrent in the external circuit, attributed to the PV effect. As the charges are driven by the potential discrepancy, it can be adjusted by proper choice of metal contact or by doped graphene via back gating. Besides the PV effect, the PTE effect can also contribute to the photocurrent in the circumstances of p-n junctions[48, 60] or interfaces between single layer and bilayer graphene[61].

However, in this type of structure, the effective photodetection area is limited to the submicrometre-wide metal-graphene contact region, which results in low responsivity. To solve this problem, an interdigital finger structure was introduced to expand the effective photodetection area[39]. With this method, responsivity can be enhanced to tens of mili ampere per watt. Because of the fast carrier mobility and short carrier lifetime of graphene, the response speed of this type of graphene photodetector ranges from several tens of gigahertz to a very high several hundreds of gigahertz[39].

Because of the FET structure of single-layer graphene photodetectors, the first stage is very simple and the mechanisms were thoroughly investigated. Generally speaking, the later modification strategy mainly involves two aspects: device geometry modification and materials engineering. As the absorption efficiency is only 2.3% (rather low in absolute terms), delicate device geometry designs were adopted to enhance absorption ability (i.e., to modulate responsivity). The counterpart is material engineering which can obtain very high responsivity in most cases[62-64] but usually at the cost of decreasing response speed.

Geometry modification, can be classified into two types: suspended graphene photodetectors[61, 65, 66] and graphene photodetectors integrated with photonic structures, such as waveguide[40, 67, 68], microcavity[69-72] and plasmonic structures[73-75].

2.3.1 Photonic integration

The integration of graphene with waveguide has been reported by Gan et al., Posposchil et al., and Wang et al. respectively with similar geometry [40, 67, 68, 76] (see Figure 2.3) The interaction length is only one atomic layer thick if directly illuminating light on graphene; however, the interaction length, determined by the waveguide length, was increased by propagating the light in the waveguide under the graphene. As the graphene is not regulated,

they achieved bandwidth of 20GHz and an open eye at 12Gbit s^{-1}. The responsivities range from 0.05 to 0.13AW^{-1} which has two orders of magnitude enhancement. However, to achieve high absorption in graphene, the waveguide length is tens to hundreds of micrometres, which limits the operation bandwidth to tens of gigahertz[77] as the devices have a large capacitance.

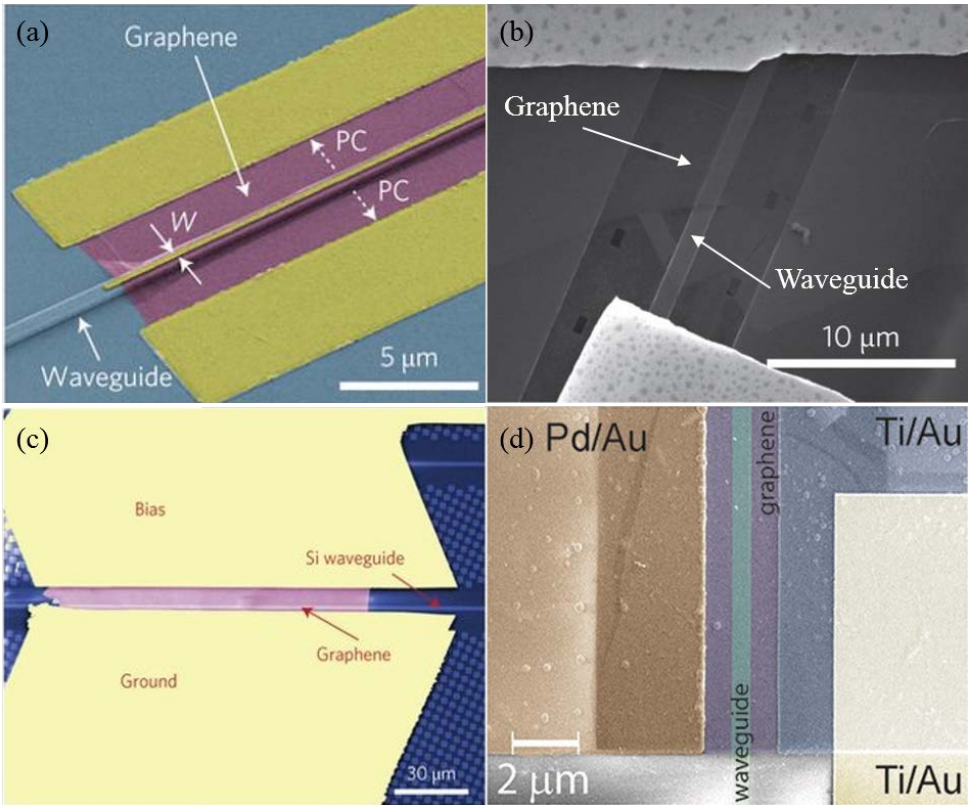

Figure 2.3 Four different types of waveguide-integrated graphene photodetectors. (a) Coloured SEM of a waveguide-integrated graphene photodetector. (b) SEM image of a graphene photodetector based on the SOI waveguide. (c) SEM image (false colour) of graphene photodetector with a waveguide covered by bilayer graphene. (d) SEM image of waveguide-integrated graphene photodetector. Images adapted from [40, 67, 76, 78].

In contrast, both microcavity[71] and photonic crystal cavity[72, 79] can realise an extremely compact photodetector, but at the cost of a reduced detection bandwidth, which is determined by the Q factor of the integrated cavity. Furchi et al. from University of Zurich achieved a Fabry-Perot cavity integrated graphene photodetector (see Figure 2.4 (a)), with a 26-fold enhancement compared to without a cavity. This order of enhancement is attributed to the multiple graphene-light interactions in the cavity. At the same time, the integration of a graphene photodetector with a silicon photonic crystal cavity (see Figure 2.4 (b) and (c))

has been separately achieved by two research groups [72, 79]. Although there is the limitation of the small operation wavelength range, this integration scheme could potentially be employed to fabricate graphene photodetectors and modulators with ultrasmall footprint and ultrahigh modulation speed.

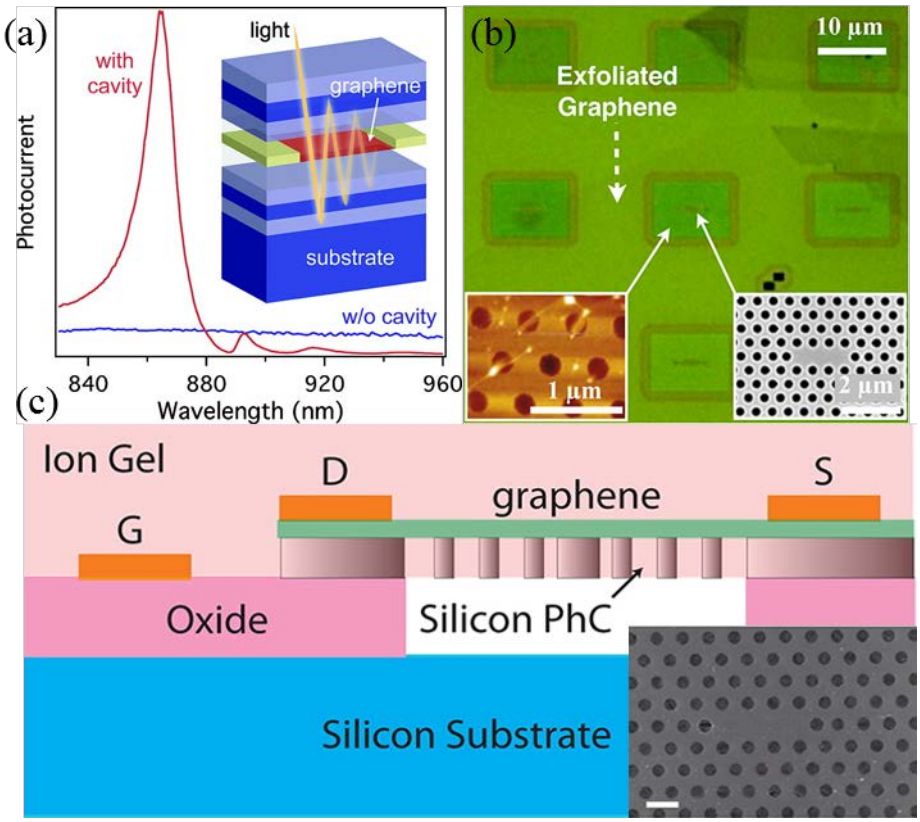

Figure 2.4 Cavity-integrated graphene photodetectors. (a) Photocurrent spectra of a graphene photodetector with (red line) and without (blue line) a Fabry-Perot cavity. Inset: Schematic of the graphene photodetector inside a cavity. (b) Optical microscope image of a photonic crystal cavities integrated graphene photodetector. Inset: AFM image of the device (left), SEM image of the device (right). (c) Schematic of the photonic crystal cavity-graphene photodetector. Inset: SEM image of the device. Scale bar is 500 nm. Images adapted from [71, 72, 79].

Alternatively, another way to enhance the interaction between graphene and light is to utilise surface plasmon polaritons[73, 75, 80-83] (see Figure 2.5). By integrating with plasmonic nanostructures, the very low external quantum efficiency problem of graphene photodetectors can be effectively solved and efficiency can be enhanced by up to 1500% [73]. Moreover, wavelength and polarisation selectivity can also be achieved by designing plasmonic nanostructures of variable resonance frequencies. Additionally, this kind of device

exhibits a very fast response speed as high as 1 MHz, demonstrating a potential application in the area of high frequency optical singal sensing.

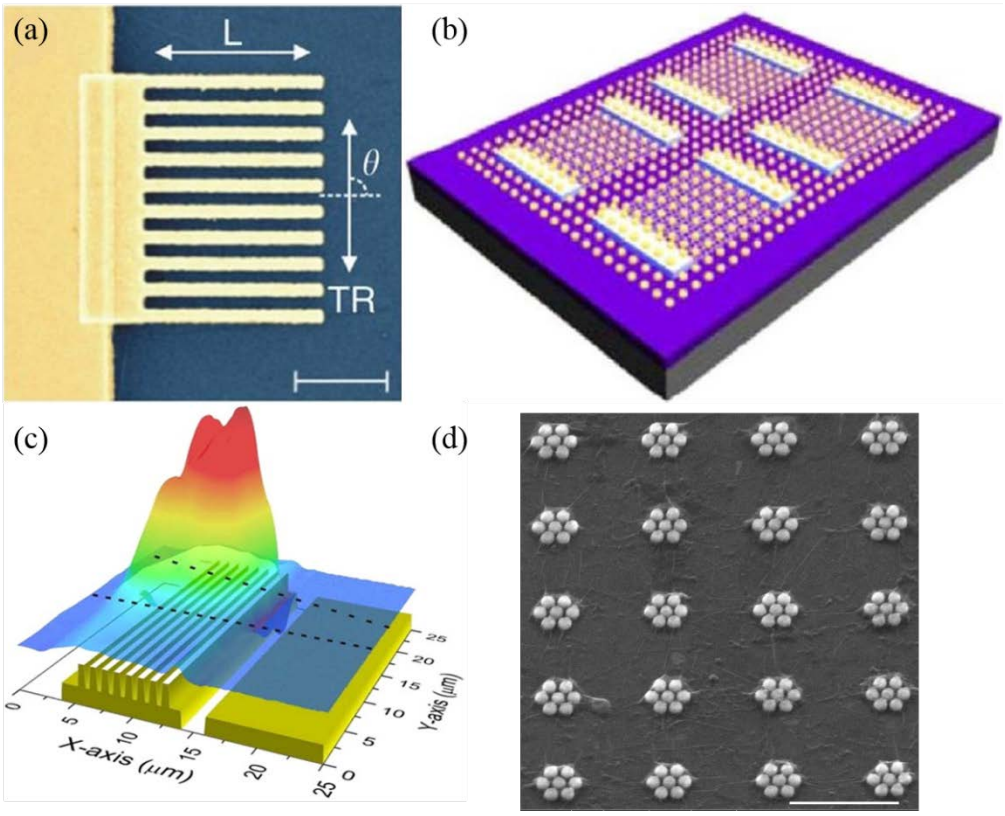

Figure 2.5 Graphene photodetectors integrated with plasmonic nanostructures. (a) SEM image of graphene with gold grating nanostructure. Scale bar is 1μm. (b) Schematic of graphene photodetector integrated with gold nanoparticles arrays. (c) Schematic of plasmonic grating-graphene structure and its simulated absorption distribution. (d) SEM image of fabricated heptamer array on graphene layer. Scale bar is 1 μm. Images adapted from [73, 75, 82, 83].

2.3.2 Quantum dots integration

Although the previous reviewed graphene photodetectors integrated with waveguides, microcavities and plasmonic nanostructures can be improved by enhancing graphene absorption, these solutions could not provide a mechanism for obtaining the photoconductive gain, which is the process of generating multiple charge carriers per single incident photon. This can significantly improve photodetection responsivity, which is crucial for highly sensitive photodetection.

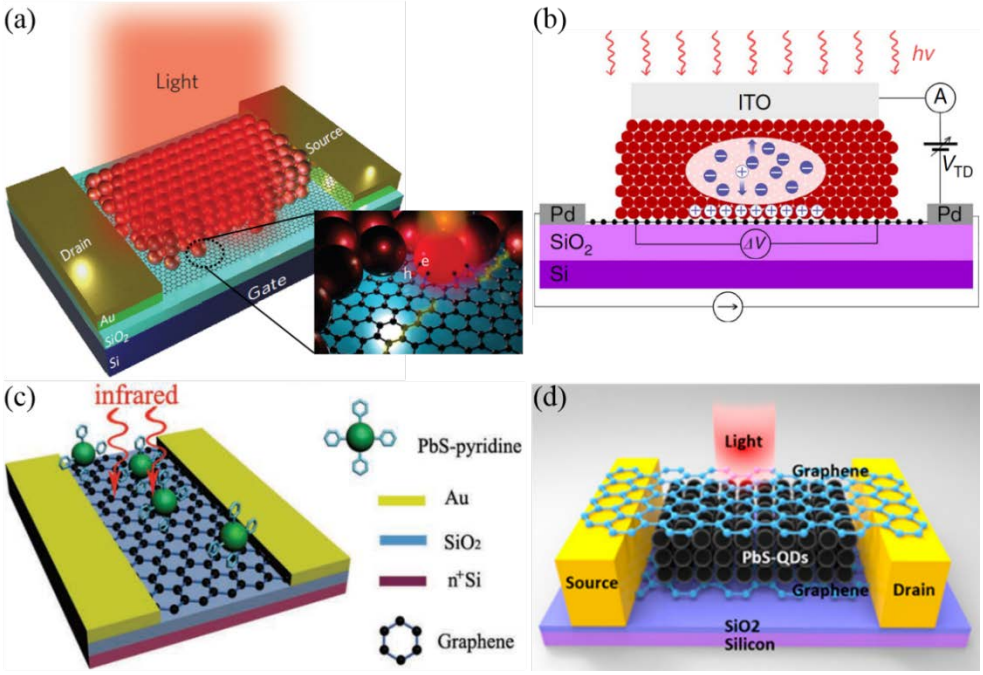

Figure 2.6 Graphene photodetectors integrated with quantum dots. (a) Schematic of graphene-quantum dots hybrid photodetector. Inset: Illustration of electron-hole pairs generation with illumination of light. (b) Schematic of QDs-graphene phototransistor operation. (c) Diagram of graphene transistor with modification of PbS quantum dots under light illumination. (d) Schematic of hybrid graphene/PbS-QDs/graphene photodetector. Images adapted from [62, 64, 84, 85].

A new route to drastically improve the responsivity of graphene photodetectors is using colloidal quantum dots[62, 64, 84-86], which possess the advantages of a long exciton lifetime, large exciton energy and strong confinement effect[87]. This innovative work had been pioneered by Spanish researchers, who exploited favourable electrical properties of graphene layer and extraordinary optical properties of quantum dots to deliberately design this hybrid structure (as shown in Figure 2.6 (a)). A gain of approximately 10^8 electrons per incident photon and a responsivity of approximate 10^7 A/W were achieved in this work. However the response time of this device is in the order of 10 seconds.

In summary, graphene photodetectors enhanced by external structures or materials possess the advantages of high responsivity and deliberate selectivity of detection wavelength. However, some also suffer from large device area, narrow bandwidth and ultraslow response speed. Therefore, there is still significant room for improvement in graphene photodetectors.

2.3.3 Graphene nanostructures for photodetection

In contrast to geometry modification, which solves the problem of how to improve absorption efficiency, material engineering regulates the intrinsic electronic and optical properties of graphene. In terms of single layer graphene, material engineering can be classified as shaping graphene and chemically doping graphene. Regarding photodetectors based on chemically doping graphene, there is a few published literatures[88] and they all investigate and explain from the chemical point of view. Here, I focus on the research of graphene photodetectors from the physical point of view and therefore, mainly concentrate on a review of graphene photodetectors based on shaped graphene platforms in this section.

Shaping graphene is the process of structurally reshaping the graphene to graphene nanostructures, such as graphene nanoribbons (GNRs)[89-93], graphene quantum dots (GQDs)[94, 95] and GNMes (GNMs)[96, 97].

GNR is the first and most extensively investigated shaped graphene pattern. The most important advantage of GNR over pristine graphene is that it possesses a width-dependent band gap, which results from the atom symmetry breaking[98-100]. The emergence of a band gap brings many benefits, such as more selective responses to incident light, higher efficiency of exciton extraction and increased separation of electron-hole pairs. Furthermore, it shows reduced heat transport ability[101] that can exert a PTE effect in most cases.

The work[102] based on GNRs with band gap of 50meV proposed by Ryzhii et al. shows responsivity as high as $250AW^{-1}$ under bias of 5V. The infrared GNR photodetector proposed by Chitara et al. gives responsivity of $1AW^{-1}$ under the bias of 2V with incident light of 1550 nm[103]. However, the GNR array photodetector at the infrared wavelength can be further enhanced by combining the graphene plasmons effect[104], as shown in Figure 2.7 (c). Freitag et al. demonstrated a polarisation-sensitive and gate-tunable photodetector based on GNR array with 100nm width and spacing. The photons interact with the plasmon-phonon quasiparticles when the incident infrared falls on the structure. Compared with the pristine graphene photodetector, this structure has a sixfold enhancement in photoconductivity. Moreover, this work paved the way for light-sensitive and frequency-selective graphene photodetectors.

Another similar type of patterned graphene for photodetection is GQDs[63, 105, 106] as shown in Figure 2.7 (a). Because of the quantum confinement effect, this graphene pattern

has band gap as well. In addition, the edge of these GQDs which act as the midgap states bands (trapping states), plays a very important role in improving responsivity. Under incident light of 532nm and external bias of 0.1V, responsivity as high as 8.6AW^{-1} was achieved in this regime, but at the expense of very low operation speed due to the introduction of trapping states. In the solutions given by the authors, reponse speed performance can be elevated by reducing the disorders and defect density or by exploring other patterns such as nanoribbons and nanomeshes.

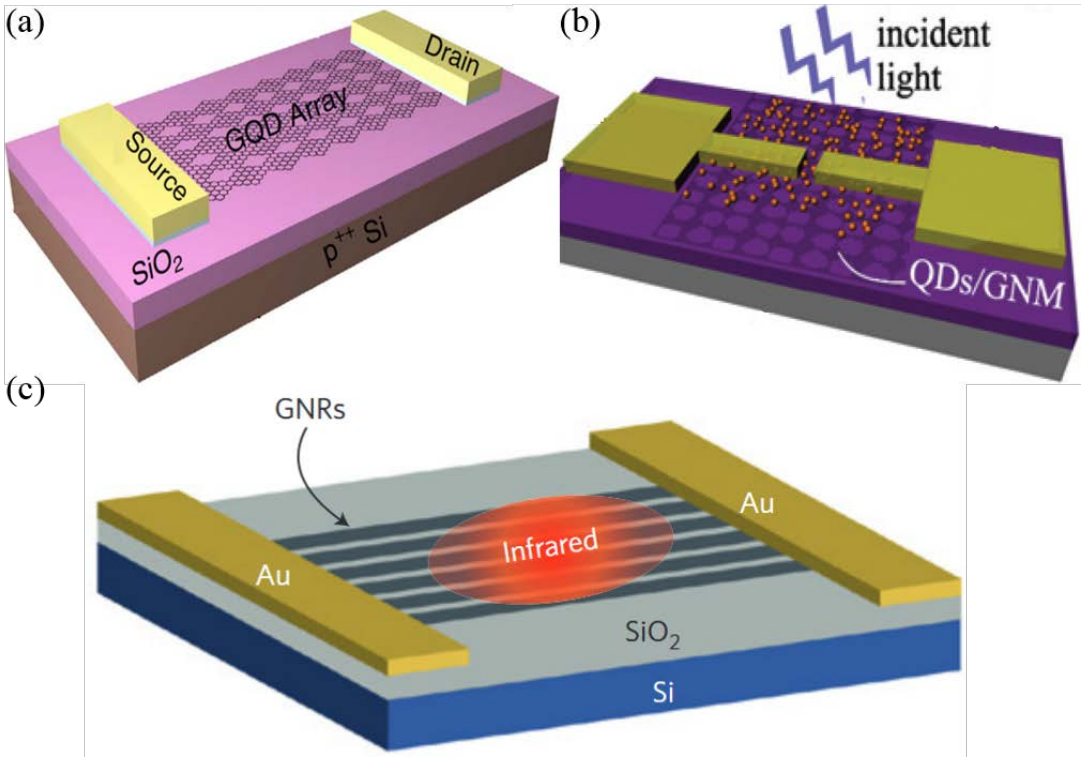

Figure 2.7 Schematic of photodetectors based on graphene pattern structures. (a) Structure diagram of photodetector based on GQDs array. (b) Schematic image of a GNM/QD FET photodetector. (c) Schematic of a photodetector based on graphene nanoribbons. Scale bar is 2 μm. Images adapted from [63, 104, 107].

GNM[96] is another graphene pattern that has band gap dependent on its dimension[108, 109]. Many novel fabrication methods have been proposed[96, 110-112] but little attentions has been paid to photodetection based on GNM. Liu et al. recently demonstrated their work on a GNM/QDs hybrid photodetector[107] by laying CdSe QDs on the nanomesh (see Figure 2.7 (b)). The responsivities range from 34 AW^{-1} to 2700AW^{-1}, with incident light 400 nm and bias of 30 mV obtained under different circumstances.

In summary, graphene photodetectors have achieved remarkable results with great promise for various applications even compared with the well-developed silicon-based photodetectors. However, the scope to improve graphene photodetection performance through material engineering is far from exhausted, especially in the area of GNM and due to recent developments in graphene plasmons. Thus, this is an exciting field, and we seek to explore the deep mechanism of graphene plasmons enhanced photodetectors based on GNM structures.

Table 2.1 summarises the representative photodetectors based on graphene and their key parameters.

Methodology	Materials	Operation wavelength	Responsivity	Representative reference
Dual-gate	Monolayer graphene	632.8 nm	1 mA/W	56
Integrated with photonic structures	Monolayer or bilayer graphene	830-900 nm 1450-1590 nm 400-700 nm	21 mA/W 108 mA/W 6.1 mA/W	40,66, 67, 70,71,72,74,75
Hybrid	Graphene and quantum dots	532 nm,1050 nm,1600 nm	5*10^7 A/W	61,63,82,83
Shaped	Graphene nanoribbon or nanomesh	1550 nm 532 nm	250 A/W 8.6 mA/W	62, 98,99,101,102

Table 2.1 Representative photodetectors based on graphene.

2.4 Graphene plasmonics

Over the past decades, much research interest has been focused on the study of noble metal plasmons, which can be used extensively in near infrared and partly in the visible, with dominant materials silver and gold. However, the search for new materials is imperative because of noble metals' high intrinsic optical loss and low confinement. Since it was sucessfully exfoliated in 2004, graphene has emerged as a prominent candidate, for its remarkable electrical and optical properties. As a good conductive 2D material, graphene has been theoretically predicted[113] and demonstrated in experiments[114-117] to support surface plasmons ranging from terahertz to infrared, which can help to bridge the so-called THz gap. Furthermore, graphene plasmons has advantages when compared with the surface

plasmons supported by noble metals. First, graphene plasmons possess a highly desired feature of tunability for a given structure as the carrier density can be tuned by electrostatic (gating) or chemical doping. Second, the very high carrier mobility gives graphene plasmons the properties of long life time and low loss which can produce longer propagating length. In addition, there are other benefits, such as compatibility with current CMOS technologies and extreme light confinement. In the following section, I illustrate the theory basis and quantitative analysis of graphene plasmons.

Because of the momentum mismatch, graphene plasmon polaritons on pristine graphene cannot be directly excited with incident light[116, 117]; however, localised graphene plasmons supported by patterned graphene structures can be excited directly. Many remarkable properties of localised graphene plasmons are demonstrated in the different structures such as GNR[118-120], nanorings[121]and nanodiscs[122-124]. I briefly review localised graphene plasmons in patterned graphene nanostructures in this section [125] as our proposed and investigated graphene photodetectors are enhanced by graphene plasmons. Generally, the semi-classical theory is accurate enough to describe the properties of localised graphene plasmons as long as the scale of patterned graphene structures are above several tens nanometres[126], for example, 20nm for nanodiscs and 10nm for nanoribbons. Otherwise, the quantum effect should be considered, which can lead to fascinating results compared with the plasmons supported by pristine graphene.

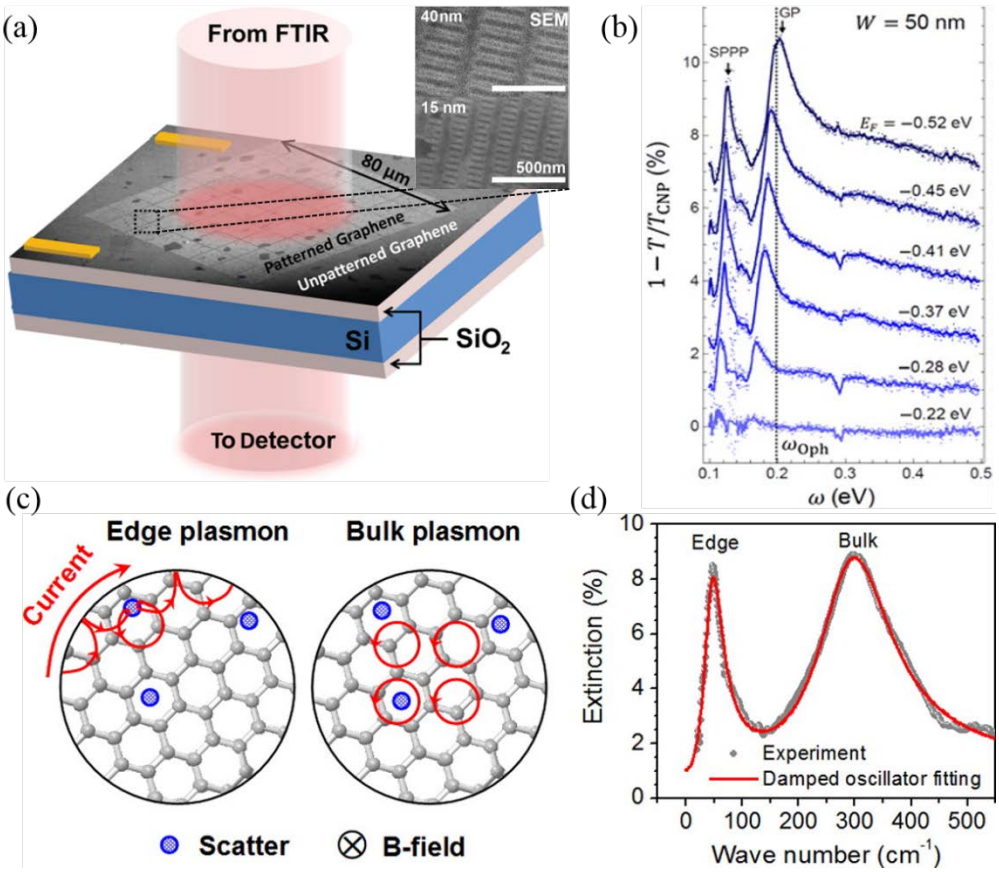

Figure 2.8 Photodetectors enhanced by graphene plasmons that supported by graphene nanostructures. (a) Schematic graphene nanoribbons plasmons device. Inset: SEM image of graphene nanoribbon array. (b) Measured optical transmission through 50 nm wide graphene nanoribbons with varying Fermi level. (c) Schematic depiction of charged carrier motion for edge and bulk plasmon modes in graphene nanodisc structures. (d) Experimental extinction spectrum of a sample. Images reproduced from [120, 123].

As discussed in the previous chapter, GNRs are one of the first and most widely investigated graphene patterns as they can be easily created. Due to the reduction of freedom in electron cloud oscillation, the plasmons in GNRs have polarisation sensitivity and can have a very high enhancement of absorption because of the creation of resonances (see Figure 2.8 (a)). Another prominent characteristic is its ribbon-width-dependent band gap, which has important implications in the fields of metamaterial and photodetection, among others. The study of plasmons in graphene nanodiscs and nanorings was performed by Hu et al.[122, 127] showed the EM field in the structures behaved like a dipole. Furthermore, the enhancement of plasmons in graphene nanodiscs is very strong for its zero dimensional nature, as shwon in Figure 2.8 (d). Although there are broad application prospects and some research has been

published, the properties of plasmons in patterned graphene structures are yet to be thoroughly investigated, motivating the current study.

In summary, surface plasmons and graphene have become very prominent research fields in recent years. Their hybridisation, graphene plasmons, are set to become a hot spot in the fields of nanoelectronics and nanooptics, among others. This field has not been extensively investigated and more effort is required, prompting the research of this project and investigate its relative applications.

2.5 Surface plasmons absorption and photocurrent enhancement

Controlling light on scales much smaller than incident light wavelength is one of the most prominent advantages of surface plasmons. This has also prompted the development of nanoscale optoelectronics. Due to their unique optical properties, surface plasmons exhibit many potential applications in subwavelength optics, such as near-field optics, SERS, solar cells, sensors and photodetectors. Among these, surface plasmon absorption enhancement plays a very important role. Hence, in this section I provide an introduction to surface plasmon absorption enhancement in graphene photodetection.

Conventional metal surface plasmons were the first to be used to enhance light absorption in graphene photodetection. The mechanism is that the excited surface plasmons at resonant states strengthen the interaction between graphene and light by creating regions of highly enhanced electric field. Therefore, graphene photodetectors absorb much more incident light than pure graphene structures and hence, surface-plasmon-enhanced photodetectors show higher responsivities compared with pure graphene photodetectors.

All graphene photodetectors enhanced by metal surface plasmons are reviewed in Section 2.3. Here, we only emphasise the enhancement of absorption or photocurrent, as shown in Figure 2.9. With these deliberate designs, there is normally at least one order of magnitude enhancement for the photocurrent; for example, the heptamer array metal structure gives 80 times improvement of photocurrent compared to without this metal structure in reference [75]. In addition, wavelength and polarisation selectivity can also be achieved due to the wavelength and polarisation sensitivity of the plasmonic structures at resonant states.

However, the corresponding disadvantage is that the resonant state cannot be changed externally for a fixed plasmonic structure, which means different plasmonic geometries must be designed and fabricated to achieve resonance at the desired resonant wavelength. This situation is not cost-effective, is non-tunable and a waste of resources for the surface plasmons supported by costly noble metals.

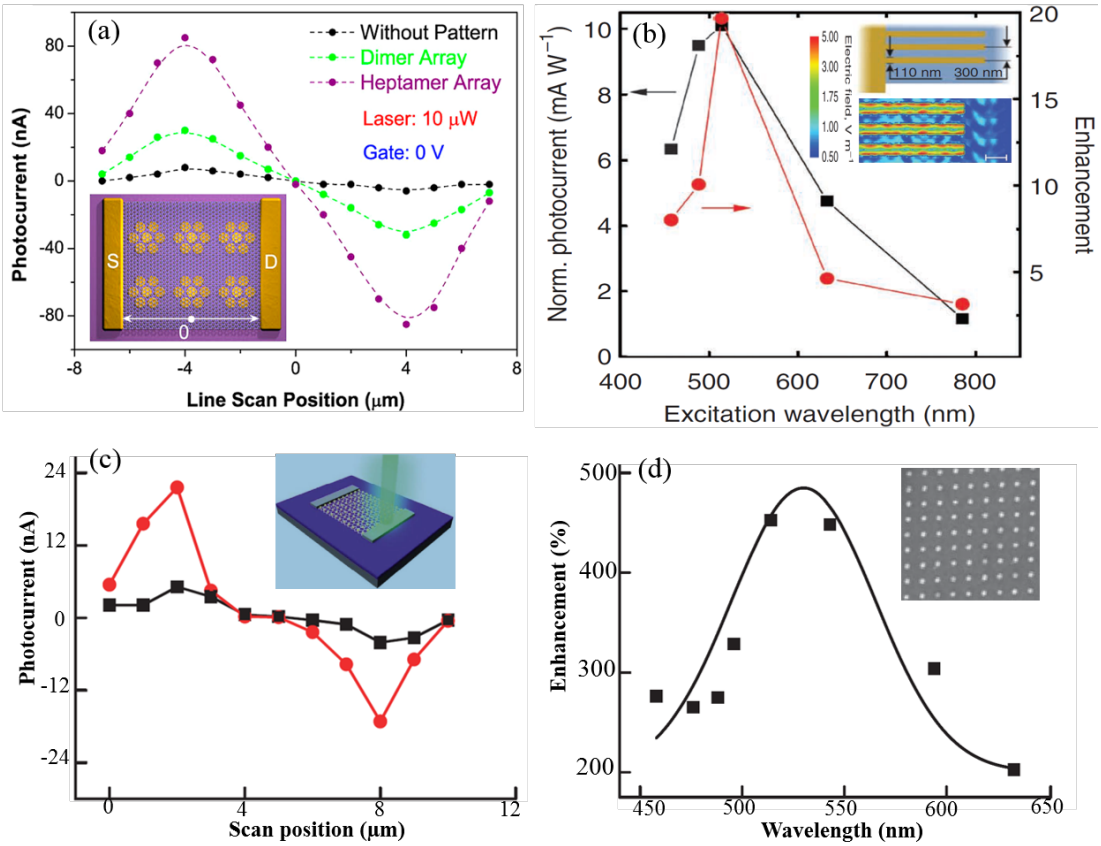

Figure 2.9 Enhanced photocurrent by conventional surface plasmons in different graphene photodetectors. (a) Photocurrent profiles of antenna-graphene sandwich devices(inset) for different geometries. (b) Normalised photocurrent and related enhancement measured as a function of excitation wavelength for finger structure of a 300 nm pitch and 110 nm finger width. Inset: Schematic of finger structure and its simulated electric field distribution at excitation of 514 nm. Scale bar is 300 nm. (c) Photocurrent profiles with scanning from source electrode to drain electrode of a graphene photodetector with (red line) and without (black line) Au nanoparticles. Inset shows the schematic of a graphene photodetector with Au nanoparticles. (d) Measured photocurrent enhancement spectrum for the device with Au nanoparticles. Inset: SEM image of gold nanoparticles array. All images adapted from [75, 82, 104].

In research on graphene physics, graphene can also be a very prominent platform supporting surface plasmons [114, 116, 117, 128] for its remarkable optical and electronic properties.

Most importantly, the sensational benefit of intrinsic graphene plasmons is that gate voltage can dynamically tune it. Furthermore, it also has the benefits of extreme light confinement, low Ohmic loss, and abundance of nontoxic carbon.

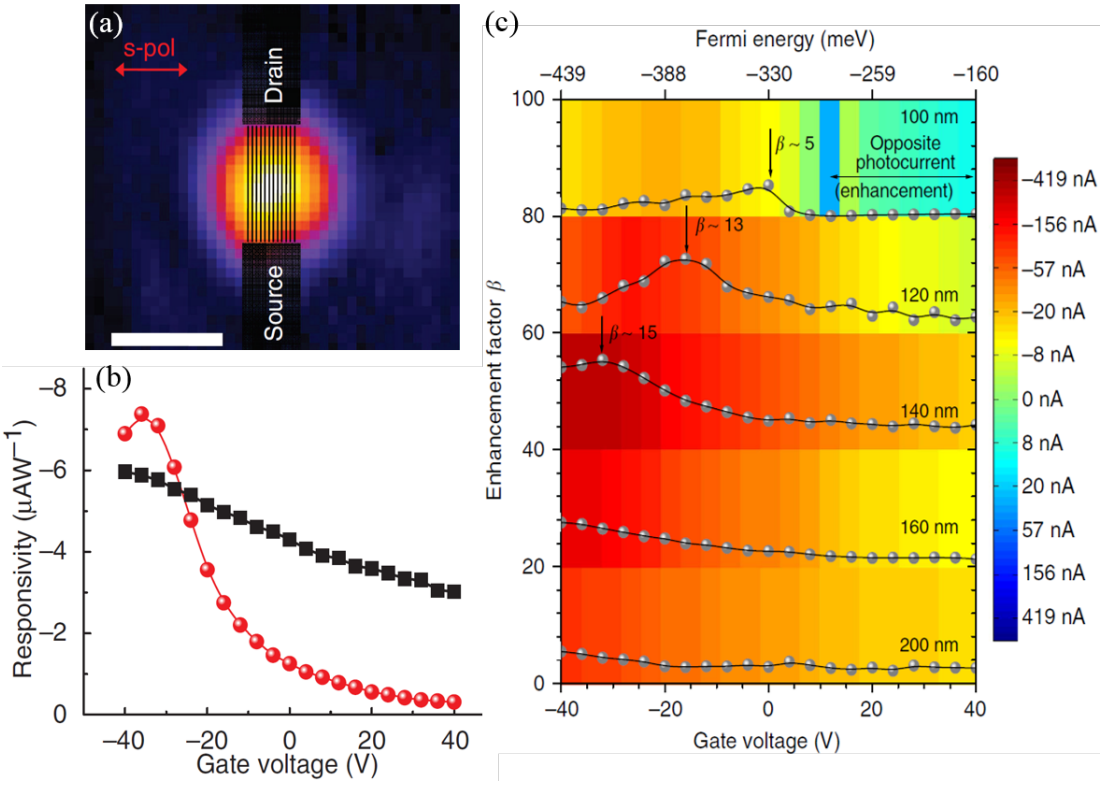

Figure 2.10 Enhanced photocurrent by graphene surface plasmons. (a) Scanning photocurrent image of a graphene nanoribbon superlattice photodetector. Scale bar is 30 μm. (b) Responsivity of graphene photodetectors for 140 nm graphene nanoribbon superlattice (red spheres) and pristine graphene (black squares) upon same excitation (laser power is 66mW and bias voltage is -2 V). (c) Photocurrent enhancement factor $\beta = \left|I_{90^\circ}/I_{0^\circ}\right|$ as a function of gate voltage and graphene nanoribbon width. Images adapted from [104].

With the convenient excitation of graphene plasmons supported by nano structures with incident light, photodetectors based on graphene nanostructures have been extensively investigated. There is a seven-fold enhancement of the photocurrent due to the function of graphene plasmons. Figure 2.10 (b) shows the photocurrent response of a GNR photodetector. It is evident that there is an approximate 35% improvement compared with the pristine graphene photodetector when the gate voltage is above negative 30 volts. Furthermore, the evident polarisation sensitivity (see Figure 2.10 (c)) can be used for the detection of polarised light.

Although the topic of intrinsic graphene plasmon-enhanced photodetection is prominent, few papers have been published and it has not been extensively investigated. This section has noted that intrinsic graphene plasmons can introduce many benefits, such as polarisation sensitivity and band gap for photodetection. Therefore, we add to the research body by investigating graphene photodetection enhanced by graphene plasmons in graphene nanostructures.

2.6 Graphene bandgap engineering

In the previous chapter, I provided a brief introduction to bandgap engineering of single-layer graphene. In this section, I provide a thorough review of the published literature on bandgap engineering of graphene. In addition, I review the surface plasmon absorption enhancement literature. These reviews comprise the theoretical basis of the method for improving responsivity and restricting the dark current in our proposed structures.

Bandgap (also called band gap or energy gap) is an energy range in a solid where no electron states can exist. In the diagram of the electronic band structure of a solid, the bandgap generally describes the energy difference between the bottom of the conduction band and the top of the valence band. According to band energy theory, all the materials can be categorised as metal, semiconductor or insulator based on the size of the bandgap (see Figure 2.11 (a)). Because the bandgap is equivalent to the energy needed for an outer shell electron to break free out of the atom, it is a major factor determining the electrical conductivity of a solid. Hence, controlling the bandgap of one material allows us to design its electrical properties.

Graphene, the first and most fully investigated 2D material, has enormous potential in electronics and photonics because of its remarkable electronic and optical properties. First, both the electrons and holes have ultrahigh charge carrier mobility ($> 10^5$ $cm^2V^{-1}s^{-1}$) due to the linear energy dispersion relationship around the Dirac cone. Second, the optoelectronic properties of graphene can be dynamically tuned by controlling its Fermi level via chemical doping or external gate voltage. However, graphene is a gapless semiconductor or semimetal (as shown in Figure 2.11 (b)), which can lead to the low separation rate of the electron–hole pair and high dark current for the photodetection area. Therefore, the introduction of a bandgap for the photodetection platform, graphene, is vital.

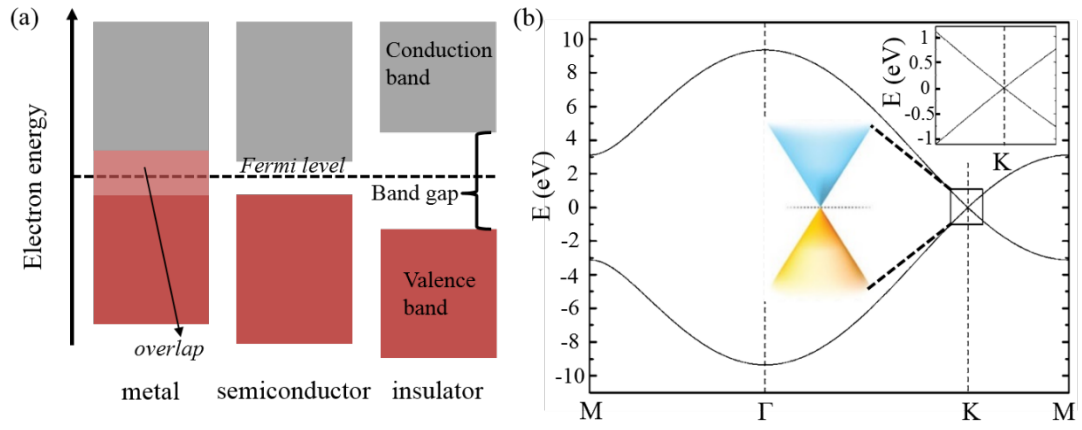

Figure 2.11 (a) Schematic of electronic band structure of metals, semiconductors and insulators. (b) Electronic band structure of single layer graphene. Image(b) adapted from [129].

There are several ways to open the electronic band structure of graphene, such as a substrate induced band gap[130-132], bilayer graphene structure[133-138], or patterned graphene nanostructures[109, 139-144]. Here, we mainly review the mechanisms of band gap engineering through the methods of monolayer graphene pattering and double layer stacking.

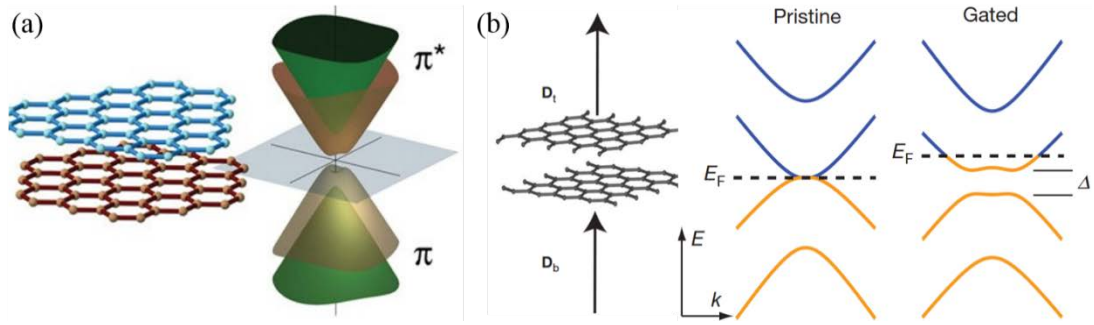

Figure 2.12 (a) Electronic structure of an asymmetric double layer graphene. (b) Schematic showing how gating of a bilayer graphene induces top (D_t) and bottom (D_b) electrical displacement fields (left) and electronic band structure of a pristine (middle) and gated (right) bilayer graphene. Images adapted from [133, 134].

Band gap engineering in bilayer graphene was first proposed and investigated in 2006[133]. Scientists in advanced light source in University of California, Berkeley characterised the electronic band structure and successfully controlled the band gap in a bilayer graphene film,

which deposited on the substrate of silicon carbide using angle-resolved photoemission spectroscopy. As shown in Figure 2.12 (a), there is a band gap in the asymmetric double layer graphene. They introduced symmetry breaking by doping one sheet with adsorbed potassium atoms; moreover, they predicted that similar control could be achieved by varying the electric field across the bilayer graphene film.

Two years later, researchers from the same institute published work on tunable band gap in electrically gated bilayer graphene on nature[134] (see Figure 2.12 (b)). By using a dual-gate bilayer graphene FET and infrared microspectroscopy, they exhibited gate-controlled continuously tunable bandgap of up to 250meV. From their thorough theoretical analysis, the bandgap results from the inversion symmetry were produced by electrical gating, which has the benefit of external tunability, very prominent in optoelectronics applications.

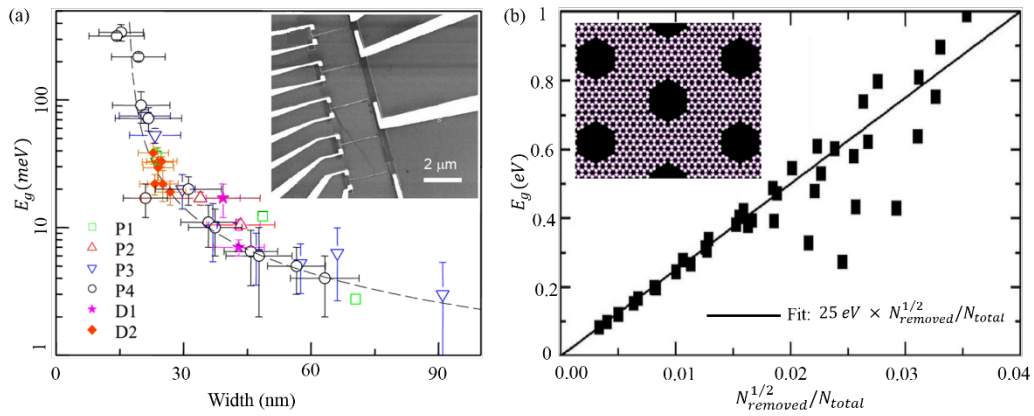

Figure 2.13 (a) Width dependent band gap of graphene nanoribbons for 6 device sets. Inset: SEM image of device with parallel graphene nanoribbons of varying width. (b) Calculated energy band gap for GNM structure. Inset: Sketch of a GNM structure with triangular arrangement of defects. Images adapted from [140, 145].

In contrast to use bilayer graphene structure, material modification (periodic patterning) of single layer graphene including using defects, passivation, doping and nanoscale perforation is another method to introduce a band gap. Because of its easy preparation and remarkable properties, GNRs[98] have become a research hotspot in band gap engineering and related appliaction. The lithographically patterned graphene ribbon structure possesses an energy gap near the charge neutrality point because of the lateral confinement of charge carriers. In the following, graphene nanodisc, GQDs and GNM are investigated. The role of electronic structures of all periodic patterned structures is the confinement effecting charge carriers.

Nearly all theoretical calculation and analysis in the published literatures are based on tight-binding modelling and first principles calculation. Regarding energy band structure, theoretical work is profound and complex. Hence, here, I provide only a brief review and the main explanation rather than reviewing all the theoretical work.

2.7 Chiral photodetection

The major aim of this thesis is to design, fabricate and characterise novel graphene photodetectors working in the MIR spectra range. One particular important point concerns MIR spin angular momentum detection with chiral plasmonic structures. In this section, we review the published related work and propose our own design, starting with sample fabrication and related characterisation work.

Chirality is a geometric property referring to a structure for which the mirror image cannot be translated or rotated back onto itself. This property exists in many forms in nature, such as molecules, proteins and crystals. Chiral geometries can produce intriguing chiral-optical effects, such as CD, widely used in optical rotators, optical isolators and biological spectroscopy. CD is the differential absorption of left circularly polarised (LCP) and right circularly polarised (RCP) light. However, CD is very weak in natural materials/structures, and therefore, the chiral effect is detectable only when the optical path length is much larger than the wavelength of light, inhibiting the development of compact chiral-optical devices.

Before exploring the methodology to obtain a chiral structure possessing high CD, we need to present the physical mechanism behind the chiral-optical property. Since in electromagnetics, a chiral medium is one kind of bianisotropic media where the electrical and magnetic fields are coupled together, its optical response is described via the following relations:

$$\vec{D} = \varepsilon_0 \varepsilon_r \vec{E} + \frac{i}{c_0} \gamma \vec{H} \tag{2.4}$$

$$\vec{B} = -\frac{i}{c_0} \gamma \vec{E} + \mu_0 \mu_r \vec{H} \tag{2.5}$$

Here, ε_r, μ_r and γ are the permittivity, permeability and chirality tensors, respectively. ε_0 and μ_0 are the permittivity and permeability of vacuum. $\vec{E}$ and $\vec{H}$ are the electric field and magnetic field, and $\vec{D}$ and $\vec{B}$ are the electric displacement and magnetic induction.

According to the two equations above, the refractive index n, defined as the ratio between the speed in vacuum and speed of light in medium for the right-handed (+) and left-handed (-) circular polarisations are given by

$$n_{\pm} = \sqrt{\varepsilon\mu} \pm \gamma \tag{2.6}$$

From the equation above, it is evident that the two different circular polarisations have different absorption (i.e., different CD due to the different refractive index) when ε μ and γ are complex.

As chiral response is weak in natural materials, the development of compact and effective photonic polarisation devices is urgent.

Past decades have seen the development of engineered plasmonics nanostructures that can support surface plasmon polaritons, opening an avenue to achieving compact functional circular polarised devices on a subwavelength scale. At the resonant state, there is several orders of magnitude increasement in local electric and magnetic field. In 2007, Fedotov et al. proposed and demonstrated that a plane metal nanostructure consisting of chiral fish-scale units can achieve a maximum CD up to 25% from the visible to near-IR spectra region[146].This new effect associated with the enantiomerically sensitive plasmon is fundamentally different than the gyrotropy of the bulk chiral medium and the Faraday effect. This work showed a new perspective on CD detection based on surface plasmons polaritons supported by a 2D chiral structure.

In 2009, 2D Archimedean plasmonic spirals[147] (see Figure 2.14 (c)) were proven to have capabilities for circular polarisation analysing. Within that structure, a circular polarisation extinction ratio above 100 was obtained with a lateral size of the spiral device as small as $4\lambda_{spp}$. Although different transmission patterns corresponding to left or right circular polarised light can be identified by the intensity distribution, the total transmission energy of different polarisation states is indistinguishable.

Following research investigated chiral split rings, rod dimers and chiral networks[148, 149], Zhukovsky et al. theoretically calculated and numerically simulated the relationship between the strength of chiral properties and dimer geometrical parameters. In the coupled dipole analytical approach, the symmetric rod dimers are achiral while the structures with most distinct 2D enantiomers have the most pronounced chiral properties.

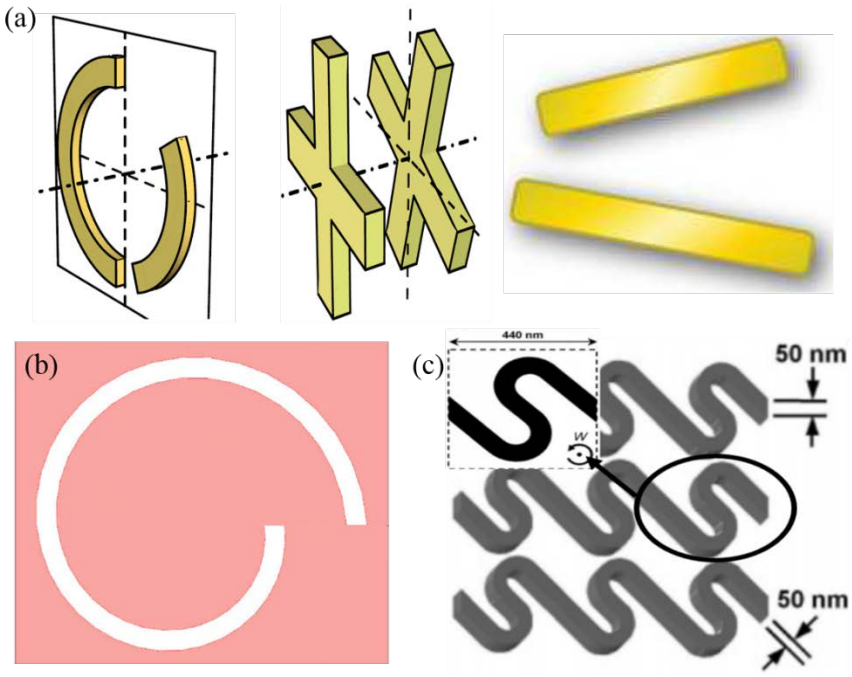

Figure 2.14 Schematic of chiral structures. (a) Examples of 2D (left) and 3D(middle) enantiomeric structure and geometry of an arbitrary planar rod dimer. (b) Diagram of a left-hand single-turn Archimedes' spiral. (c) Sketch of the chiral fish-scale structure and its unit cell shows in inset. Images adapted from [150-152].

Following the concept of 2D chiral structure for CD applications, a new 2D metal chiral network formed from metal ribbons was proposed by Konishi et al. This work fabricated chiral structures with a left and right sense of twist, designed to possess a fourfold rotational symmetry axis along the substrate normal. Optical activity was clearly observed with samples of different periods for normal incidence. Moreover, the resonant enhancement of the optical activity was proven to be associated with surface plasmon resonance. Similar to the chiral network structure, the optical activity of gammadion, as shown in Figure 2.15, has been thoroughly explored, to reveal that the optical activity not only comes from the dissymmetric backing by a substrate but also from the selective rounding of the nanostructure edges.

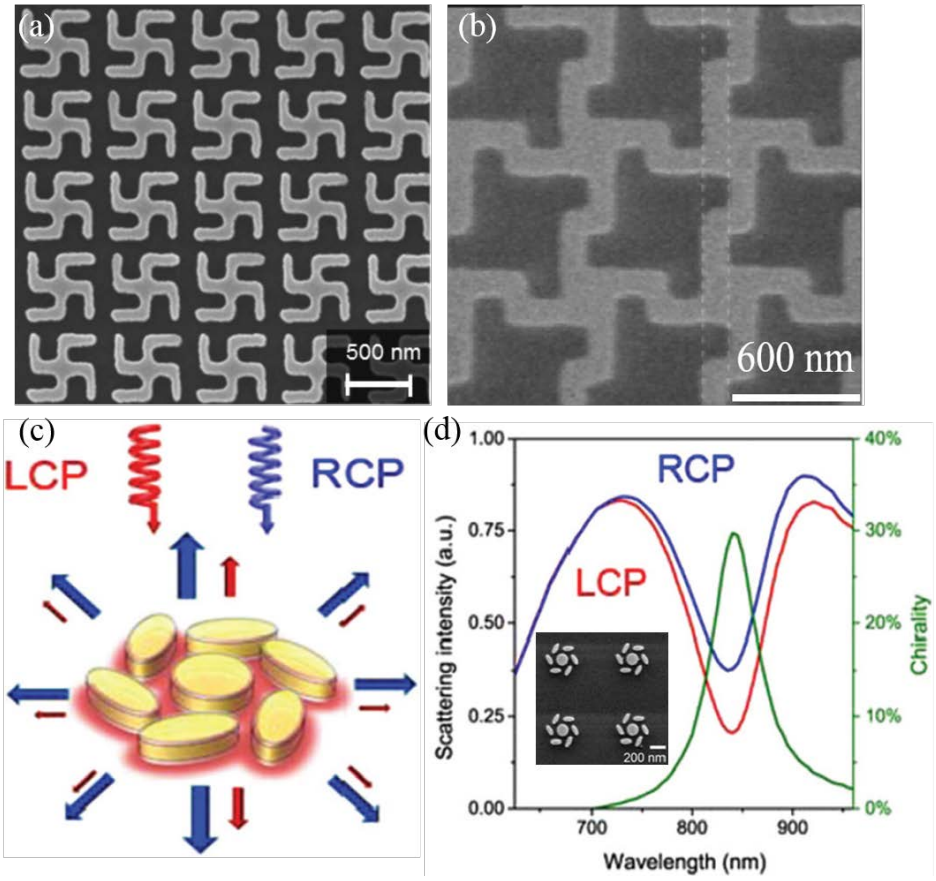

Figure 2.15 (a) SEM images of gold gammadia nanostructures. (b) SEM image of right twisted chiral network structure, 600 nm period. (c) Schematic of a chiral Fano oligomer structure under normal-incident circularly polarised light. (d) Calculated scattering cross section for LCP and RCP incident light and the resulting chirality. Inset: SEM image of heptamer array. Images adapted from [153-155].

Although many circularly polarised light detectors based on chiral plasmonics structure have been proposed and investigated, few are efficient and highly selective. In 2015, researchers from Vanderbilt University and Ohio University proposed and experimentally demonstrated an ultracompact circularly polarised light detector based on the platform of chiral plasmonics metamaterials formed by 'Z' shape silver chiral metamolecules[156]. Within this structure, the simulated CD is as high as 90% while 72% (see Figure 2.16 (c) and (d)) was experimentally achieved in a telecommunication regime. Furthermore, the chiral response can be tuned with different structure sizes across the entire telecommunication regime, offering benefits for security in fibre and free-space communication, imaging and sensing applications for circular polarised light (CPL).

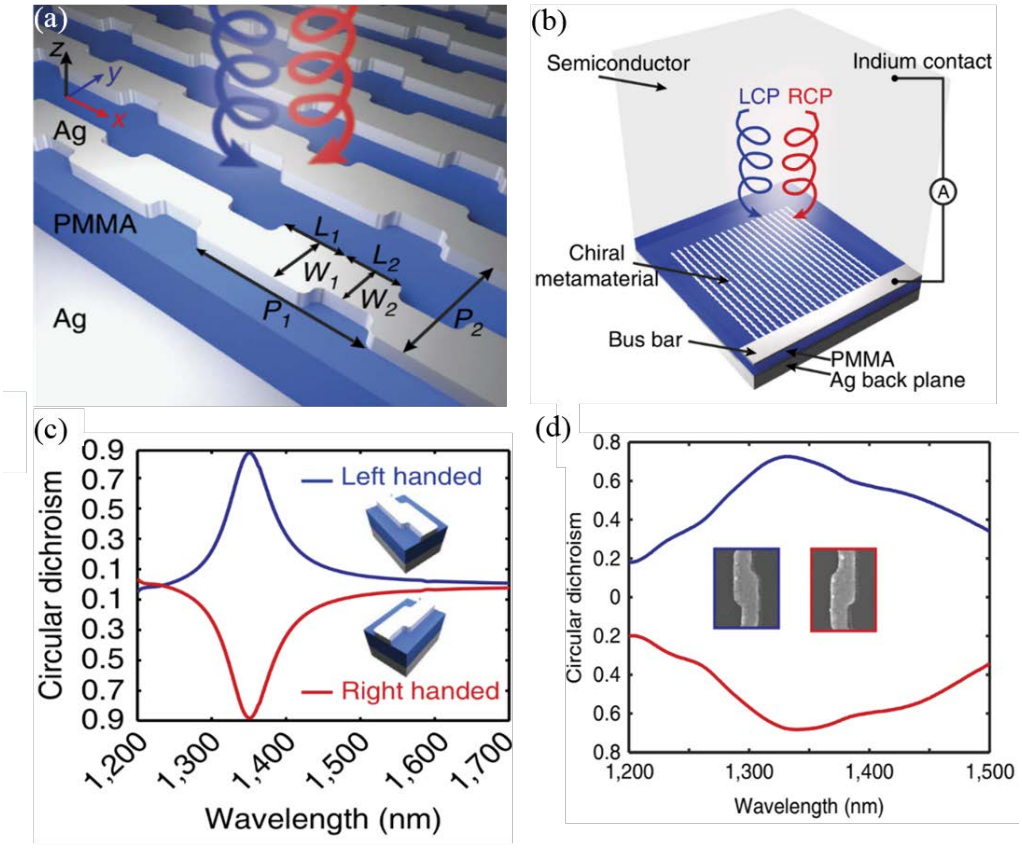

Figure 2.16 (a) Schematic of the 'z' shape chiral plasmonic structure. (b) Schematic of the CPL detector consisting of the 'z' shape chiral structure. Calculated (c) and experimentally measured (d) CD spectra for both the LH (blue) and RH (red) nanostructure. Images adapted from [156].

One year later, another new planar chiral metal structure, heptamers, was experimentally and theoretically demonstrated by Zu et al.[157]. In this work, it was revealed that the light–matter interaction in individual metallic nanostructures is dramatically enhanced by the plasmonic Fano interference. To achieve the maximum CD, inter-particle rotation angle and separation distance of the planar heptamers were engineered. Experiments showed that maximum chirality (about 30%) was recorded when rotation angle was 60° and 180°, which gave the largest structure symmetry breaking. For the relationship between chiral response and inter-particle distance, gap distance from 160 nm to 260 nm was investigated; the maximum DC of 30% was measured with the distance d decreasing to 160 nm. To explain the mechanism of this plasmonic-enhanced chirality, the coupled dipole approximation (CDA) mode and multipole mode expansion method was employed to analyse the observed chirality. In a further exploration, the excitation of magnetic quadrupolar and electric toroidal dipolar modes provided enhanced chirality in a plasmonic chiral resonance.

Although many planar plasmonic chiral nanostructures have been proposed and experimentally demonstrated and theoretical calculations show that CD relies on finite non-radiative (Ohmic) losses of the chiral nanostructures, because of the challenge of measuring non-radiative loss at the nanoscale, experimental verification was not achieved until the work of Khanikaev et al.[158]

In this work, they designed a specific plasmonic nanostructure consisting of a square array of unit cells that contains one vertical dipole nanoantenna and one horizontal monopole nanoantenna (see Figure 2.17). Scattering-type near-field-scanning optical microscopy (s-SNOM) was used to map the optical energy distribution on nanoantennas and their enantiomers under the illumination of RCP and LCP light, followed by usage of photo-expansion microscopy (AFM-IR) to experimentally demonstrate the drastically different Ohmic heating of the nanoantennas for the RCP and LCP light illumination. Based on these two direct experimental results, it is seen that optical activity in planar plasmonic nanostructure is unambiguously related to the circularly dichroic Ohmic loss caused by the circularly dichroic near-field distribution. These experimental probations and visualisations showed the first direct experimental evidence for the physical explanation of planar chiral plasmonic nanostructures, offering significant benefits for the fields of biological sensing and novel infrared optical devices.

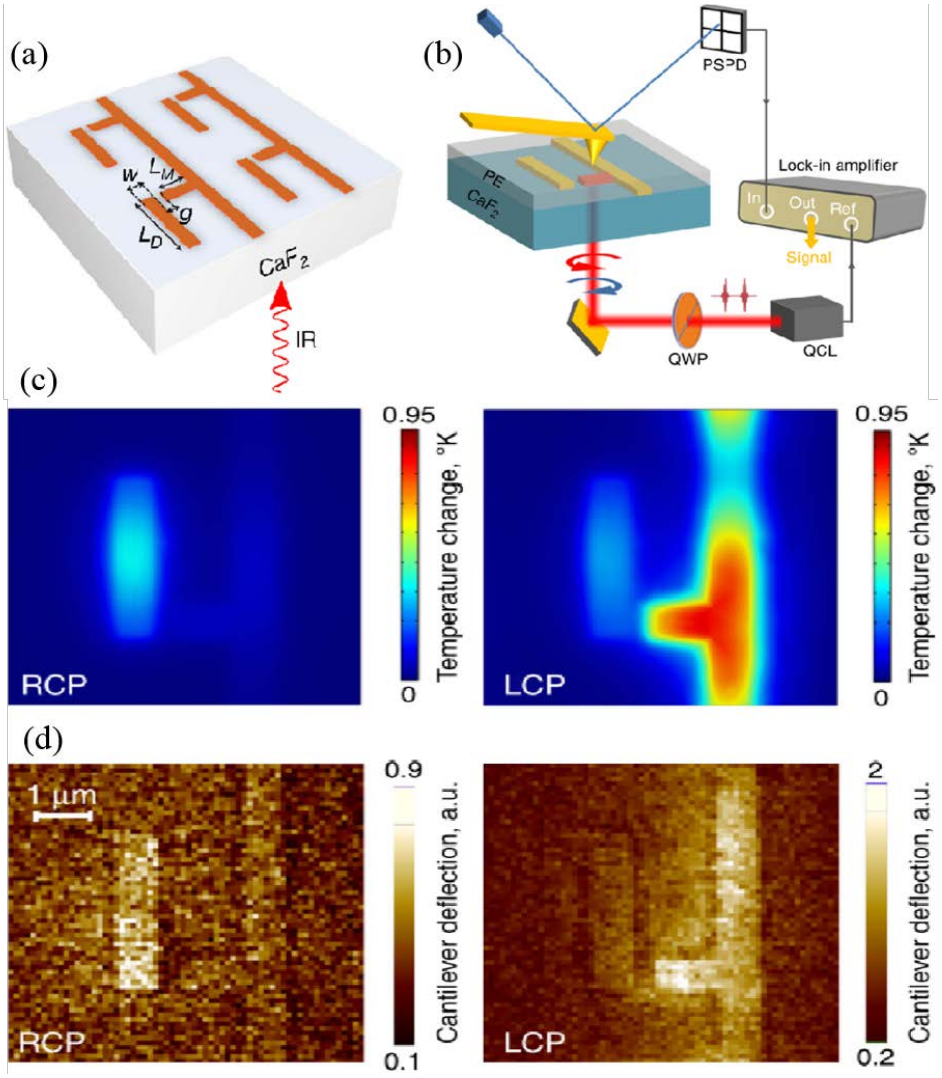

Figure 2.17 (a) Schematic of a periodic nanostructure illuminated by circular polarised light. (b) Experimental setup of the AFM-IR measurements of circularly dichroic thermal expansion. (c) COMSOL simulations of temperature increase distribution with parameters of time duration T=200ns, peak intensity I=1kWcm^{-1} and wavelength λ=9.1μm. (d) AFM-IR cantilever deflection on top of a PE-coated sample excited with circular polarised laser pulses. Images adapted from [159].

Based on the above review, Table 2.2 summarises the simulation/experimental results for circular polarised light detection with chiral plasmonics structures. It can be concluded that the zigzag shape shows the maximum absorption and CD. In addition, all the working wavelength ranges are from visible to near infrared, while there is only one work targeted at the mid-infrared wavelength.

	Max. Absorption	CD	Wavelength/ frequency	Metal	Simulation/ Experiment	Reference
Fish-scale	45%	0.28	630nm	Al.	Simulation	[152]
Archimedes' spiral	N.A.	N.A.	808nm	Au	Simulation	[151]
diamer	38%	10%	10GHz	Au	Simulation	[150]
Chira network	N.A.	N.A.	~800nm	Au	Simulation	[154]
Gammadia	N.A.	6%	600nm	Au	experiment	[155]
'z' shape	100%(simu.) 98%(exp.)	90%(simu.) 72%(exp.)	1200nm-1700nm	Ag/Al	Both	[156]
heptamer	N.A.	20%	800nm	Au	Both	[153]
Periodic metasurface	N.A.	10%	9.3μm	Au	Both	[159]

Table 2.2 Performance of circular polarised light detector with chiral plasmonics structures.

2.8 Discussion

This chapter provided a review and discussion of graphene photodetectors and graphene plasmons and the technologies and theories required in our proposed project. However, the following questions regarding graphene photodetection remain unresolved:

- To what extent can graphene absorption be enhanced by chiral surface plasmon resonances in the MIR?
- Can the enhanced absorption in graphene layer be helpful for the increasement of photocarriers?
- Can the internal electric field of graphene photodetector separate electrons in the mid-infrared?
- Can intrinsic graphene surface plasmons be used to enhance absorption in the coveted MIR regime?
- Can intrinsic graphene surface plasmons exist side by side with band-gap engineering?
- To what extent can GNM photodetection be made spectrally selective and tunable?

This PhD thesis addresses these important scientific and technological questions and lays the groundwork for the development of future graphene photodetectors.

Chapter 3

Direct detection of photon spin angular momentum by a graphene mid-infrared photodetector

3.1 Introduction

The main aim of this thesis is to overcome challenges of mid-infrared photodetection. Graphene has attracted great interest because of its exceptional electronic and optical properties, such as ultrahigh carrier mobility, broadband absorption, its cheap and nontoxic nature, and its compatibility with complementary metal-oxide semiconductors (CMOS). However, the 2.3% constant absorbance at visible and near-infrared wavelengths and even less at the mid-infrared wavelength is undisputedly insufficient for practical photodetection, even considering its one-atomic thickness. Additionally, pristine graphene is polarisation immune, which limits its application in many areas. Recently, several newly proposed plasmonic structures have been utilised to improve the performance of graphene photodetectors by enhancing the absorption of the graphene layer; however, these designed plasmonics structures do not possess the chirality property, which is key for circularly polarised light detection, although the efficiency of graphene photodetectors can be improved by up to 20 times. While some chiral plasmonic structures have been investigated for CPL detection, they suffer from low efficiency or non-directly detectable signals.

This chapter investigates a noble metal surface plasmons enhanced spin angular momentum graphene photodetector at mid-infrared to overcome these challenges. The graphene photodetector consists of a graphene layer and LH and RH chiral plasmonic structure array. There is an absorption difference for LH and RH under the illumination of LCP and RCP, which leads to CD. First, we optimise the structure parameter sizes; following that, the device is fabricated via the nano-fabrication method and characterised with our own system. Specifically, we aim to address the following questions:

1. To what extent can graphene absorption be enhanced by chiral surface plasmon resonances in the MIR?
2. Can the enhanced absorption in graphene layer be helpful for the increasement of photocarriers?
3. Can the internal electric field of graphene photodetector separate electrons in the mid-infrared?

The structure of this chapter is as follows. The development of geometry for the MIR spin angular momentum detector is introduced in Section 3.2, including why it is the best structure for detection. Numerical simulation and optimisation for each parameter is presented in Section 3.3. Having established design and simulation, we present the fabrication processes of these designed structures in Section 3.4. These chiral structures are characterised with SEM to verify that they are consistent with our design size and FTIR measurement is used to characterise the transmission signal to compare with the simulation results in Section 3.5. Section 3.6 concludes with a discussion of the results.

3.2 Detector geometry

When light is illuminated on a material and interacts with it, the shape and exact size of the geometry determines the resonant wavelength and strength. It has been shown that zigzag noble metal structures can be used for absorbing circularly polarised state of light[110]. Here, we use the zigzag structure to absorb the light in mid-infrared. We use silicon as a substrate due to the strong transmission between the wavelength of 1.1 μm and 6.5 μm. Furthermore, considering the properties of broadband absorption and high mobility of graphene, we choose graphene located on top of the substrate of SiO_2/Si as the absorption layer. The geometry of the chiral metal structure (see Figure 3.1 (a)) determines the CD between the LCP light and RCP light.

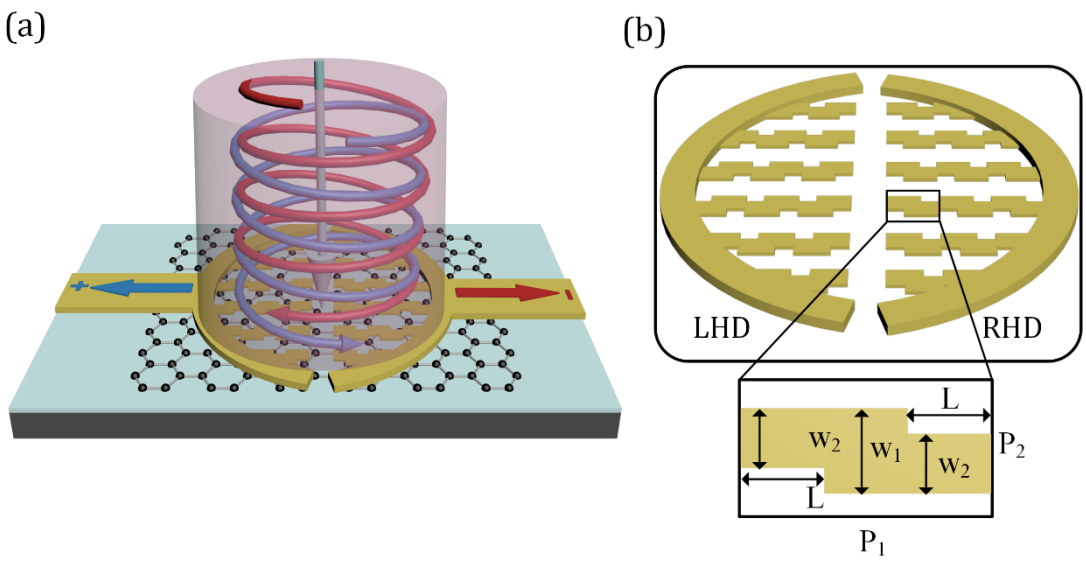

Figure 3.1 (a) Schematic of the simultaneous MIR spin angular momentum photodetector. The blue and red spiral represent LCP and RCP light and the positive and negative sign represent the defined photocurrent direction. (b) Schematic of chiral structure arrays. P_1 and P_2 are the period length, W_1 and W_2 are width and neck width of unit cell, and L is neck length of unit cell.

The operation principle is explained as follows. The source and drain electrodes of a monolayer graphene photodetector are shaped into left handed (LHD) and right handed (RHD) chiral zig-zag plasmonic resonators, respectively (see Figure 3.1 (b)). Each resonator is designed to be resonant with a single photon spin angular momentum state, illustrated in

the figure as either LCP or RCP spirals, respectively. Because of the chemical potential difference between each electrode and the graphene layer, two equal but opposite internal electric fields are formed at the two electrode boundaries. These electric fields peak within $\approx$ 300 nm from each electrode[149] such that adjacent electric fields do not considerably overlap and cancel. A single spin angular momentum state incident across the entire detector resonates with only one electrode and generates current in only one direction. This spin angular momentum dependent current generation is illustrated by the red and blue current directions in the Figure 3.1 (a).

3.3 Absorption optimisation

Responsivity is one of the most important parameters for photodetectors, and light absorption is the main contributor to the generation of photocurrent. Therefore, obtaining the maximum absorption and CD via structure optimisation is very important. Further, to gain a physical understanding of the optical and electrical properties of the chiral structure for photodetection, we first conduct a theoretical analysis and numerical simulation. Hence, in this section, we present and discuss the simulation results of the transmission and reflection of incident left circular polarised light and right circular polarised light on the chiral-graphene structure. The commercially available CST Microwave Studio, which is based on the frequency domain finite element method (FEM), is used for the simulation.

For all simulations, the unit cell boundary condition is applied in the X and Y directions. While open boundaries were chosen in the Z direction for incident plane waves to illuminate and exit the simulated system and extract the reflection, transmission and absorption information when the structure is excited with the LCP and RCP plane waves, with the high loss of higher order modes, here we only consider the fundamental Floquet modes at the open boundaries.

We use three main parameters to characterise the optical and electronic properties of the device:

Transmission: this parameter indicates how much of the RCP/LCP plane wave is able to transmit through the hybrid structure consisting of a chiral plasmonic structure, a graphene layer and SiO_2/Si substrate.

Absorption of hybrid structure (A_t): this is the amount of incident LCP/RCP light that is absorbed by the whole photodetector, calculated by subtracting the transmission and reflection from the incidence.

Absorption of graphene (A_g): this parameter shows how much incident LCP/RCP light can be absorbed by the graphene layer. Because graphene is the absorption layer and the medium that produces the photocurrent, the amount of graphene absorption influences the amount of produced photocurrent and the absorption difference between LCP and RCP determines the CD of the device. The absorption of graphene layer was calculated by getting the ratio between power loss in graphene layer and power stimulated in the incident port.

Since most infrared light is blocked by our atmosphere, the wavelength at the atmosphere transmission window is very important for astronomical communication or the science of geography, due to the reason that it can pass through the atmosphere without too much loss. Because of this, we shift the working wavelength of the designed structure to the first atmosphere window (3–5 μm) by choosing the appropriate size.

In the following subsections, we investigate the effect of geometrical parameters, such as P_1, P_2, W_1, W_2 and L, on the optical properties of chiral plasmonic structures. With these investigations, we aim to understand the behavior of the absorption of the hybrid structure and graphene layer and confirm the best geometry size for absorption and CD. In this way, appropriate experimental recipes and conditions can be targeted and planned.

3.3.1 The effect of unit cell size

Because changing the handedness of the chiral structure changes the chirality of the behaviour, we take the left-handed chiral structure as an example to calculate response to left circular polarised light and right circular polarised light. The absorption of photodetection structure and graphene layer for the left circular polarised light and right circular polarised light as the periodic parameter P1 is varied are shown in Figure 3.2. We investigate the fundamental mode of each size and plot the spectra from 3 μm to 5 μm.

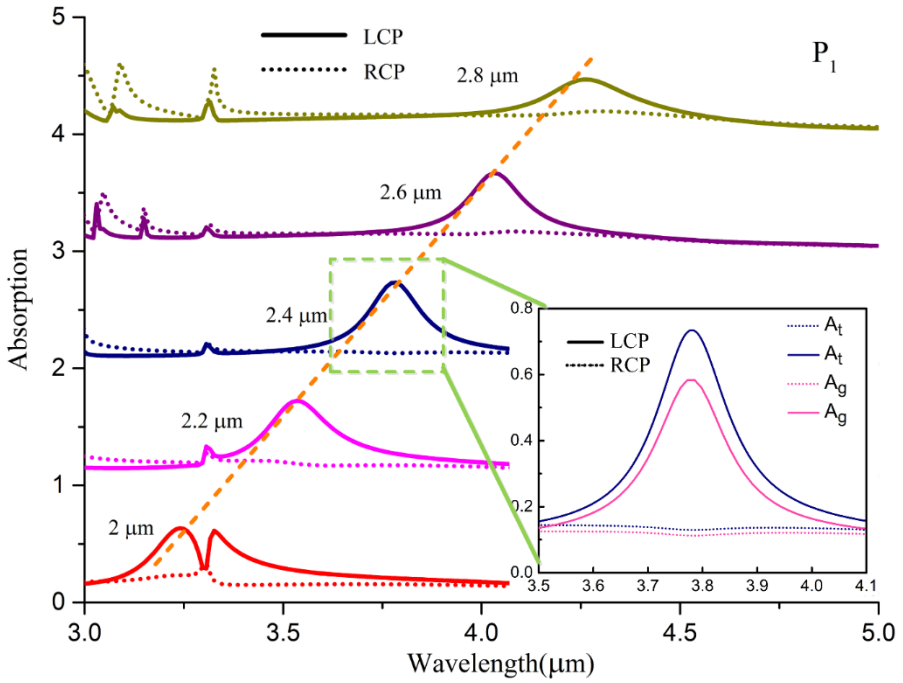

Figure 3.2 Numerical simulation of total absorption spectra for a LH chiral structure array with varying periodic length P_1. The inset shows the absorption of hybrid structure and graphene layer both for LCP and RCP when P_1 is 2.4 μm.

Two trends that indicate the optical properties of the simulated structure are clearly shown in these spectra. With lateral length increasing, the resonance wavelength shifts to red, and maximum absorption and largest CD occur when P1 is at the threshold of 2.4 μm. Further, the resonance peaks become lower and broader as P1 continues increasing from the threshold value. This is consistent with the Maxwell equations, which reveal that increasing structure size will redshift the resonance wavelength, and beyond a certain threshold, will lower and broaden the resonance. Further, the behaviour of graphene absorption is consistent with the behaviour of the hybrid structure. The main absorption of the hybrid structure comes from the graphene layer (85.7% at the threshold value of P1), which endorses our proposal that we can use the photocurrent produced from the graphene layer to detect the circular polarised state of the incident light.

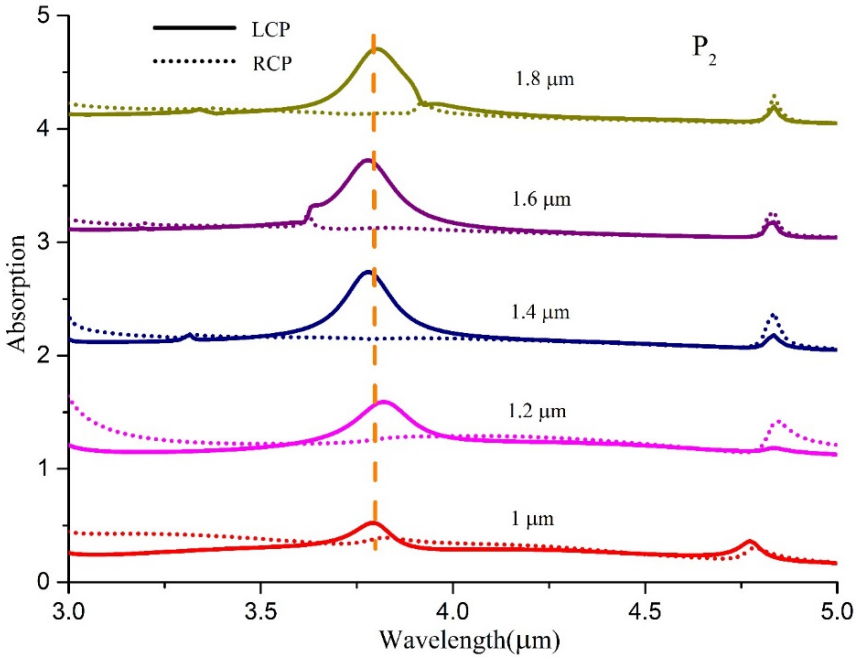

Figure 3.3 Numerical simulation of total absorption spectra for a LH chiral structure array with varying periodic length P_2.

The absorption spectra of the photodetection structure which includes LH chiral structure array and graphene layer as a function of P_2 is plotted in Figure 3.3. As there is no change in structure size, there is no clear shift in resonance wavelength. However, there is a considerable change of magnitude of the absorption when P_2 is varied. This is because the distance between each unit cell changes when P_2 varies, and this distance has an impact on the coupling between the unit cells, causing the absorption difference. Similarly, the behaviour of the graphene absorption is consistent with the behaviour of absorption for the whole hybrid structure.

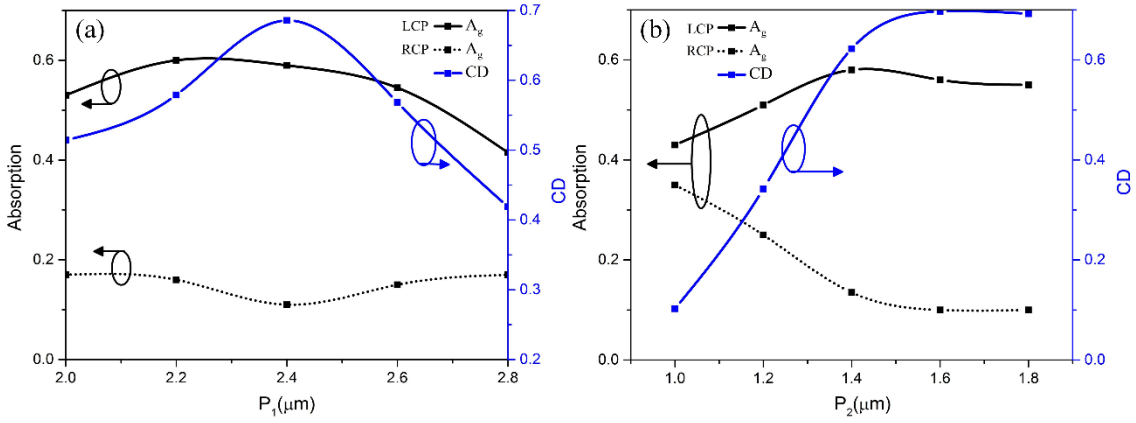

Figure 3.4 Simulated maximum graphene absorption for LCP and RCP illumination and CD for varying P_1 (a) and P_2 (b) respectively.

To clearly show the impact of P_1 and P_2 on the absorption of graphene layer and CD, we extract the related data from the above two figures and plot this in Figure 3.4. CD is defined as follows:

$$CD = \frac{A_L - A_R}{A_L + A_R} \tag{3.1}$$

By considering both a higher absorption and larger CD, we confirmed the optimised parameters of P_1 = 2.4 μm and P_2 = 1.4 μm.

3.3.2 The effect of width and neck width

With a similar methodology, we investigate the impact of width W_1 and neck width W_2 on absorption and CD under LCP and RCP illumination (see Figure 3.5).

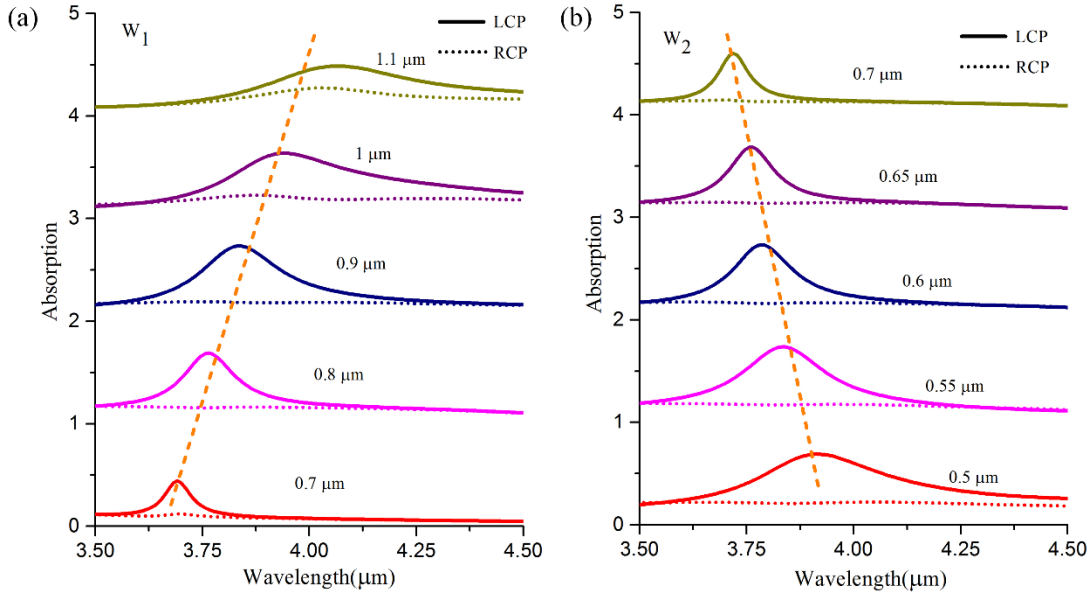

Figure 3.5 (a) Simulated total absorption spectra of photodetection structure with LH chiral structure and graphene layer under illumination of LCP and RCP for varying W_1. (b) Simulated total absorption spectra of photodetection structure with LH chiral structure and graphene layer under illumination of LCP and RCP for varying W_2.

As shown in Figure 3.5 (a) and (b), when increasing the size of the unit cell or decreasing the neck width of the unit cell, the resonance wavelength redshifts and the resonance peak starts to decrease and broaden after reaching a maximum value. In addition, the absorption of

graphene behaves similarly, with the absorption of the hybrid structure for both left circular polarised light and right circular polarised light.

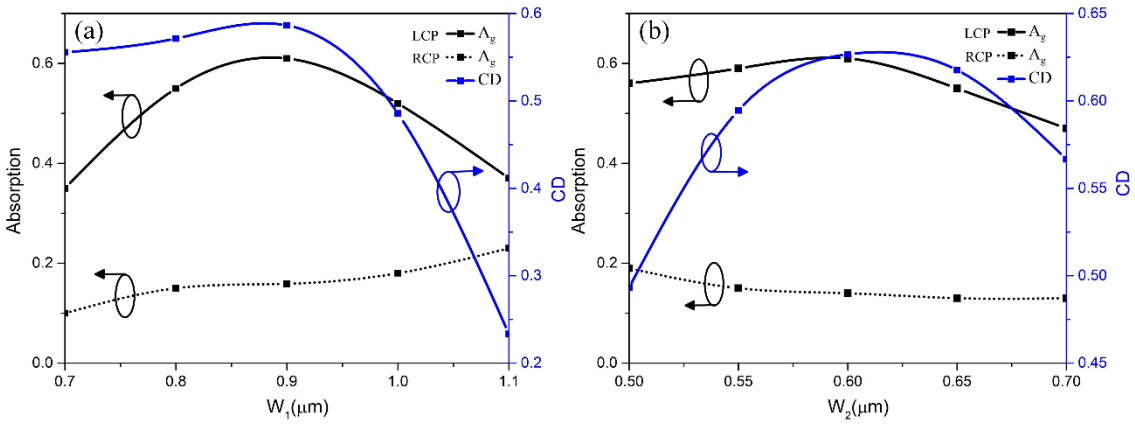

Figure 3.6 Simulated maximum graphene absorption for LCP and RCP illumination and CD for varying width (a) and neck width (b) of unit cell.

Similarly, by extracting related data and replotting in Figure 3.6, it is evident that the optimised values of the width and neck width are 0.85 μm and 0.55 μm respectively.

3.3.3 The effect of neck length

After four parameters have been optimised, the last size-related parameter that needs to be optimised is the length of the neck, L. Hence, in this subsection, we will investigate the impact of L on the optical properties of the proposed structure.

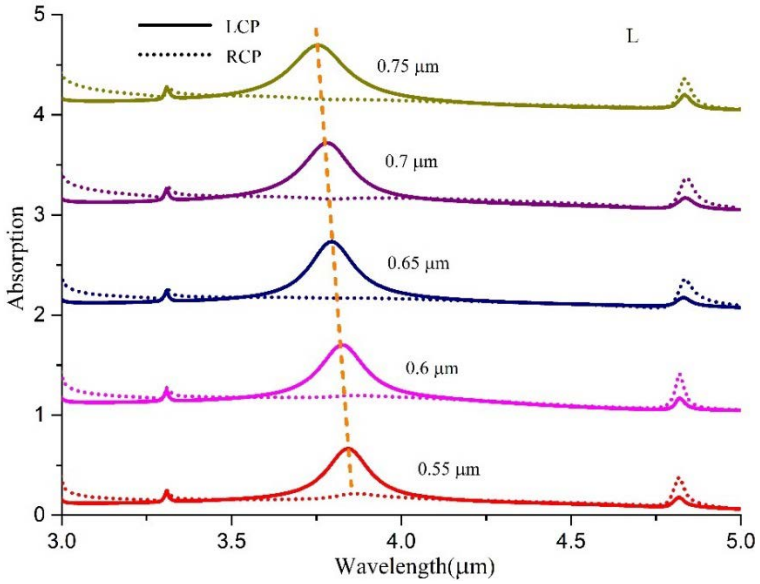

Figure 3.7 Numerical simulation of the LH chiral plasmonic structure for varying neck length L. (a) Total absorption spectra of hybrid structure for LCP and RCP. (b) Total absorption spectra of graphene layer for LCP and RCP.

As can be seen from the above figure, parameter L has a minor impact on the absorption of graphene and the hybrid structure compared with the previous parameters. The relationship between absorption of graphene, CD and parameter is plotted in Figure 3.8 which shows the optimised value of L is 0.6 μm. With this optimised parameter, the maximum absorption is 62% and the CD is 0.52.

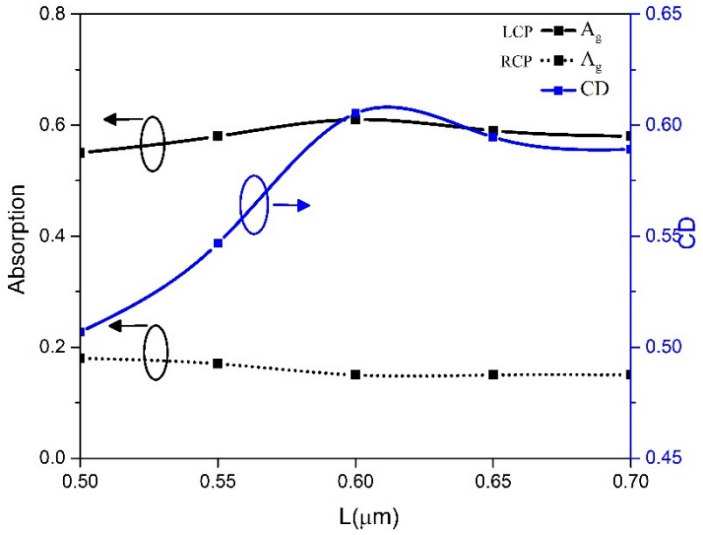

Figure 3.8 Simulated dependence of the maximum absorption of graphene layer for LCP and RCP and CD on the neck length of a unit cell.

3.3.4 The optical absorption and electric field

To fully understand the optical property and ability to generate photocurrent for the optimised structure, absorption of graphene and hybrid structure for the left-handed and right-handed structure with all optimised parameters (P_1 = 2400 nm, P_2 =1400 nm, W_1 =850 nm, W_2 =550 nm, L=650 nm) are shown in Figure 3.9 (a) and (b).

The maximum absorption of the whole hybrid structure and graphene layer can reach 78% and 59% respectively for LH with LCP illumination and RH with RCP illumination at resonant wavelength (see Figure 3.9). CD can be up to 45% by comparing the different absorption of graphene layer for LCP and RCP. Considering the atomic thickness graphene layer and the absorption of pure graphene layer is 2.3% for pristine graphene and drops with an increase of Fermi level, the absorption of graphene has been improved 26 times.

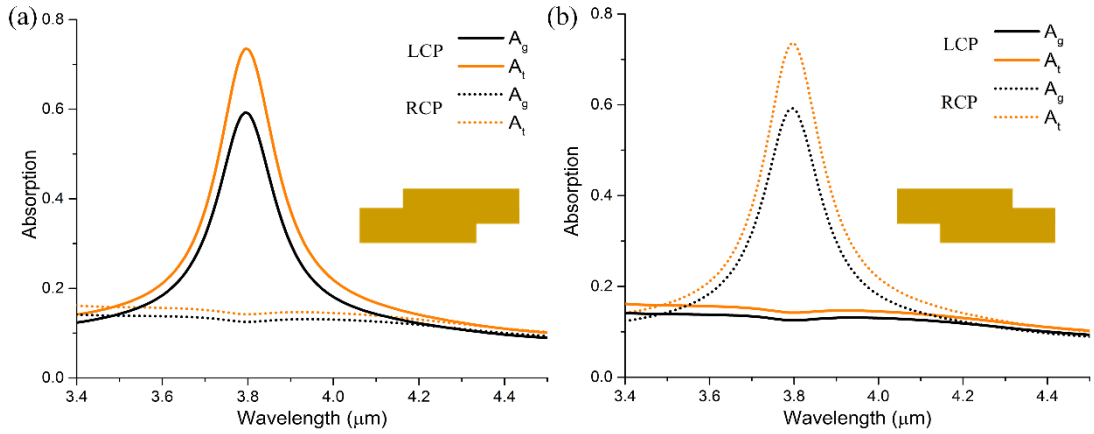

Figure 3.9 Simulated optical absorption spectra for optimised photodetector structure (P_1 = 2400 nm, P_2 =1400 nm, W_1 =850 nm, W_2 =550 nm, L=650 nm) under LCP and RCP illumination for LH (a) and RH (b) chiral plasmonic structure.

So far, we have investigated and simulated the optical property of the proposed hybrid structure, but not illustrated the relationship between optical absorption and generated photocurrent. Hence, this mechanism is demonstrated in this section.

Four different plots for electric energy density of two handedness chiral structures under illumination of both LCP and RCP are shown in Figure 3.10. From these plots, it is evident

that, for the LH structure, this resonates strongly with LCP illumination, while the resonance is much weaker under the illumination of RCP. The strong near-field enhancement can be seen along the edges of the electrodes and is particularly strong at the zigzag corners. The strength of the enhancement is most significant when on-resonance for LCP illumination, rising to four orders of magnitude higher energy density than the incident plane wave illumination. Importantly, this near-field electric field enhancement decays to −15 dB at a distance of 275 nm from the electrode, which overlaps with the internal electric fields in the graphene layer generated by the chemical potential difference between the graphene and gold. Electron–hole pairs generated by this near-field enhancement can therefore be separated by the internal electric field and can form a photocurrent. While the most efficient charge carrier separation occurs close to the 5 μm gap between electrodes where the probability of recombination is smallest, photocurrent contributions also arise along the length of the electrodes and contribute to total photocurrent magnitude.

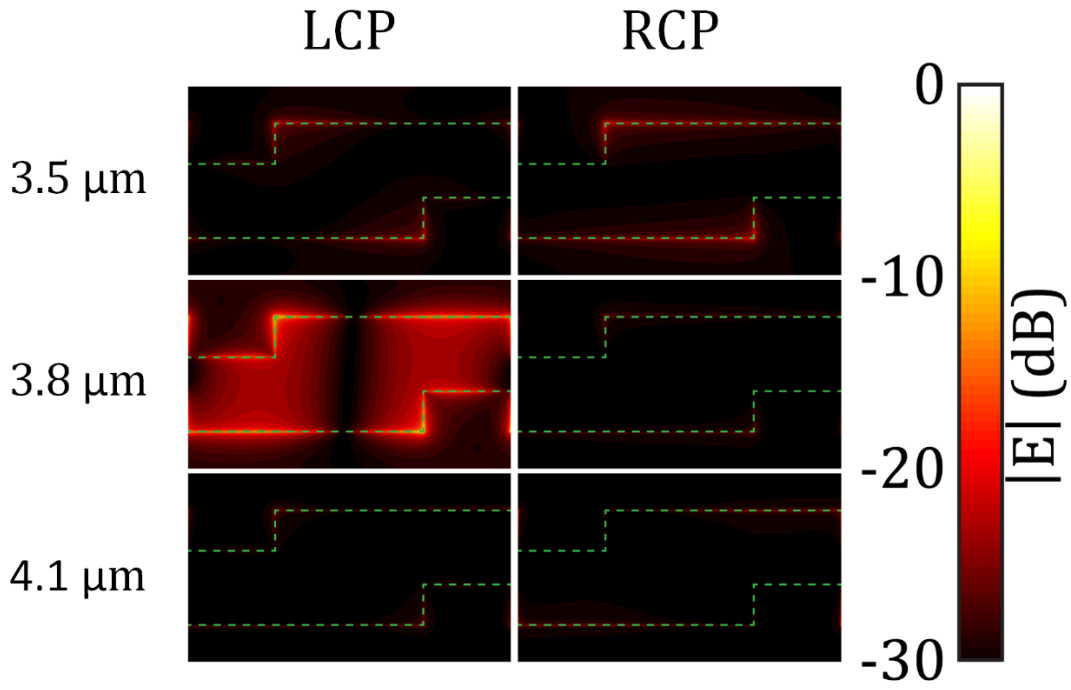

Figure 3.10 Simulated electric field for LH chiral plasmonic structure with LCP and RCP illumination at three different wavelengths.

In this section, we optimised all size-related parameters and investigated the relationship between strong near electric field and internal electric field to prove this proposed structure

can generate the photocurrent. In the following sections, we focus on the experimental part of this project.

3.4 Device Fabrication

In this section, we show the steps used to fabricate chiral graphene mid-infrared photodetectors. Our fabrication method involves two parts: materials preparation and fabrication. We introduce and explain why and how we use the nano-fabrication method to fabricate the device. Fabrication results are presented and followed by related discussion.

3.4.1 Materials and geometry

Large (several μm^2) graphene flakes can be produced in three main ways: mechanical exfoliation from graphite crystals[150, 151], which gives the highest quality of graphene flake, CVD graphene[152, 153] transfer, which shows the capability of producing larger controllable graphene layers, and epitaxial growth on silicon carbide (SiC) substrate[154, 155], which requires strict experimental conditions and high cost. Considering our experimental conditions and the required graphene area (up to at least 80 µm by 80 µm), we employed the CVD graphene and adopted the wet transfer method to achieve graphene deposition on the SiO_2/Si substrate.

The steps employed to transfer the CVD graphene are shown in Figure 3.11. The monolayer graphene sample sandwiched between two polymer layers was bought from Graphenea. While diluting in the water solution, the sacrificial layer/graphene was detached from the support film to float on the surface of the water. To transfer it onto the desired area of the substrate, the substrate was introduced into the water to retrieve the sacrificial layer/graphene from below. The sacrificial layer/graphene/substrate was dried for 30 minutes in the air and the samples annealed in a furnace at 450℃ for two hours with inert atmosphere. Before removal of the sacrificial layer, the samples were stored for at least 24 hours under vacuum conditions to avoid detachment of the graphene. Finally, the samples of sacrificial layer/graphene/substrate were dipped in acetone for one hour, followed by IPA rinse and nitrogen dry.

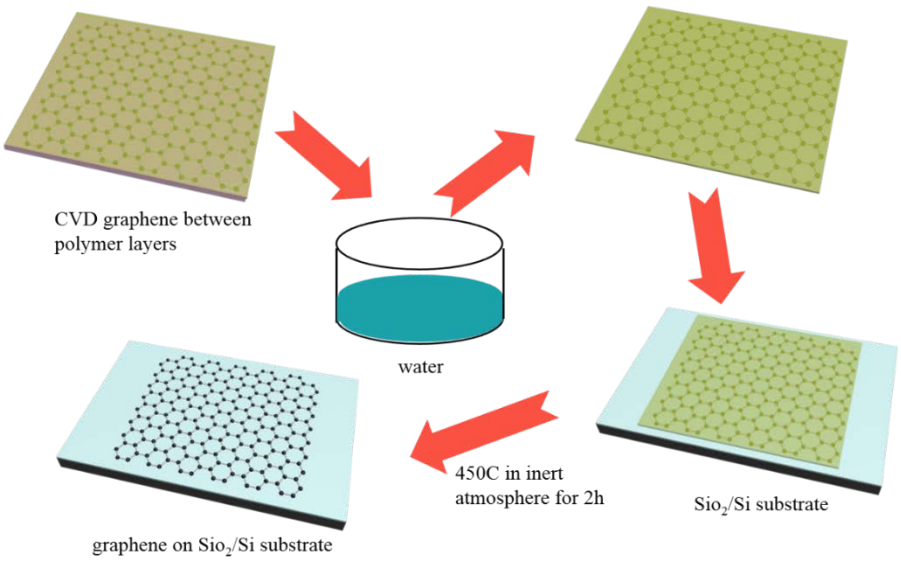

Figure 3.11 Schematic of the steps for the transfer of CVD graphene.

Once the graphene layer was transferred on the substrate, large electrodes were required to connect the macroscopical circuit and circulate the current signal. Here, we employed the photolithography technique (see Figure 3.12) to pattern these electrode areas because of its fast exposure speed (just a few seconds) and acceptable resolution (minimum feature size of a few micrometres). The photolithography (AZ 5214E) was performed with a SUSS mask aligner 6 machine. The procedure started with photoresist coating on the graphene-transferred substrate, after which the sample was exposed with proper dose after baking at 180 ℃ for 120 seconds. After development, the photoresist (AZ 5214E) was present everywhere except in the areas where the electrodes were to be deposited. The e-beam evaporation was done with the Lesker PVD 75 E-beam evaporator system, followed by the lift-off process to obtain regular electrode pads.

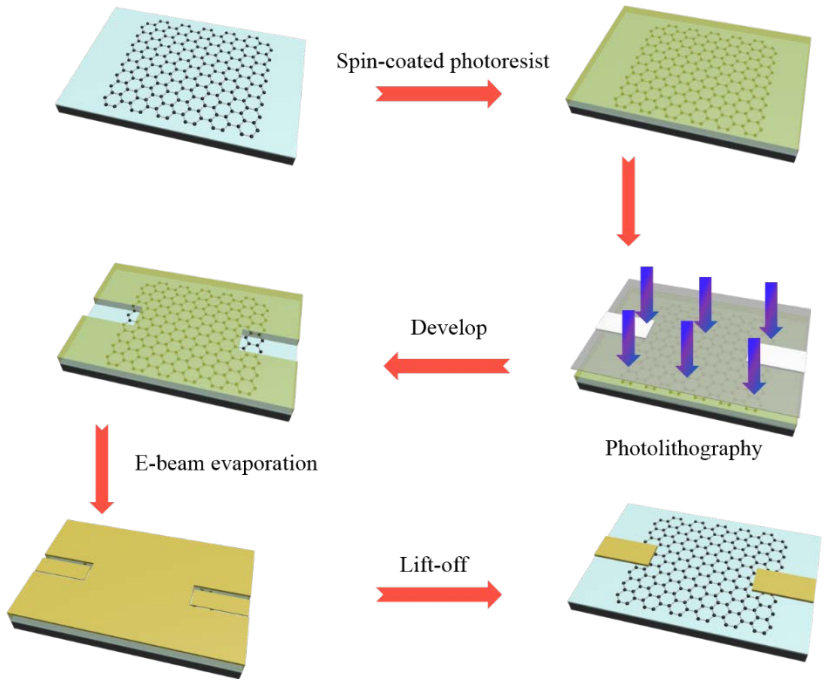

Figure 3.12 Schematic of the steps of photolithography process.

3.4.2 Chiral structure fabrication

Because the optimised size of the chiral plasmonic structure is at the scale of 1 μm, to obtain an accurate fabrication, a dedicated machine, Vistec EBPG5000plusES was used to fabricate the chiral structure. The process is similar to the photolithograph except its exposure source is electrons not UV light.

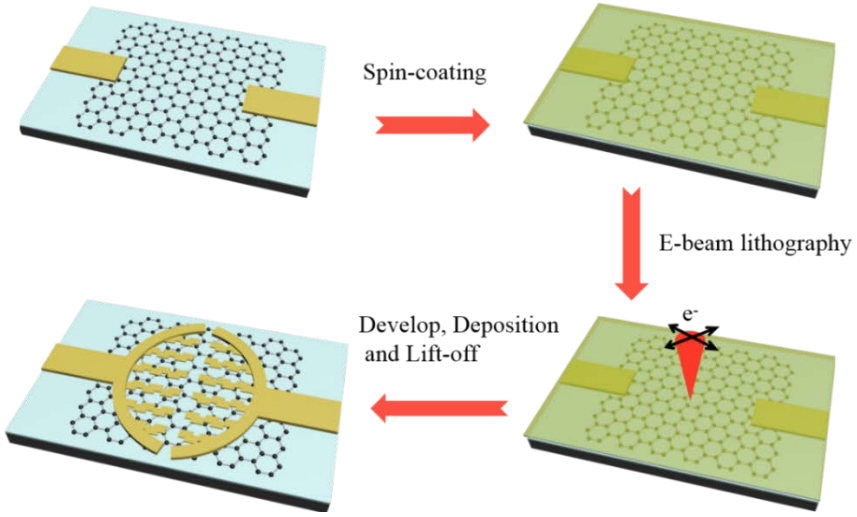

Figure 3.13 Schematic of the steps of EBL procedures.

After fabrication with EBL, the chiral structure array was characterised with SEM. The optical microscope image clearly showed the fine connection between chiral plasmonic structure and electrode and the gap between LH array and RH array. To quantitatively characterise the actual size and shape of the LH and RH chiral array, the SEM was used to measure size and depict the real shape to compare with the design.

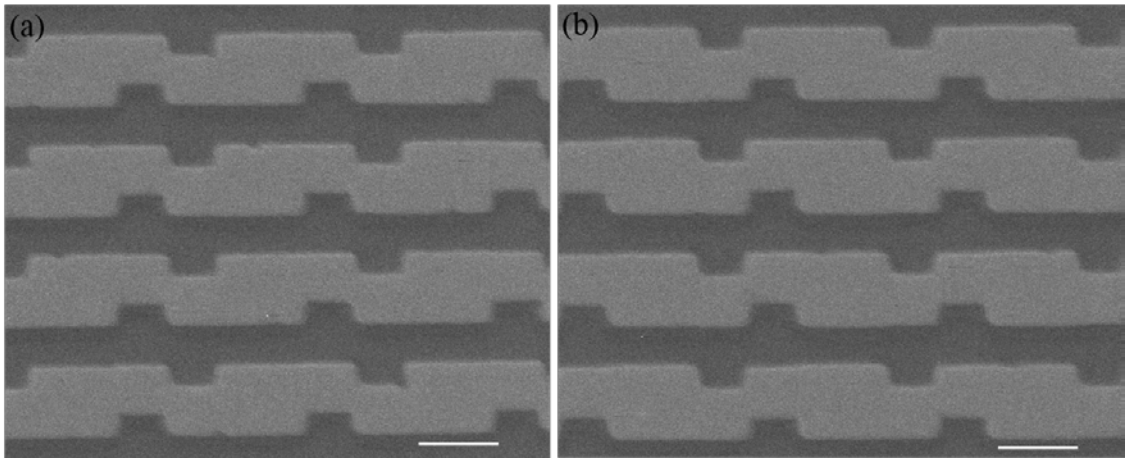

Figure 3.14 SEM image of the LH (a) and RH (b) chiral structure array. Scale bar is 1 μm.

Figure 3.14 shows SEM images of the LH and RH chiral plasmonic structure array. It clearly shows that the shape of the fabricated structures is consistent with the designed shapes, with distinct and sharp edges. With sufficient measurements of the actual size of the LH and RH chiral structures and comparing with the optimised parameters, we conclude that there is only 3.1% difference between the real sizes and their theoretical counterparts. Therefore, our developed nano-fabrication recipe is suitable for our experiment.

3.5 Optical and electronic characterisation

To confirm that photocurrent can be generated by the detector, we optically and electronically characterise the fabricated structures to confirm their optical properties. This was conducted with the measurement of the FTIR transmission spectra and photocurrent measurement of this photodetector under illumination of different circularly polarised light. In the following subsections, we focus on the optical and electrical characterisation of the device.

3.5.1 Characterisation system

The optical property of the chiral plasmonic structure was measured via FTIR microscopy (Perkin-Elmer Spectrum 100), which allowed us to characterise the transmission signal of the light over a broad range of wavelength (1–15 μm). This was also used to characterise the graphene plasmons or graphene-related surface plasmons work[110, 156-158]. The FTIR microscope operates by measuring the transmission signal when a broadband light source is focused on the micro-scale sample area. All measured transmission signals were normalised on the transmission through a sample substrate of the same size as the interested area (see Figure 3.15).

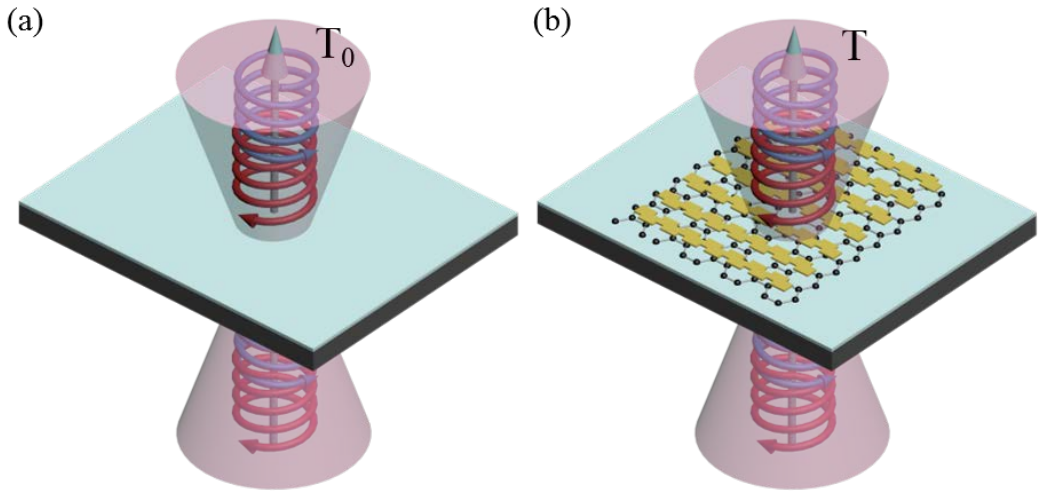

Figure 3.15 (a) Schematic of the measurement for transmission spectra of bare substrate. (b) Schematic of the measurement for transmission spectra of device. Blue and red spirals represent LCP and RCP light respectively. Yellow pattern represents LH or RH chiral structures.

The schematic of our home-made photocurrent characterisation system and the photodetector principle are shown in figure 3.16. A schematic of the optical and electronic characterisation system is shown in Figure 3.16 (b). MIR light is generated by difference frequency generation (DFG) from the output of an optical parametric amplifier (Light Conversion Topas + DFG1) pumped by a Coherent Astrella amplified Ti-Sapphire laser. A broadband linear polarizer (Thorlabs WP25H-B) and broadband quarter wave plate (Bernhard Halle BHN 2016.0083.0001) were used to generate LCP and RCP light corresponding to $+\hbar$ and $-\hbar$ spin angular momentum states.

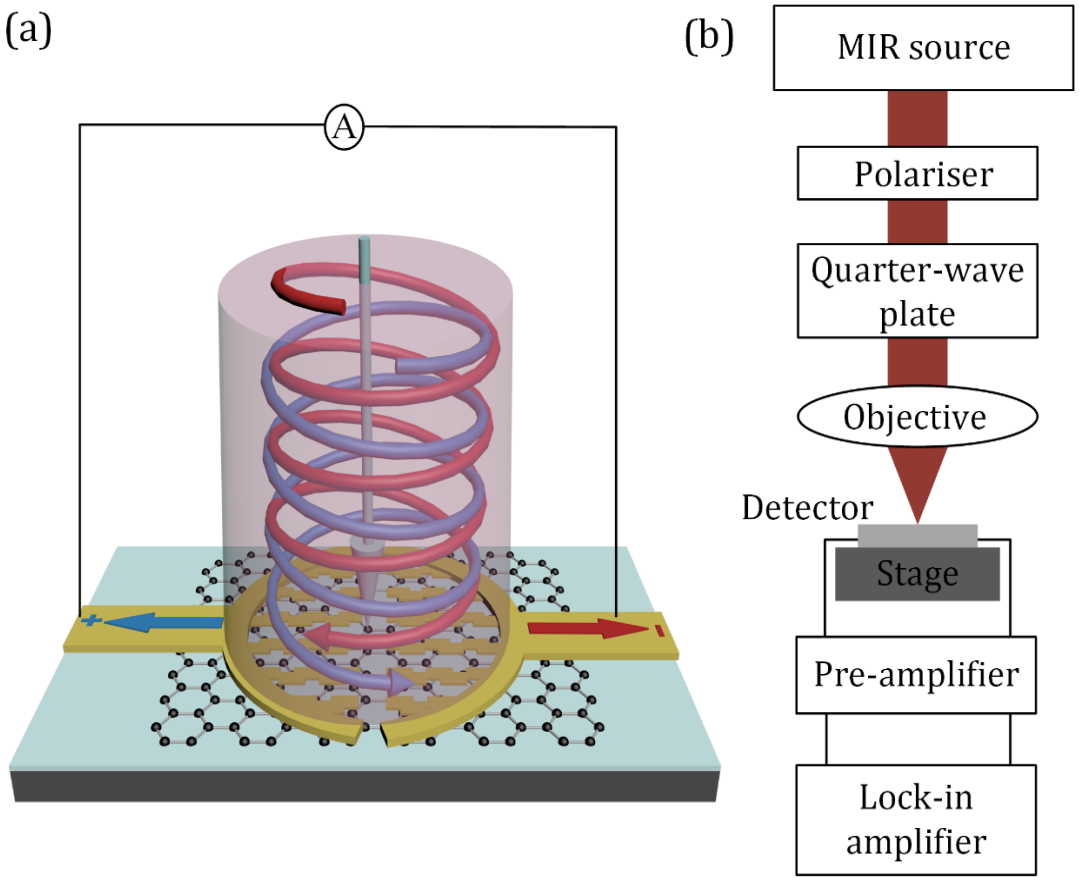

Figure 3.16 (a) Photodetector principle: LCP (blue) and RCP (red) illumination excite separate resonances in LH and RH electrodes that circulate current in positive (blue) and negative (red) directions, respectively. (b) Photocurrent measurement system: a MIR source is polarised by a linear polarizer and converted to LCP/RCP via a quarter waveplate. The beam is compressed by a 75 mm focal length lens onto the detector. The detector output is amplified by a current preamplifier and measured by a lock-in amplifier.

A 75 mm CaF2 singlet lens was used to illuminate a variable size circular area of the detector. The beam diameter entering the lens was 10 mm such that the numerical aperture of the illumination was 0.07. The illumination area was adjusted by translating the detector along the optical axis and a broadband 50:50 beamsplitter (Thorlabs BSW521) was used to enable visible light imaging via a LED/CCD based reflection microscope. The photocurrent generated by the detector was amplified by a low noise current preamplifier and detected by a lock-in amplifier (Stanford Research Systems SR570/SR530) locked to the 5 kHz frequency of the pump laser.

3.5.2 Circular dichroism

One of the core parts of this work is the absorption difference for different circular polarised light which is the origin of producing CD. Thus, we measured the transmission spectra of LH chiral plasmonic structure array and calculated the extinction spectra ($1-T/T_0$, T and T_0 are the transmission spectra through the chiral-graphene hybrid structure area and bare substrate area), and then compared with the simulated results (see Figure 3.17). Because the incident light is a pure plane wave in the simulation while it is focused light in the experiment which contains many different planes of waves, our measured extinction spectra and CD spectra are broader than the simulated results. This is a similar broadening as shown in NIR work[145], however, we still see strong CD for the LCP and RCP cases. It is evident that extinction can reach as high as ~ 80% and the CD of 8% has been achieved in experiment as expected in the simulation.

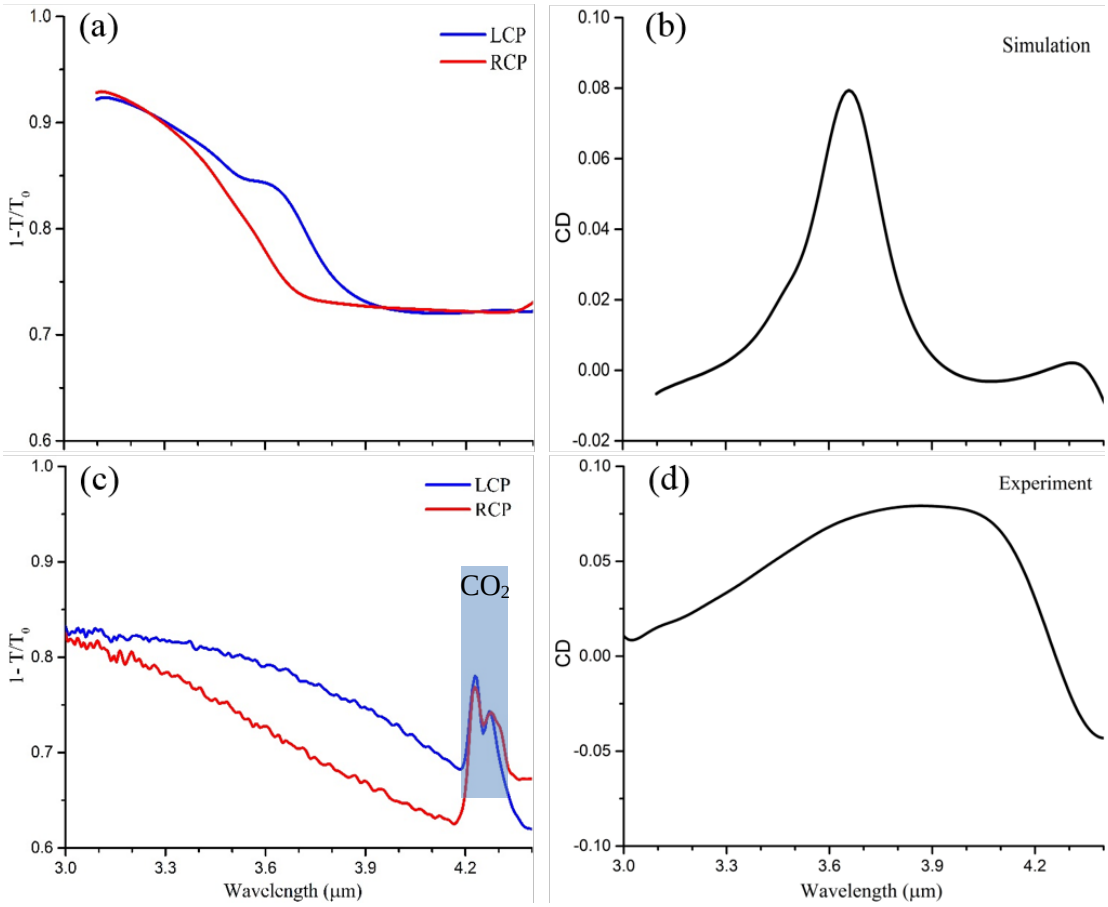

Figure 3.17 Simulated (top two) and experimentally measured (bottom two) extinction spectra (a), (c) and CD spectra (b), (d) of a LH chiral plasmonic structure with optimised size. Blue and red curves are for LCP and RCP transmitted light respectively.

3.5.3 Photocurrent characterisation

All the photocurrent characterisation was conducted with our home-made system (see Figure 3.16 (b)). The measured photoresponsivity spectra (see Figure 3.18) were obtained by measuring photocurrent as a function of wavelength when the device was illuminated with different circularly polarised laser light. The schematic of light illumination on the LH and RH structure array with different handedness of light are shown in Figure 3.18 (a) and (c), respectively, and the magnitudes of their corresponding photoresponsivity spectrum are shown in Figure 3.18 (b) and (d).

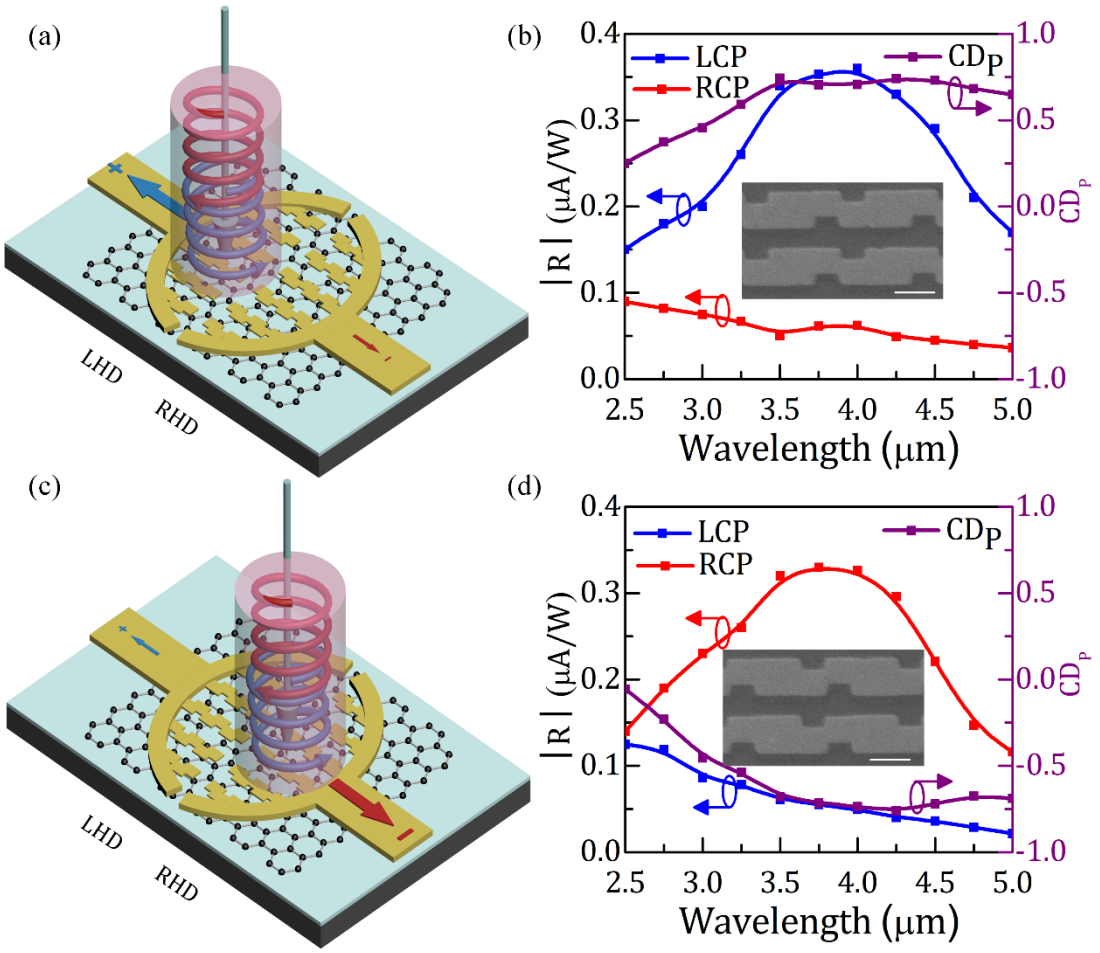

Figure 3.18 (a) LH surface plasmon electrode characterisation geometry. (b) Experimentally measured responsivity spectra and circular dichroism spectra of the LH surface plasmon electrode. Inset: SEM image of LH surface plasmon electrode. (c) RH surface plasmon electrode characterisation geometry. (d) Experimentally measured responsivity spectra and CD spectra of the RH surface plasmon electrode. Inset: SEM image of RH surface plasmon electrode. Scale bar is 1 μm.

The photocurrent CD shown in Figure 3.18 was defined as below:

$$CD_P = \frac{I_L - I_R}{I_L + I_R} \tag{3.2}$$

It is evident that there is some consistency between the measured photoresponsivity spectra (Figure 3.18 (b) and (d)) and the measured absorption spectra (Figure 3.17 (a) and (c)), proving that the photocurrent spectrum results from the absorption spectrum of the chiral structure. The maximum photoresponsivity at resonant state reaches ~0.38 μA/W, while its counterpart for the other circularly polarised light illumination is ~0.06 μA/W, which reveals that the polarisation discrimination ratio is 6.3 and the photoresponsivity difference is 0.32 μA/W. Our investigation provides one solution for the detection of MIR circular polarised light at room temperature.

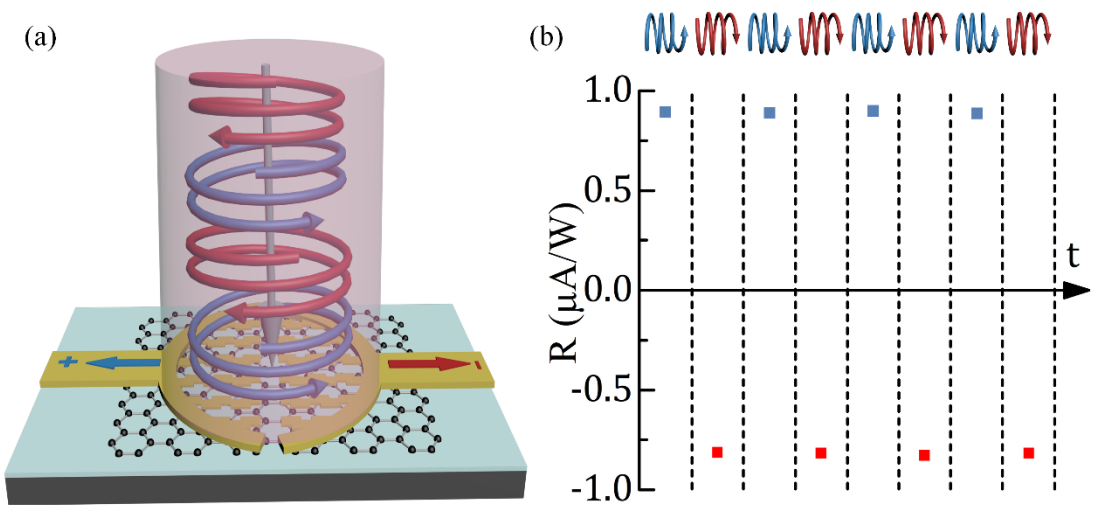

Figure 3.19 (a) Detector characterisation geometry. (b) Experimentally measured photocurrent from the entire photodetector area during illumination by a train of alternating LCP and RCP mid-infrared light.

The detection of different circular polarised light in MIR via photocurrent discussed above was obtained by illuminate light on different areas with LH and RH arrays. However, the core and innovative part of our demonstrated device distinguishes the circularly polarised states through the photocurrent flow direction without any illumination alignment on specific handedness structure arrays. Hence, we illuminated laser light with different circularly

polarised state on the whole area of the central chiral structure and measured the photocurrent as a function of time and polarisation states (see Figure 3.19).

The normal procedures were followed in conducting the experiment. First, with the help of visible light (660 nm), we aligned the system and ensured the focused spot illuminated the centre spot of the chiral structure array. Then, we calculated the focused MIR beam diameter based on the output laser spot and the parameters of the optics that laser light travels through the system and then moved the stage from the focus spot to guarantee that the whole chiral structure area was covered with MIR light. Two linear polarisers were used in this characterisation system. The function of first polariser was to provide a linear polarised light for the following optics and to reduce the MIR laser light to a safe power value. The second liner polariser was used to change the circular polarisation state. Moreover, the power of the incident light was recorded before the objective and all the photocurrent signal was measured with a preamplifier and lock-in amplifier.

As can be seen in Figure 3.19, a clear photocurrent distinction (positive and negative values) for LCP and RCP illumination at resonant wavelength (3.8 μm for our experimental structure) was observed. Because the fabricated LH and RH chiral structure array possessed the same size, a magnitude of the photocurrent of about 0.88 μA/W for both LCP light and RCP light was achieved. With the rough alignment of illumination light on the centre of the whole chiral structure array, there was a negligible difference between these. Another reason for the difference of photocurrent magnitude between the two polarisation states, or a single polarisation state at different times, is the variation of the laser output power.

From this subsection on photocurrent characterisation, it is evident that the LH and RH structure arrays possess different photoresponsivity spectra for LCP and RCP illumination, which is one basis for our photodetection design. Further, photocurrent with a different flow direction was achieved when the circular polarisation state of incident light was different. Moreover, as the chirality of our device originated from the structure of the chiral array, instead of a material chirality, multiple metal structures can be incorporated into this design to achieve multiple functionalities, such as different modes of orbital angular momentum detection or wavelength selectivity, within only one compact device. Hence, this simultaneous MIR spin angular momentum photodetector provides a solution for on-chip ultracompact photodetection of light properties.

3.6 Discussion

Here, we proposed and explored a novel hybrid structure that includes a graphene layer and chiral plasmonic structure array for simultaneous MIR spin angular momentum detection. In the first two sections of this chapter, we presented the introduction and the methodology for designing a practical structure for SAM detection. Then, commercially available FEM software, CST Studio, was utilised to numerically optimise all parameters of the proposed structure, based on higher graphene absorption and larger CD.

We then presented the direct detection of photon spin angular momentum in the mid-infrared by a single surface-plasmon-enhanced graphene photodetector. The detector was designed such that spin angular momentum states of opposite signs generate equal magnitude photocurrents of opposite sign, such that the states can be discerned electronically. The operating principle of our detector is detailed as follows. The source and drain electrodes of a monolayer graphene photodetector were shaped into left-handed and right-handed chiral zigzag plasmonic resonators, respectively. Each resonator was designed to be resonant with a single photon spin angular momentum state, illustrated in the figure as either LCP or RCP spirals, respectively. Because of the chemical potential difference between each electrode and the graphene layer, two equal but opposite internal electric fields were formed at the two electrode boundaries. These electric fields peaked within ≈ 300 nm of each electrode, such that adjacent electric fields did not considerably overlap and cancel. A single incident spin angular momentum state across the entire detector resonates with only one electrode and generates current in only one direction.

In summary, we designed and fabricated an integrated mid-infrared graphene photodetector that can directly detect the photon spin singular momentum states associated with incident LCP and RCP light. We used zigzag surface plasmon electrodes of opposite handedness to enhance graphene absorption by a factor of 17, to a maximum of 41% for LCP and minimum of 8.5% for RCP, corresponding to an absorption CD of 65.7%. We observed a peak responsivity of 0.80 μA/W and current CD of 66.7% at a resonant wavelength of 3.8 μm, corresponding to the first atmospheric transparency window, which is useful for emerging high bandwidth applications such as LiFi and LiDAR. Using this detector we showed that the photon spin angular momentum states associated with LCP and RCP light can been directly distinguished by the sign of the produced photocurrent. As the chirality and resonant wavelength of our photodetector resulted from the chirality and size of the surface plasmon electrodes and not the intrinsic properties of any of the materials, additional electrode geometries can be incorporated into a single device to expand the detection of other multiplexed states such as wavelength and orbital angular momentum.

Chapter 4

Principle of intrinsic graphene surface plasmons enhanced mid-infrared photodetection

4.1 Introduction

In the previous chapter, we investigated MIR spin angular momentum detection with a hybrid structure that contained a chiral plasmonic structure and a graphene layer. However, the metal surface plasmons utilised to enhance light absorption and photocurrent was parasitic; therefore, energy loss was unavoidable. In this and the following chapter, we investigate the properties of graphene plasmons and how to take advantage of graphene plasmons for photodetection. Based on this goal, we propose and investigate the MIR graphene photodetector enhanced by tunable intrinsic plasmons.

Before we start the experimental investigation of the MIR graphene photodetector based on a GNM structure, we conducted a theoretical and numerical investigation to guide the experiment. Thus, the aim of this chapter is to discuss the properties of graphene plasmons supported by a GNM structure. Specifically, we aim to address the following questions:

1. How do the geometrical parameters of the GNM structure affect the properties of graphene plasmons and the size of band gap?
2. Can a GNM restrict dark current by opening a band gap whilst simultaneously increasing absorption via localised surface plasmons?
3. To what degree can graphene photodetection be made spectrally selective and tunable?

This chapter is structured as follows. In Section 4.2, we investigate bandgap engineering for different geometric parameters. Because the nanomesh structure determines how many carbon atoms need to be removed and the fabrication pattern, it is important to investigate the relationship between the size and shape of the nanomesh structure and the magnitude of its bandgap to find the optimised geometric parameters. In Section 4.3, the properties of graphene plasmons are characterised. The two main factors of interest are resonant wavelength and resonant magnitude. Hence, the numerical simulation gives the resonant information for different parameters. Section 4.4 concerns predicted enhancement; we compare the absorption magnitude of the optimised structure and the pure graphene layer, to show the enhancement information. Section 4.5 offers a discussion and demonstrates the simulation results and how these results can help the experiment.

4.2 Band gap engineering

Efficient photodetection at room temperature requires the opening of a band-gap large enough to prevent excitation into the conduction band from thermal phonons. To determine the band gap level achievable by a GNM we investigate the band gap engineering of the GNM structure where the opened band gap caused by the quantum confinement effect. And the schematic of the electronic band structure of graphene and GNM have been shown in Figure 4.1. The function of the introduced band gap is to enhance responsivity by increasing the separation rate of the electron-hole pair and restrain the dark current normally caused by thermal fluctuation. Electrons jump from the valence band to conduction band when light is illuminated and there is less chance to recombine these due to the exist of the band gap in GNM structure. Furthermore, the electrons excited by thermal fluctuation cannot easily jump from the valence band to the conduction band if the energy of band gap is larger than the thermal fluctuation energy.

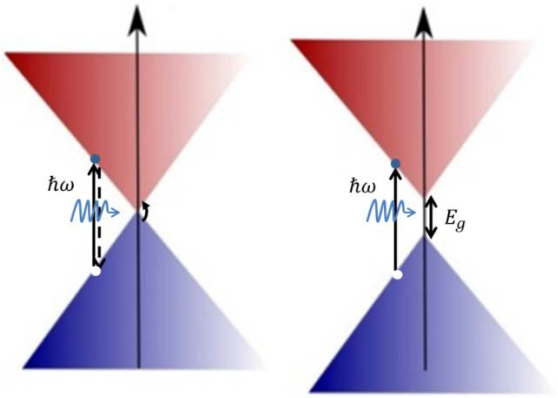

Figure 4.1 Schematic of the electronic band structure of graphene and GNM with opened band gap. The solid arrow denotes the excitation from valence band to conduction band with light incidence of frequency ω and the dash arrow denotes the recombination of electrons and holes.

4.2.1 Nanostructure design

The opening of a bandgap in graphene requires restricting electron motion via the creation of nano-scale neck widths. Many 1D and 2D geometries can create such quantum confinement. Here we investigate four nanomesh geometries that vary the neck width required for quantum confinement whilst also varying the level of remaining graphene available for absorption. Here, we theoretically investigate the band gap engineering in this section. Here, we discuss several designs of the GNM structures which is determined by the defect shape, such as, hexagon and circle, and the array arrangement type, such as square, hexagonal and triangular (see Fig. 4.2).

Density functional theory (DFT) which is adopted from references[31, 134] is used to calculate the band gap of GNM structure. For this theoretical calculation, the self-consistent pseudopotential calculation based on both the plane-wave and linear combination of atomic orbital basis is used, which exhibits the following relationship between the band gap and the ratio of diameter-period:

$$E_g = g\frac{N_{removed}^{1/2}}{N_{total}} \tag{4.1}$$

where, g=25 eV is a constant obtained by fitting numerical data, $N_{removed} and\ N_{total}$ are the numbers of removed and total (before removing C atoms to make meshes) C atoms in a unit cell, respectively.

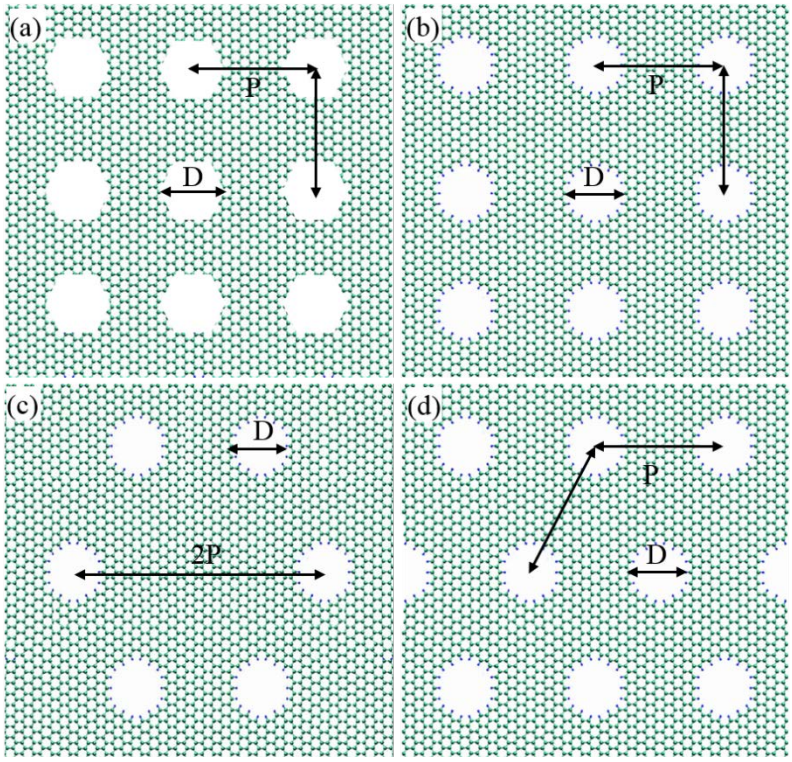

Figure 4.2 Schematic of the GNM structures with different defect shapes and arrangements. (a) Hexagon defect in square array. (b) Circle defect in square array. (c) Circle defect in hexagonal array. (d) Circle defect in triangular array. P (2P for figure c) denotes the period of the array, D denotes the diameter of the circle, length of the equilateral triangle and length of the hexagon respectively.

According to the above formula, it can be found that the remaining atoms restrict the freedom of electrons and force the electrons to travel within specific areas (neck width areas), which produces the bandgap of a GNM structure. The bandgap produced by the quantum confinement effect manifests itself by the remaining carbon atoms, by either fixing the period while changing the defect size or fixing the defect size while changing the period. Hence, we investigate the effect of parameter P and d (L for triangle and W for hexagon) on the bandgap. Because our theoretical investigation offers endorsement for the following experiment, the default value for the parameters is around the minimum value of our nano-fabrication resolution (about 50 nm). Thus, we obtain the best design based on the criteria of bandgap size and surface plasmons resonance strength.

4.2.2 The effect of period

In this section, we vary the period of the defect array to determine its effect on the magnitude of the bandgap when the size of defects is certain. As our nano-fabrication resolution is 50 nm, we set D as 50 nm and vary P from 50 nm to 100 nm. The calculated results for the bandgap with varied P are shown in Figure 4.3. As can been seen by these bandgap curves for different types of defect shapes and array arrangement, there is a reverse square relationship between bandgap and parameter P. This is consistent with expectations, because the band gap is reversely proportional to the total carbon atoms of one unit cell, while total carbon atoms is linearly related to the square of parameter P.

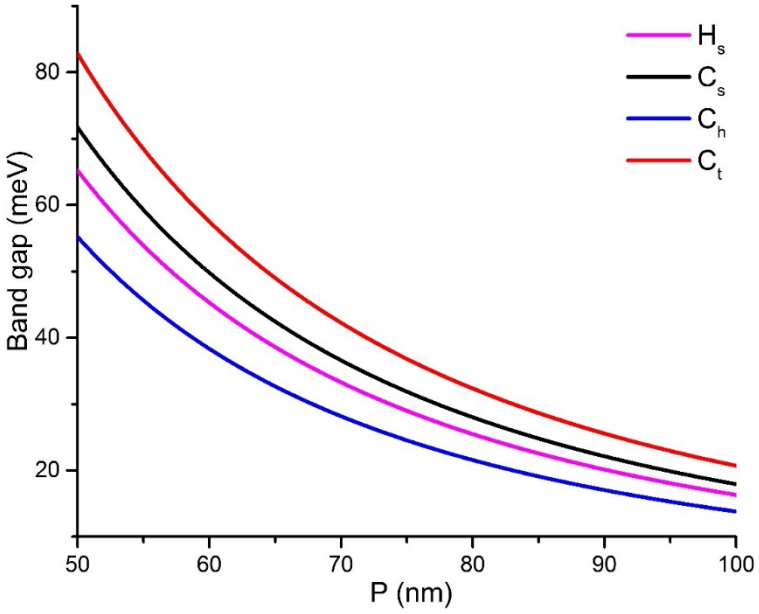

Figure 4.3 Calculated band gap of GNM against the period of defect array for different types of defects with D is 50 nm. H_s ,C_s, C_h and C_t denote the hexagon shape defect with square arrangement, circle shape defect with square, hexagonal and triangular arrangement respectively.

Further, for the same value of period, the triangle shape has the smallest bandgap when compared with the hexagon and circle. This is because there are more removed carbon atoms for the circle shape when P and W are same for all these shapes. Moreover, for same size and period parameters, the bandgap of the triangular arrangement is larger than the hexagonal arrangement, which can be proved from the circle case. This arises because the asymmetric arrangement is more compact compared with symmetric arrangements. Therefore, we can

conclude from this calculation that we need to choose the circle shape with asymmetric arrangement for the fabrication pattern of the GNM if we want to obtain a larger bandgap.

4.2.3 The effect of diameter

For a given period, the increment of diameter means a narrower neck width between neighbour holes. Neck width determines the remaining carbon atoms, which contributes to the introduced bandgap in the GNM structure. Therefore, we investigate the relationship between diameter and bandgap. Figure 4.4 shows a clear linear relationship between parameter D and bandgap, as the band gap is proportional to the square root of the number of removed carbon atoms while there is a quadratic relationship between parameter D and number of removed carbon atoms. Moreover, we reach the same conclusion that the circle shape with asymmetric arrangement has the largest bandgap when compared with other shapes of the same size and other arrangements.

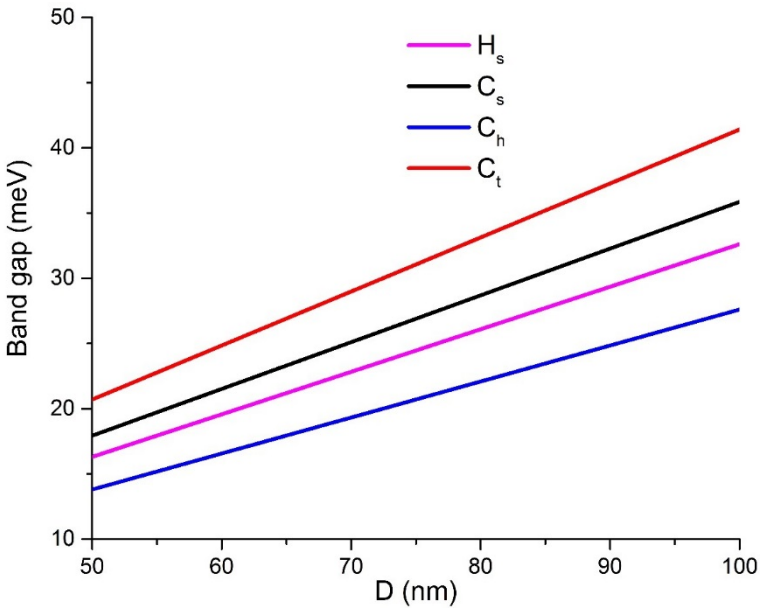

Figure 4.4 Calculated band gap of GNM against D for different types of defects with P is 100 nm.

In the previous two sections, we investigated the effect of parameters P and D on the magnitude of the band gap in GNM structures. Removing atoms produced a bandgap because it confines electron motion to a small neck width, inducing the quantum confinement effect—the narrower the neck width, the larger the bandgap.

4.3 Graphene local surface plasmon characteristics

The effect of defect shape and lattice type on the bandgap of a GNM structure were investigated in the previous section. Although a larger bandgap is preferred when choosing the shape and lattice type of a nanomesh structure, a further factor to consider is the graphene local surface plasmon characteristics supported by the mesh structure. This is because the strength of the responsivity of a GNM photodetector is limited to the absorption magnitude of the surface plasmon resonance. The function of the bandgap is to increase the electron–hole separation ratio by restraining its recombination to increase the photocurrent while surface plasmons enhance the light absorption. To obtain an excellent performance of the proposed graphene photodetector, we not only need to consider the bandgap of the GNM structure but also emphasise its absorption ability, which is a decisive factor of the photocurrent.

Therefore, in this section, surface plasmons characteristics are investigated and demonstrated. Results and discussion follow.

4.3.1 The period of GNM

Since the graphene layers can be doped strongly[159] and the experimentally achieved value of mobility μ is up to ~ 40,000 cm^2/Vs at room temperature 300 K [160], we rationally set the physical parameters of graphene as E_F=0.4 eV, τ= 8000 cm^2/Vs and T=300K. In addition, our fabrication resolution is around 50 nm. Smaller size can be achieved while at the cost of longer fabrication time which usually leads to beam distortion problems and higher costs.

The parameters mentioned above are utilised to explore the effect of period on absorption. The results are shown in Figure 4.5, where we can easily see that the resonant wavelength redshifts as the period increases when the diameter is fixed at 50 nm. Detection bandwidth is up to ~800 nm when the period ranges from 60 nm to 100 nm while all absorption magnitudes are larger than 3%. The maximum absorption is ~7% when the period is 70 nm and the resonant wavelength is 5.5 μm. At this resonant state, the magnitude of the electric field is shown in the inset of Figure 4.5. It is evident that the resonant mode is high order and that there is a strong coupling between the nearby holes. This strong coupling and interaction are the key factors for the high absorption magnitude compared with non-resonant states, and also explain why when the period increases from this value the related absorption decreases. The longer the

period, the less the coupling. Moreover, the reason why the absorption magnitude also decreases when the period decreases from 70 nm is that when the period is smaller than this threshold value, there is too little graphene area left (which acts as the absorption material), although there is stronger coupling between the holes at such short period.

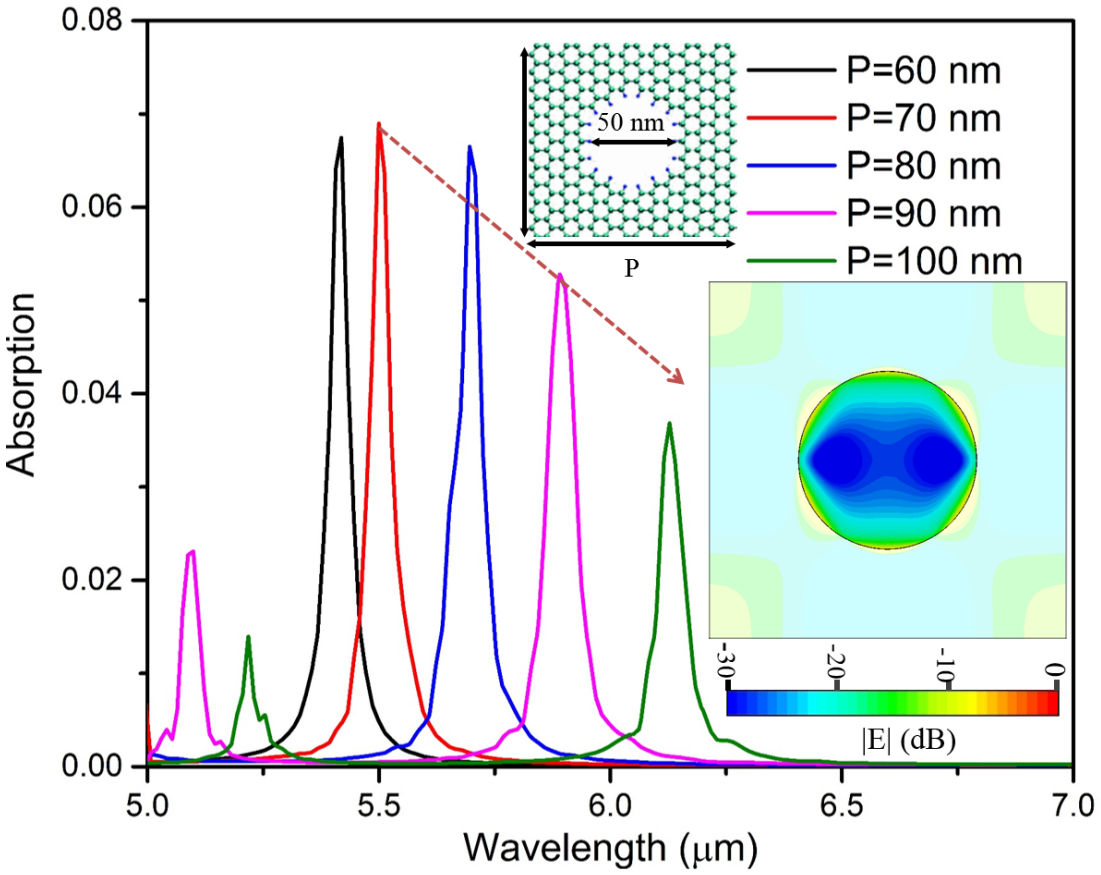

Figure 4.5 Absorption spectra of GNM with diameter of 50 nm and varying periods.

As shown in the figure above, the coupling between nearby holes and the remaining graphene layer determine the absorption magnitude. Further, a smaller unit cell with larger hole can produce a higher bandgap. From the point of view of characterisation and the performance of our proposed device, we prefer a smaller unit cell with a larger hole. However, limited by the fabrication resolution of the nano-fabrication system, we set the diameter of 50 nm and the period from 70 nm to 100 nm as the reference values of the fabrication experiment.

4.3.2 The diameter of GNM

Here, we investigate the effect of hole diameter on the magnitude of absorption and resonant wavelength. The length of unit cell is set as 100 nm and the diameter ranges from 40 nm to 80 nm with an increment of 10 nm. The simulation results are shown in Figure 4.6, from which it is evident that the shift range of the resonant wavelength is only ~ 300 nm and the resonant wavelength blueshifts as the diameter increases when it is below 50 nm, while it redshifts with an increase in diameter beyond 50 nm. This is because the resonant electrons along the edge of the circle begin to interact with their neighbours as the diameter increases.

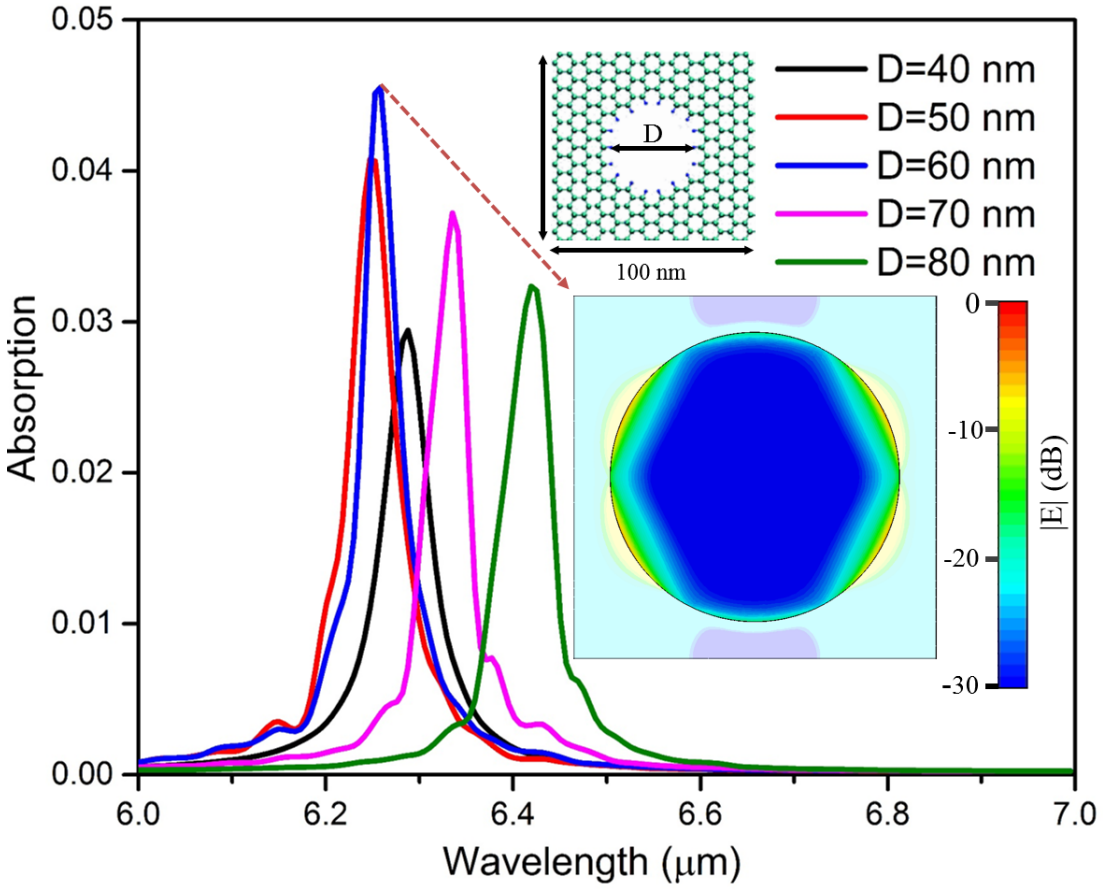

Figure 4.6 Absorption spectra of GNM with period of 50 nm and varying diameters.

Further, the maximum absorption is up to 4.5% when the diameter is 60 nm. Although this absolute value of absorption is still weak, it is an order of enhancement when compared with the absorption of the pure graphene layer at MIR with the same Fermi level. The electric field

distribution at resonant state is shown in the inset. It is evident that the resonant graphene plasmons is a quadrupole and there is strong coupling between nearby holes.

However, the resonant peaks do not show a regular shift as the diameter increase from 40 nm to 80 nm when the period is 100 nm. When the diameter is smaller than 60 nm, the resonant wavelength blueshifts and the magnitude of absorption increases as the diameter increases, while when the diameter is larger than 60 nm, the resonant wavelength redshifts and resonant wavelength decreases with an increase of diameter. This phenomenon represents a trade-off between fundamental plasmons resonant modes and high-order plasmons resonant modes and coupling between neighbouring holes.

4.3.3 The Fermi level of GNM

Besides the size tunability, another degree of freedom for tunability is the Fermi level of the GNM layer. In this section, we investigate the effect of the Fermi level on the absorption magnitude and the photodetection bandwidth (see Fig. 4.7).

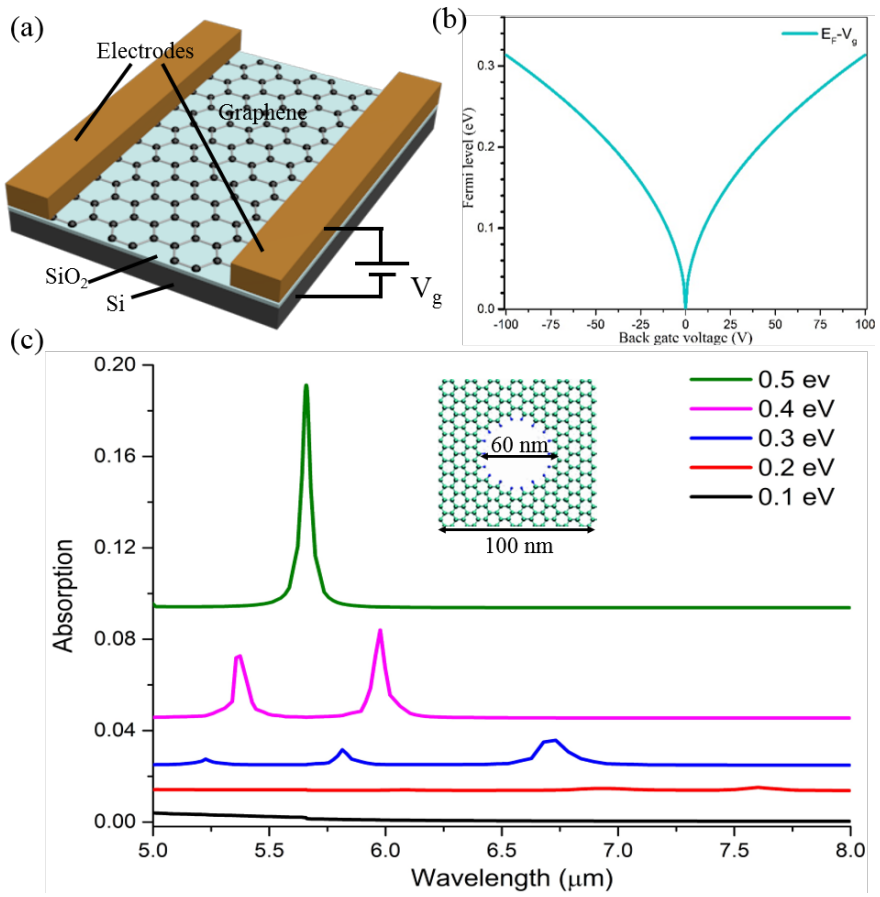

Figure 4.7 (a) Schematic of back-gating for GNM photodetector. (b) Calculated Fermi level against applied back-gate voltage. (c) Numerically simulated absorption spectra of a GNM structure with unit cell size 100 nm and diameter 50 nm for different Fermi levels.

Considering our fabrication ability and the simulated results on the effect of nanomesh size on absorption, here, we set the diameter and the period as 60 nm and 100 nm respectively and explore the effect of the Fermi level. The tunability of the Fermi level via back-gate technology is shown in Figure 4.7 (a). As investigated and demonstrated in the published journal[151], the graphene FET structure acts as a parallel capacitor; hence, the graphene layer is charged and discharged when a voltage is applied between the graphene layer and the bottom highly

doped silicon substrate. The change of the electron number in the graphene layer induces the variation in its Fermi level. As the insulating silicon oxide layer is only 300 nm, the breaking voltage is ~100 volts. The formula below shows the relationship between Fermi level and back-gate voltage; this relationship is also shown in Figure 4.7 (b), in which it is obvious that the tunability range of the Fermi level can up to 0.3 eV when 100 volts has been applied.

$$E_F = \hbar v_F \sqrt{\pi \cdot (\frac{\varepsilon_0 \varepsilon_r V_g}{d \cdot e})} \tag{4.2}$$

where, v_F is the Fermi velocity, ε_0 and ε_r are the permittivity of free space and relative permittivity of SiO_2 respectively, e is the electron charge and d is the thickness of the SiO_2 layer (300 nm in our case).

In theory, the Fermi level of graphene layer should be zero when no external electric field is applied. However, there is always finite charge present in the graphene layer, because of either induction from the absorbed impurities and substrate interface or thermal generation even without an applied electric field[161].

Because of the tunability range and initial Fermi level of the graphene layer, we simulated the surface plasmons supported by the GNM structure with Fermi level ranges from 0 to 0.5 eV (see Figure 4.7 (c)). Compared with the effect of size, Fermi level has a greater impact both on the magnitude of absorption and the shift of the resonant wavelength. The resonant wavelength blueshifts from 7.6 μm to 5.6 μm when the Fermi level is increased from 0.2 eV to 0.5 eV, while there is no obvious resonant state when the Fermi level is 0.1 eV because of the small number of electrons in the graphene layer. The larger the Fermi level, the higher the absorption magnitude.

Moreover, the absorption magnitude can reach ~ 10%, which is two orders of enhancement compared with the non-resonant state with same parameters when the Fermi level is 0.5 eV. When the Fermi level drops to 0.4 eV and 0.3 eV, the absorption magnitude decreases to 4% and 2%, respectively; the resonant peak is nearly non-observable when the Fermi level is 0.2 eV. The key point from experimentally observing these resonant peaks is to effectively tune the Fermi level away from the Dirac point as much as possible via the back-gate voltage technique.

4.4 Band gap engineering and graphene plasmons

After investigating bandgap engineering and graphene plasmons, one question that arises is whether the band gap can work side by side with graphene plasmons to enhance the absorption of light and restrain the dark current, as mentioned in the introduction to this chapter. To explore and resolve this issue, in Figure 4.8, we show the electric field distribution of the GNM structure array at resonant wavelength (a), a schematic of light absorption and electron–hole pair generation for the GNM structure with a bandgap (b) and the relation between thermal phonon, cut-off wavelength of bandgap and resonant wavelength of the GNM structure array (c).

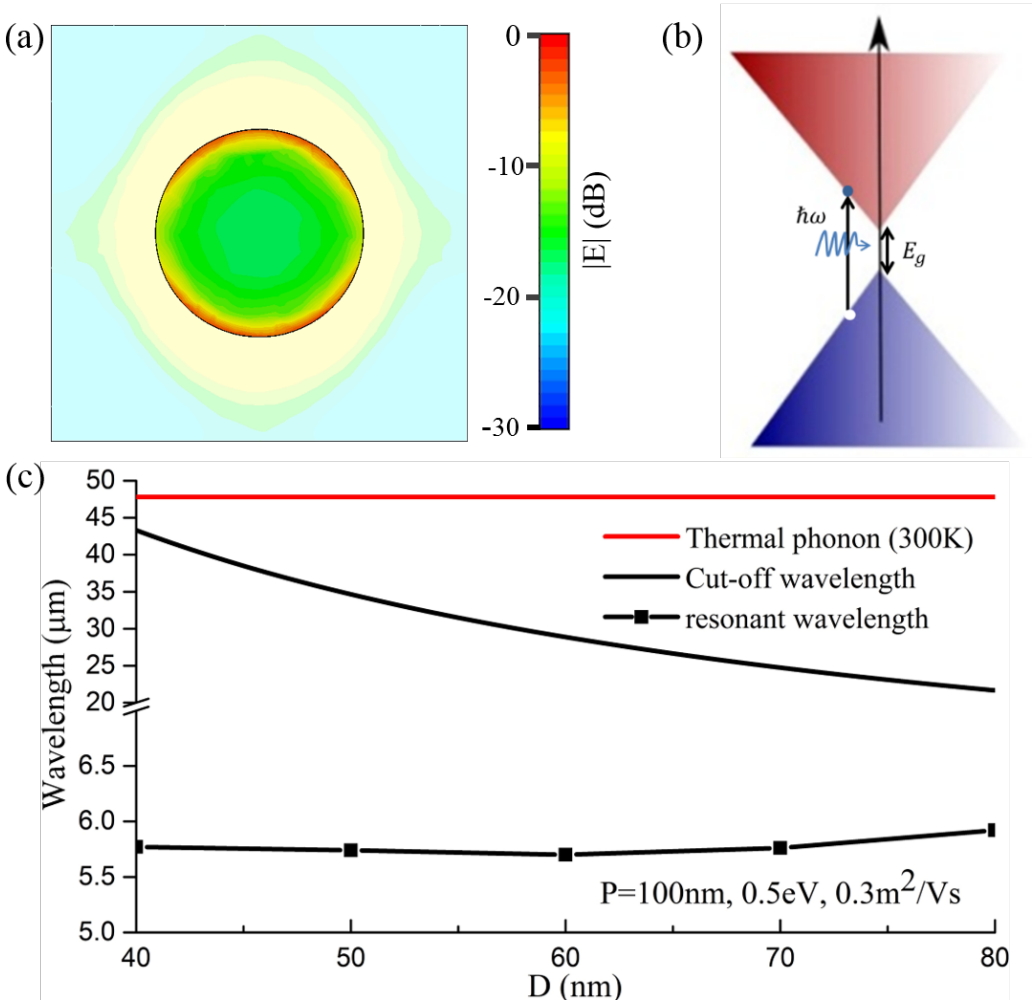

Figure 4.8 (a) The electric field distribution of GNM structure at resonant wavelength. (b) Energy band structure of GNM structure with a band gap. (c) Plots of the corresponding

wavelength of thermal phonon at room temperature, cut-off wavelength of the band gap and resonant wavelengths of GNM with period of 100 nm and varying diameters.

To determine whether graphene plasmons can work side by side with bandgap engineering, we plot and compare the resonant wavelength of graphene plasmons supported by the GNM and cut-off wavelength of the bandgap for the GNM. As shown in Figure 4.8 (c), the energy of phonon is smaller than the energy of the bandgap, which proves that the opened bandgap can effectively restrain the electron–hole recombination and thermal fluctuation. Thus, the bandgap can depress the dark current of the device and can also aid photocurrent generation.

Further, the energy of the resonant wavelength is larger than the energy of the bandgap, revealing that graphene plasmons can work side by side with bandgap engineering for the proposed GNM structure. Therefore, with a light at resonant wavelength incidence on the GNM structure, localised graphene plasmons can be excited and an electron–hole pair can be generated within the excitation of this light.

$$E_p < E_{bg} < E_{sp} \tag{4.3}$$

where E_p, E_{bg} and E_{sp} are energy of thermal phonon, energy of bandgap and energy of surface plasmons, respectively.

4.5 Discussion

To gain a better physics understanding of our proposed MIR photodetector based on a GNM platform, we exploit the theoretical investigation and numerical simulation in this chapter. Because of the limitations of the current MIR photodetector, we propose utilising the graphene platform to design and achieve a MIR photodetector that is cheaper, tunable and can work at room temperature. However, graphene still involves the intrinsic limitations of gaplessness and low absorption, as elucidated in the first section of this chapter. Therefore, to overcome these intrinsic drawbacks, we open a bandgap by fabricating a GNM structure and increase its absorption by introducing graphene plasmons.

We investigate bandgap engineering and graphene plasmons in the following two sections. To explore how large a bandgap we can experimentally achieve, we calculate the bandgap of a broad range of geometrical configurations including different defect shapes and different lattice types possessing the same hole diameter and period. The results show that the nanomesh structure with a circle unit shape arranged in a triangular array possesses a larger bandgap. The effect of hole diameter and period on bandgap is also illustrated; there is a linear relationship between hole diameter and bandgap, and a reverse relationship between period and bandgap. In addition, by considering our fabrication resolution, the achievable bandgap ranges from 20 meV to 70 meV.

Based on the calculation results for bandgap, we investigated the characteristics of graphene plasmons supported by a GNM, which possesses a large bandgap and is experimentally achievable. The absorption magnitude and resonant wavelength were determined by the trade-off between resonant mode and interaction between neighbouring holes. Moreover, an absorption up to 6.9% was reached, when the size of the hole diameter was 50 nm and period was 70 nm. The impact of the Fermi level on graphene plasmons was also demonstrated. Since the tunability of detection originates from the tunability of the Fermi level while the Fermi level of the graphene layer is adjusted by back-gate voltage, we show the relationships between these. The thickness of the silicon oxide layer determined the maximum applied voltage as ~ 100 V, which provided a Fermi level with a variation range of ~0.32 eV. Considering the initial Fermi level is normally not at the Dirac cone position, we investigated the properties of the graphene plasmons with Fermi levels from 0 eV to 0.5 eV. The resonant wavelength blueshifted and absorption dramatically increased with the increase of the Fermi level. Further,

absorption reached ~ 10% when the Fermi level was 0.5 eV, which is two orders of enhancement compared with the graphene layer with the same Fermi level at the non-resonant state in MIR.

After investigating bandgap engineering and graphene plasmons individually, the next question is whether these two can work side by side. We demonstrated our investigation in the fourth section. By comparing the energy of thermal fluctuation at room temperature, the energy of the bandgap and the corresponding energy of the resonant wavelength, we conclude that the latter is much larger than the former two, while the energy of the bandgap is larger than the energy of thermal fluctuation at room temperature. This proves that the introduced bandgap can effectively restrain electron thermal fluctuation (i.e., dark current in photodetection) and bandgap engineering can work side by side with graphene plasmons.

Chapter 5

Fabrication of GNM photodetectors

The previous chapter explored an intrinsic surface plasmons enhanced MIR photodetector. It was found that the energy of the introduced bandgap was larger than the energy of thermal fluctuation at room temperature, but smaller than the energy of the resonant surface plasmons, hence proving that the bandgap and intrinsic surface plasmons can work side by side to improve the performance of the proposed MIR photodetector by boosting responsivity and restraining the dark current.

In this chapter, we experimentally fabricate GNM photodetectors based on the knowledge gained in Chapter 4. Our characterisation results are compared with the simulation results of the previous chapter, followed by a detailed discussion. The fabrication process involves several nano-fabrication techniques, such as photolithography, EBL, e-beam deposition and reactive ion etching. Regarding the characterisation work, we exploited a home-made MIR photocurrent characterisation system, by which a comparison between the theoretical investigation and experimental characterisation is achievable.

This chapter is structured as follows. A detailed introduction is presented in Section 5.1. In Section 5.2, we report on the fabrication of the GNM structure. We then show the geometric characterisation of the fabricated structure for hole size, neck width, uniformity and roughness. The two most important characterisations—electronic and optical—are demonstrated in Sections 5.3 and 5.4. We conclude this chapter with a discussion of all results and provide an outlook for this work.

5.1 Introduction

The schematic of proposed GNM photodetector has a GNM with diameter of d nm and period of p nm as the detection platform. And a 300 nm silicon oxide layer is located between GNM and silicon layer while two gold electrodes are deposited on top of the GNM layer (see Figure 5.1).

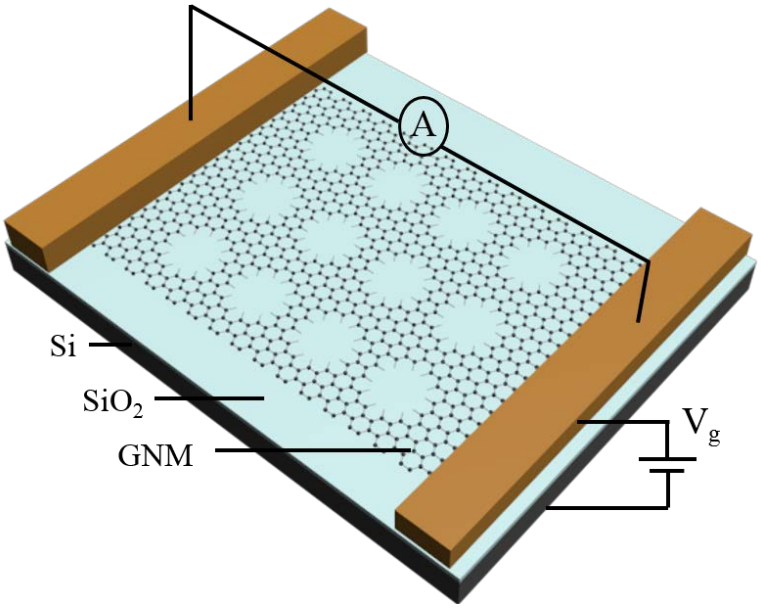

Figure 5.1 Schematic of the MIR GNM photodetector. Monolayer graphene is transferred on SiO_2/Si substrate and fabricated to GNM structure. Source and drain electrode are deposited on GNM layer and connected to measure photocurrent signal. Back gate voltage is applied between source electrode and silicon layer to tune the Fermi level of this GNM photodetector.

To experimentally achieve the GNM photodetector, the following questions are addressed in this chapter:

1. How much absorption enhanced by intrinsic graphene surface plasmons can be experimentally achieved for photodetection in the coveted MIR regime?
2. Can intrinsic graphene surface plasmons exist side by side with band-gap engineering?
3. To what degree can graphene photodetection be made spectrally selective and tuneable?

5.2 Fabrication method

The devices fabricated and characterised in this chapter are based on the typical graphene transistor design[151] with different size and shape according to specific requirements of the experiments. Here, we demonstrate the specific fabrication recipes for the GNM photodetector. As in the simulation results shown in Chapter 4, the transport mobility of the graphene layer plays an important role in the improvement of absorption at the resonant state. Furthermore, the mobility of exfoliated graphene[160, 162] is much larger than the mobility of the CVD graphene[152, 163] although CVD graphene can provide larger graphene area which is vital for the FTIR characterisation to obtain a better signal noise ratio.

To experimentally achieve the best performance of the tuneable intrinsic plasmons enhanced MIR photodetector based on a GNM platform, we fabricated the device with both exfoliated graphene and CVD graphene.

5.2.1 Graphene exfoliation and characterisation

Pristine graphene was exfoliated from the highly oriented pyrolytic graphite (HOPG) crystal using scotch tape. With one strip, the flakes were peeled from the crystal, and then other pieces of clean tape were used to peel flakes from the first one. This procedure was repeated several times case by case until the density of graphene flakes on the strip was uniform and transparent. Normally, six–seven exfoliations were enough to obtain a strip with good material density.

The prepared strip with graphene flakes was brought into contact with the SiO_2/Si substrate, which had been cleaned with acetone, IPA and plasma cleaning. Pressure was required before the strip was peeled from the substrate at relatively fast speed (see Figure 5.2). The quality and yield of monolayer graphene remaining on the surface of the SiO_2/Si substrate were determined by pressure applied and removal speed. The material density on the strip and the cleanliness of the substrate were also factors.

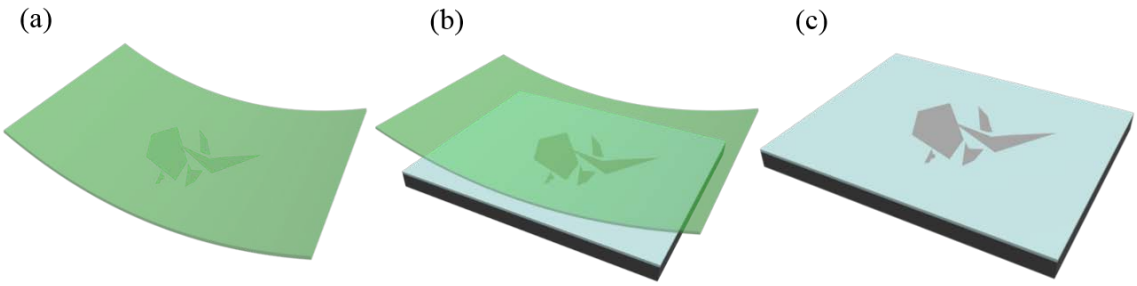

Figure 5.2 Graphene exfoliation procedure. (a) Graphene flakes are peeled off from HOPG crystal with scotch tape. (b) The scotch tape with graphene flakes is pressed onto the SiO_2/Si substrate. (c) The tape is slowly peeled off from substrate.

As the exfoliated graphene flakes were randomly transferred onto the surface of the substrate and their layer number was uncertain, characterisation and identification of the monolayer graphene was necessary. To select the monolayer graphene from all exfoliated graphene flakes, an optical microscope was used. The optical contrast [151] of graphene flakes with different layers were different (see Fig. 5.3 (a)).

5.2.2 CVD graphene transfer and characterisation

The transfer steps of CVD graphene were explained in Figure 3.11 and not repeated here.

Since the quality of CVD graphene also needed to be characterised to choose a complete area to fabricate devices, the optical image of the transferred monolayer CVD graphene is shown in Figure 5.2 (b). This can be used as a rough method to identify the location of the monolayer graphene. However, it is not possible to accurately determine the layer of the exfoliated graphene flakes with an optical image. Hence, to validate the monolayer graphene, Raman spectroscopy[164-168] was employed. As shown in Figure 5.2 (c) and (d), the layer of graphene flakes can be distinguished by the ratio between the G peak at ~ 1580 cm-1 and 2D peak at ~2700 cm-1.

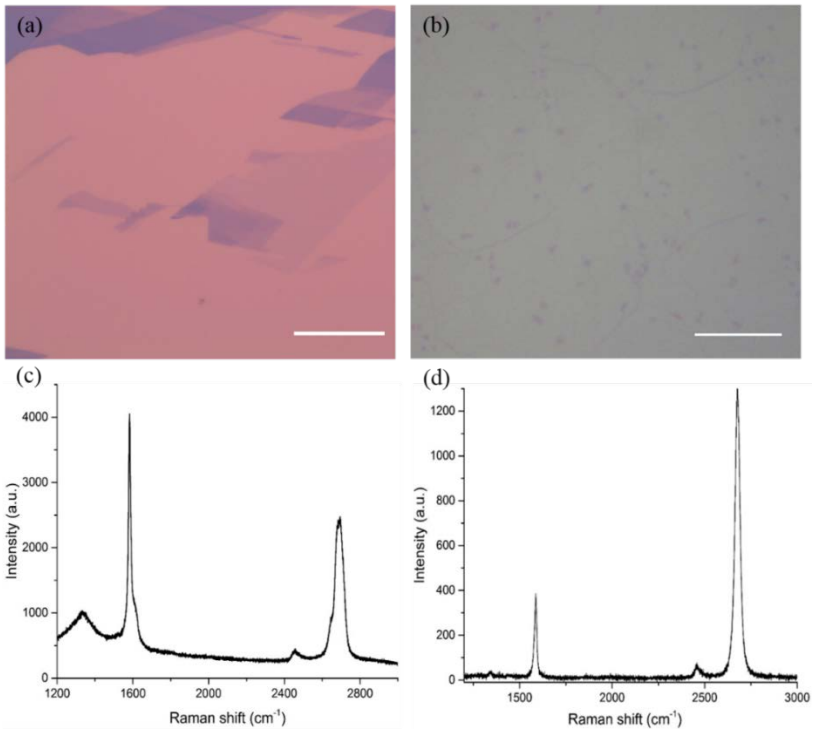

Figure 5.3 (a) Optical image of exfoliated graphene flakes on SiO_2/Si substrate. (b) Optical image of transferred monolayer graphene on SiO_2/Si substrate. Scale bar, 20μm. (c) Raman spectrum of multilayer graphene. (d) Raman spectrum of monolayer graphene.

5.2.3 Metal electrode deposition

Once the monolayer graphene was confirmed via Raman spectra, the fabrication processes of electrical devices including photolithography, e-beam evaporation, EBL, e-beam evaporation, a second EBL and reactive ion etching. Before these nano-fabrication procedures, finding a reference marker with an optical microscope, such as a large flake, is very helpful to accurately locate the position of the monolayer graphene during the process of photolithography. The schematics of these procedures were shown in Section 3.4. Here, the first EBL and the following e-beam evaporation were optional, depending on how big the monolayer graphene was, since their function is to connect the exfoliated graphene layer and the large electrodes patterned with photolithography. The second EBL was used to expose the nanomesh pattern on the PMMA layer; the pattern was then transferred to the graphene layer by following the reactive ion etching. The optical image and SEM image of the fabricated device are shown in Figure 5.4.

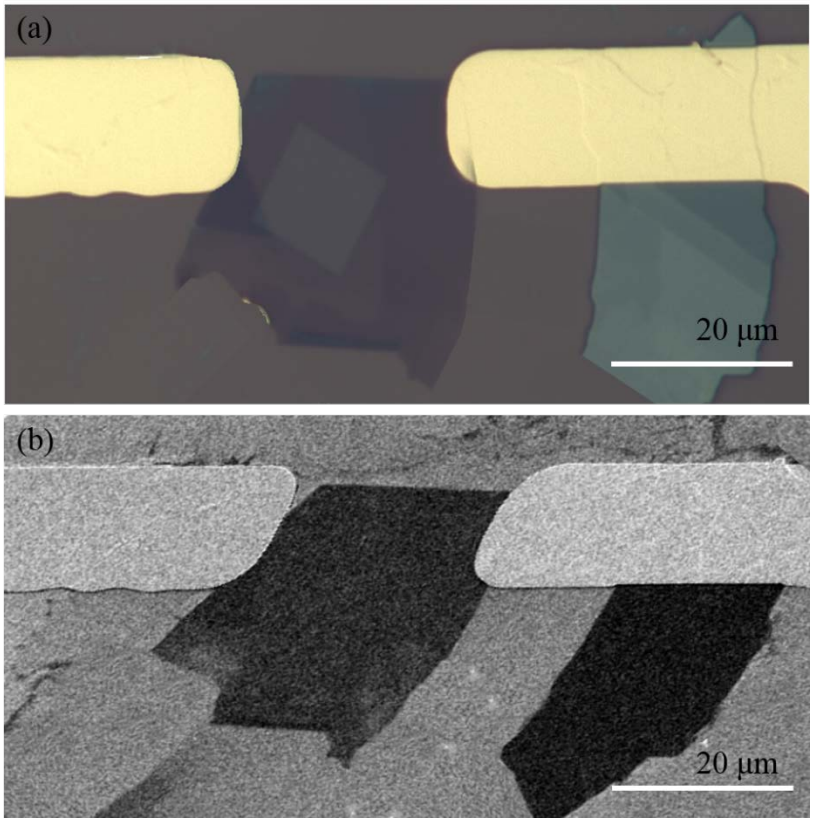

Figure 5.4 (a) Optical image and (b) SEM image of fabricated photodetector with exfoliated monolayer graphene flake.

Although exfoliated monolayer graphene possesses the advantages of high carrier mobility and fewer defects, there are also many drawbacks, such as low yield and small size. A large area of monolayer graphene is needed for a reasonable signal–noise ratio in the FTIR characterisation; therefore, the fabrication of CVD graphene is investigated and demonstrated in the following section.

5.2.4 GNM fabrication

The basic concept and process of the wet transfer of CVD graphene was shown in Figure 3.12. However, there is an additional step required in this chapter to pattern graphene into the designed shape to avoid problems such as too large an area or too many defects. Here, we briefly introduce how to etch the desired graphene shape after it has been transferred on to the SiO_2/Si substrate.

After the CVD graphene has been transferred to the substrate, the expected pattern of graphene is transferred from the pattern of the exposed PMMA layer that was spin coated on top of it via a lithographic technique and the ensuing etching (see Fig. 5.5). Depending on the feature resolution, a selected area is exposed by either an electron beam or UV light, making it soluble in a developer. After development, the designed pattern will show up on the PMMA resist layer. Following this, a treatment with an oxygen plasma etching in a reactive ion etching (RIE) system is performed to remove the graphene areas, where there is no PMMA resist. The last step is to rinse the PMMA resist, after which the expected pattern will show up on the graphene layer. The SEM image of the transferred graphene on the substrate is shown in Fig. 5.6.

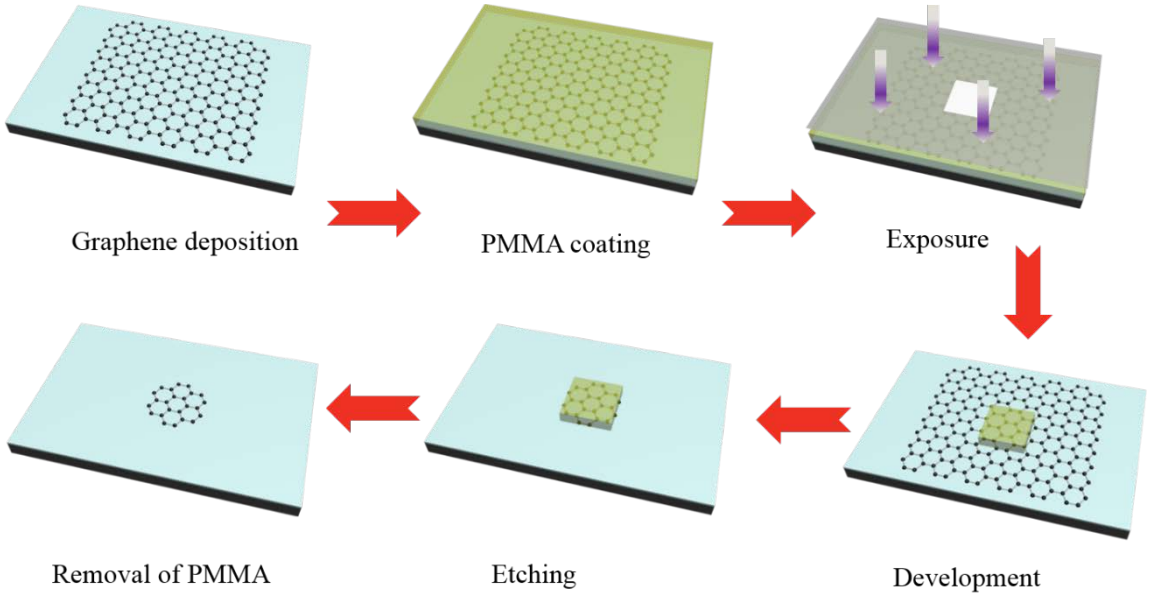

Figure 5.5 Schematic of the steps to etch graphene layer to a desired shape. Colour code: grey/light blue: SiO_2/Si substrate, light green: PMMA resist.

To select a graphene area of high quality, Raman spectra was performed to ensure that there was no fold or damage; an optical microscope or even a scanning electron microscope is used to confirm the selected area.

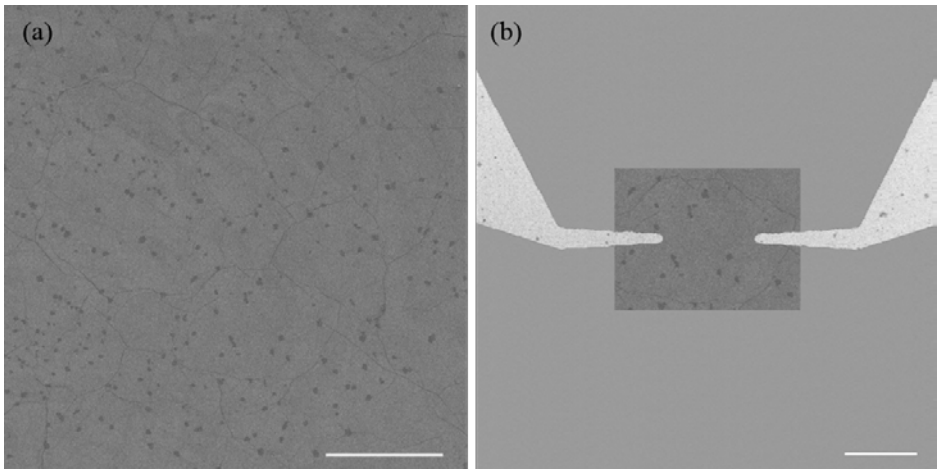

Figure 5.6 (a) SEM image of transferred CVD graphene on SiO_2/Si substrate. (b) SEM image of etched graphene after deposited with metal electrodes. Scale bars are 50 μm.

After exfoliating and obtaining a larger enough monolayer graphene or etching transferred CVD graphene to a desired shape, fabrication of the electrode is required for signal measurement by wire bonding. The SEM image of a device fabricated with etched graphene and electrodes deposition is shown in Figure 5.6. The fabrication process is similar to that shown in Figure 3.13; the only difference here is that EBL was used to expose for cases that involved small and fine electrodes. Therefore, we demonstrate the fabrication process of the GNM pattern after the electrode deposition in the next section.

Because of the nanoscale size of the desired GNM array structure, EBL performed with Vistec EBPG5000plusES was used to write the pattern. During the lithography process, a focused electron beam generated by an electron beam pattern generator (EBPG) scanned on a PMMA resist layer covered on the substrate. The scanning of the electron beam followed the designed pattern.

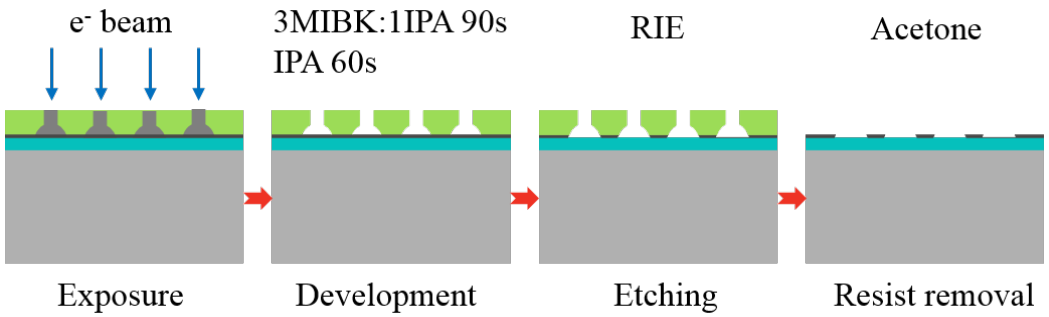

Figure 5.7 Schematic of the fabrication process of GNM pattern. Colour code: grey/light blue: SiO_2/Si substrate, black: graphene, light green: PMMA resist.

As shown in Figure 5.7, chemical modifications in the electron resist are introduced by the electron beam and the pattern on the resist can be transferred on the graphene layer. This is the main principle of the fabrication process of the GNM array. Here, we used a positive electron resist; therefore, the exposure area could be selectively dissolved in certain solvents. However, because of the backscattered electrons from the SiO_2/Si substrate, the shape of the exposed area was not a uniform cylinder as designed. Therefore, the exposed size should be smaller than the expected size and a recipe with all the related parameters needed to be developed.

After development, the unexposed resist was a mask protecting the underlying graphene from etching; the GNM will show up after the resist removal. These fabrication processes can be repeated to fabricate much more complex shapes. Further, alignment markers are needed for fine alignment each time. Characterisation with SEM and AFM was performed to check the exact size and shape of the fabricated structure to give feedback for the fabrication recipes. Moreover, the exact size data from the characterisation can be used for the initial parameters of the simulation to compare the simulation and experimental results. The characterisation work for the GNM array structure is illustrated in the following section.

5.3 Geometric characterisation

Because the quality of the fabricated GNM determines the quality of the proposed MIR graphene photodetector, the geometric characterisation of the GNM structure is explored and demonstrated here. In this section, characterisation of three aspects—hole size, neck width, roughness and uniformity—is investigated.

5.3.1 Hole size

As explained in the previous section on the process of GNM fabrication, the cross section of an exposed circular hole is an irregular shape instead of a regular rectangular shape (see Figure 5.8). Therefore, the size of the etched holes is different from the designed value. Moreover, there are many other factors, such as focused electron beam size, dose range, development time and etching time, that can affect the size and shape of the final fabricated nanomesh structure. A well-developed fabrication recipe was obtained over many trials and used for the GNM array fabrication.

To push our fabrication limit to the expected size (around 50 nm), we started to fabricate the nanomesh array with a larger hole size (150 nm) and then shrunk the size step by step. In Figure 5.8, an overview of the fabrication area is shown in (a) and a GNM array with hole size of 150 nm and period of 300 nm is shown in (b). It can be qualitatively distinguished from these two figures that the fabricated hole array is very uniform and the measured hole size matches well with the designed size. The quantitative analysis results are in Figure 5.8.

Although the actual GNM size was determined by many factors, such as the electron beam current, dose range and etching time, the most critical and tricky factor was the electron beam current. Therefore, we investigated the dependence of the measured diameter size of the nanomesh array structure on the electron beam current, which also implies the focused spot size when all other parameters are the same, and plotted their relationship in Figure 5.9. As can be see, there is no significant difference in the fabrication results whether a higher electron beam current (10 nA) or a lower electron beam current (2 nA) is used if the designed diameter is larger than 100 nm. Moreover, their deviation is only ~5nm (<5%), which proves this is very high-quality fabrication work, especially considering the nanoscale size and complex fabrication steps. On the other hand, a smaller electron beam current gives a better result at the

cost of a much longer fabrication time. Therefore, by considering the fabrication error and time, we conclude that electron beam current of 10 nA with a spot size of 10 nm is the optimised EBL option for fabrication of the GNM array with hole size larger than 100 nm.

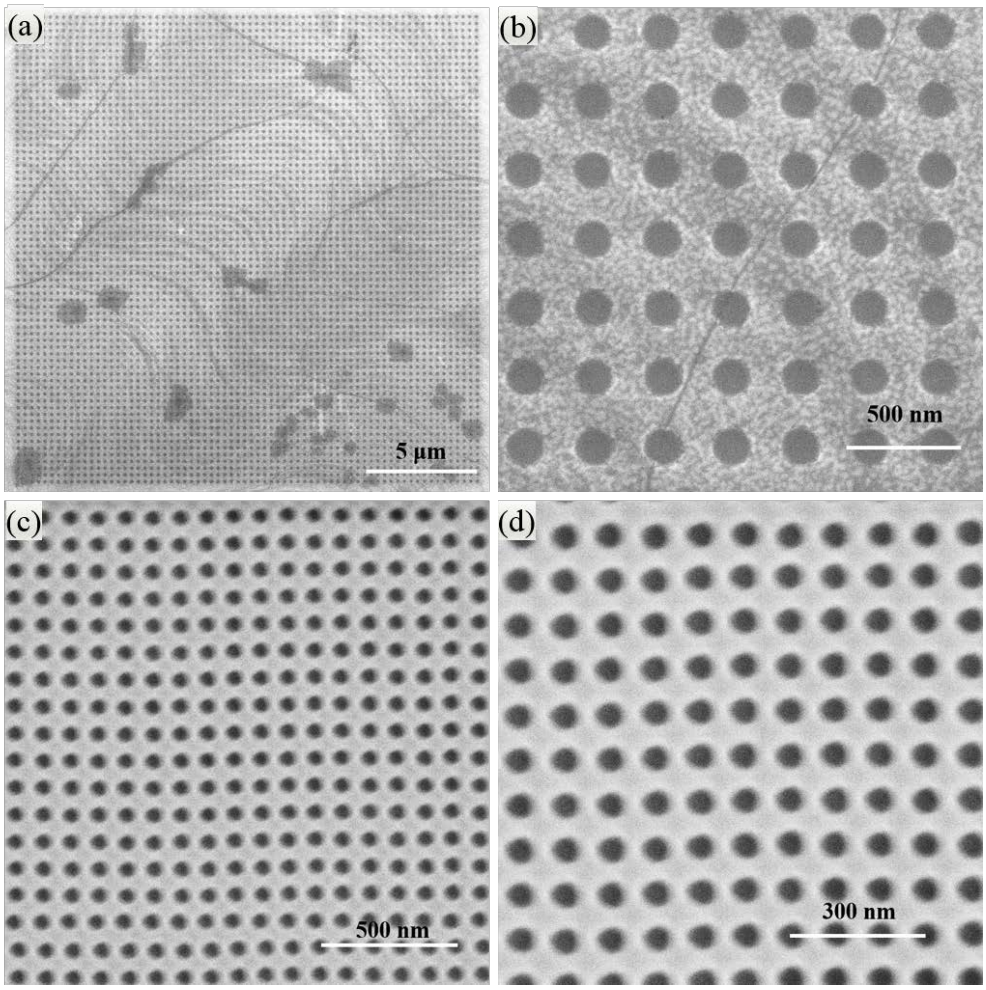

Figure 5.8 SEM images of fabricated GNM array structure. (a) An overall view of fabricated GNM array. (b) GNM array with diameter of 150nm and period of 150 nm. (c) (d) GNM array with diameter of 50 nm and period of 100 nm.

After obtaining the optimised experimental conditions for a larger nanomesh, we shrunk the fabrication hole size from 100 nm to 40 nm with same period/diameter ratio of two. The SEM images of the GNM array structure with hole diameter of 50 nm and period of 100 nm are shown in Figure 5.8 (c) and (d). The quantitative analysis results are presented in Fig. 5.9.

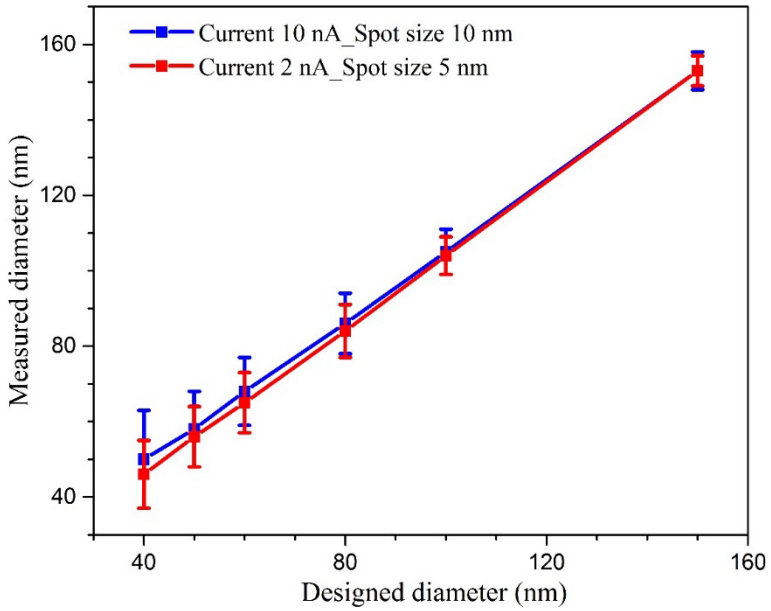

Figure 5.9 Measured dependence of GNM diameters on the electron beam current when compared with the designed diameters.

Contrary to the results of hole size with diameter of 100 nm and 150 nm, a smaller electron beam current plays an important role in the accuracy of the fabrication structure, as clearly shown in Figure 5.9. The experimental diameter sizes are closer to the designed value if the smaller electron beam current is used, especially for the fabrication of nanomesh with diameter smaller than 80 nm. And with our optimised recipe, the variance is only ± 5 nm when the fabrication diameter is 50 nm or even 40 nm. Therefore, an electron beam current of 2 nA is needed for the fabrication when the hole diameter is smaller than 80 nm, even at the cost of exposure time.

Compared with the simulation results in Chapter 4, we experimentally achieved the smallest diameter of 40 nm. In addition, the red or blueshift of resonant wavelength produced by the ± 5 nm variance of the diameter was within 100 nm, which is unlikely to lead to side effects from the application point of view.

5.3.2 Neck width

The diameter of the nanomesh structure investigated in the last section is a key parameter to evaluate how small we can fabricate with current experimental conditions; it also plays an important role in graphene plasmons resonance. Therefore, we fully investigated this in last section and concluded with the choice of fabrication parameters for different sizes of GNM. However, the neck areas (the areas between the adjacent holes) play an important role in the performance of bandgap engineering and graphene absorption. Hence, this section explores fabrication work in light of neck width.

The SEM images of fabricated nanomesh arrays with different neck widths are shown in Figure 5.10. It can be seen that GNM with neck width down to 10 nm (the smallest possible neck width here) has been uniformly fabricated.

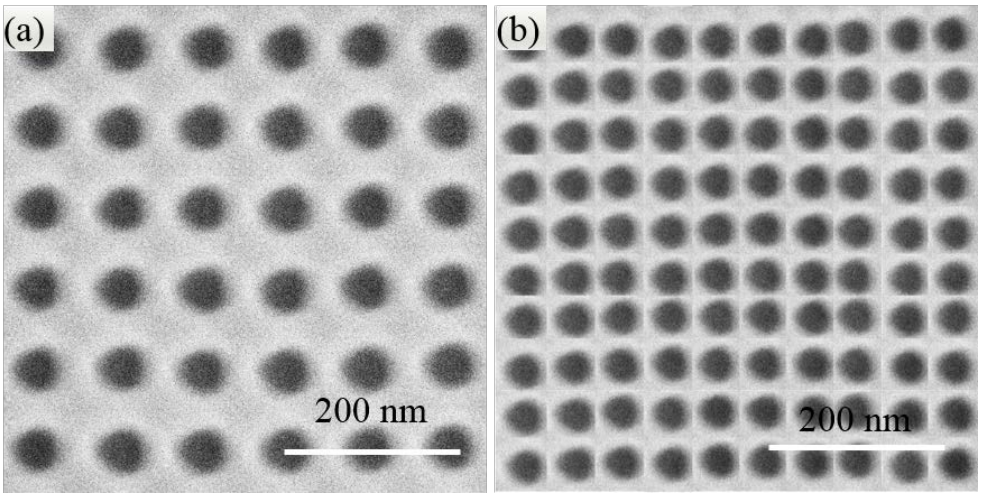

Figure 5.10 SEM image of GNM with different neck width. (a) GNM with hole diameter of 50 nm and neck width of 50 nm. (b) GNM with hole diameter of 50 nm and neck width of 10 nm.

As investigated in Chapter 4, neck width contributes to the quantum confinement effect, which produces the bandgap of GNM structures. Therefore, for one specific period, the smaller the neck width, the larger the bandgap. Here, we experimentally achieved neck width of 10 nm when the period was only 60 nm; this produced a bandgap of 49 meV.

5.3.3 Uniformity

Because the actual shape of the fabricated circle has a vital influence on resonant properties, the property of uniformity is investigated here. From the previous SEM images, it is evident that the fabricated nanomesh is quite circular. However, to quantitively show uniformity we measure one batch of samples and analyse the results (shown in Figure 5.11). Although the results shown here are not based on all the samples, the number of analysed samples is sufficient to represent the quality of the fabrication recipes.

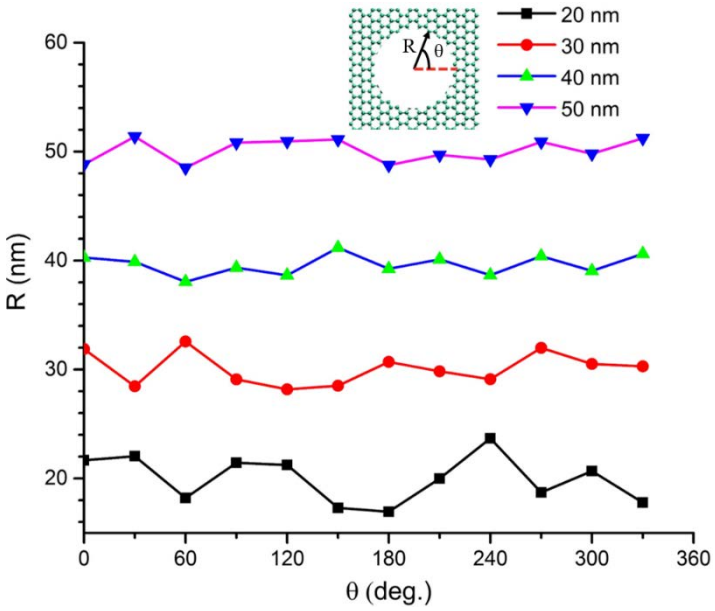

Figure 5.11 The average radius of fabricated GNM of different diameters along radial direction.

As illustrated in Figure 5.11, the larger the diameter, the more accurate the result. The aspect ratios between the shortest axis and longest axis are 0.73, 0.87, 0.93 and 0.95 for radii 20 nm, 30 nm, 40 nm and 50 nm, respectively. Hence, the fabricated GNM is quite circular, especially when the diameter is above 50 nm.

5.3.4 Roughness

The roughness of the fabricated GNM structure must also be characterised as too much PMMA residual can have an effect on the mobility and absorption efficiency of the graphene layer. Figure 5.12 shows roughness investigated via AFM images for GNM with a spacing of 100 nm and different diameters.

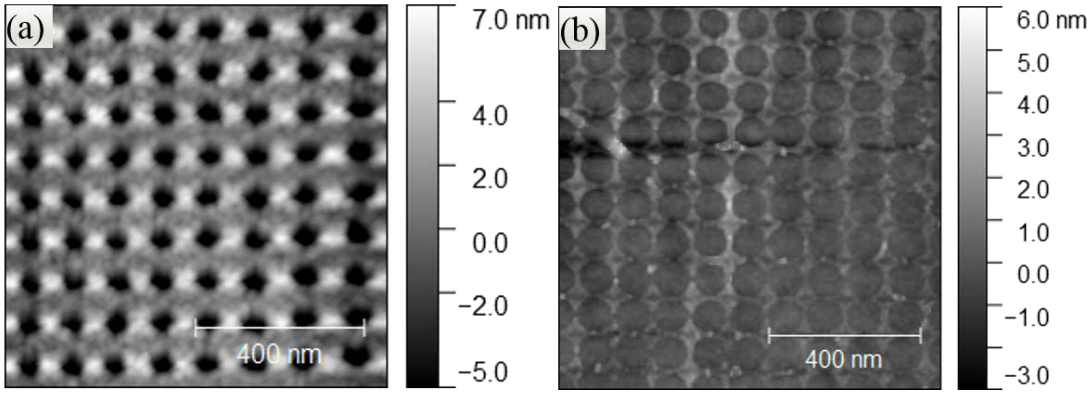

Figure 5.12 (a) AFM image of GNM with diameter of 50 nm and period of 100 nm. (b) AFM image of GNM with diameter of 90 nm and period of 100 nm.

The height distribution in the AFM image shows the roughness of the fabricated device. The above figures indicate average height is about 5 nm. Because the theoretical thickness of the graphene layer is about 1 nm, there is some PMMA residual on the graphene layer even after the special treatment with plasma and oven. This PMMA residual can lower the charge mobility of the graphene layer and affect the absorption of graphene, weakening the performance of the GNM photodetector. A further process of removing the PMMA residual is needed.

5.4 Electronic characterisation of Fermi level

After the fabrication work and ensuing geometric characterisation, an electronic characterisation proceeded with an aim of determining the intrinsic doping level and estimating its mobility. Here, we measured the source-drain current when changing the back-gate voltage to tune the carrier concentration of the graphene layer and therefore its resistance (see Figure 5.13). The graphene layer was transferred on the SiO_2/Si substrate with a thickness of 300 nm SiO_2 and then fabricated to the GNM array pattern. By applying a back-gate voltage between the backside Si and top electrode, deposited on top of the graphene layer, a potential drop is created across the SiO_2 insulating layer. This setup resembles the capacitor structure and hence the back-gate voltage (V_g) induces the accumulation of surface charge density (n) in the graphene layer according to the following equation:

$$n = \frac{\varepsilon_0 \varepsilon_r V_g}{d \cdot e} = \alpha \cdot V_g \tag{5.1}$$

where ε_0 and ε_r are the permittivity of free space and relative permittivity of SiO_2 respectively, e is the electron charge and d is the thickness of SiO_2 layer (300 nm in our case). Moreover, there is a relationship between carrier density and Fermi level as shown in the equation below:

$$E_F = \hbar v_F \sqrt{\pi \cdot n} \tag{5.2}$$

From this equation, Fermi levels up to ± 0.3 eV can be modified when applying ± 100 V. However, the reachable graphene Fermi level is limited by the breakdown voltage of the gate dielectric material. As a rule of thumb, 30–40 V per 100 nm can be safely applied to the typical SiO_2/Si case.

If the graphene is neutral, its Fermi level lays at the Dirac point where graphene exhibits the largest resistivity. However, normally the graphene is p^+ doped[41] due to the reason that there is some oxygen and water adsorbates. Hence, in this case, the above equation needs to be revised to:

$$n = \frac{\varepsilon_0 \varepsilon_r (V_g - V_{Dirac})}{d \cdot e} = \alpha \cdot (V_g - V_{Dirac}) \tag{5.3}$$

Here, the Dirac voltage V_{Dirac} serves as an offset value for the tuning of charge carriers concentration via back-gate voltage. Moreover, it can be used to calculate the initial Fermi level of the fabricated graphene-related device.

In the graphene layer, mobility indicates the strength of scattering mechanisms, including intrinsic scattering and extrinsic scattering. Intrinsic scattering refers to scattering on phonons while extrinsic scattering refers to scattering on defects, impurities and adsorbates. Hence, the quality of the carrier mobility reflects the quality of the fabricated devices. Further, mobility has an effect on retardation time, effectively influencing the resonance of the GNM structure.

Mobility can be measured and calculated based on the formula below:

$$\mu_i = \frac{1}{n_i \cdot e \cdot \rho} \tag{5.4}$$

where, i and ρ denote electrons or holes and resistivity respectively.

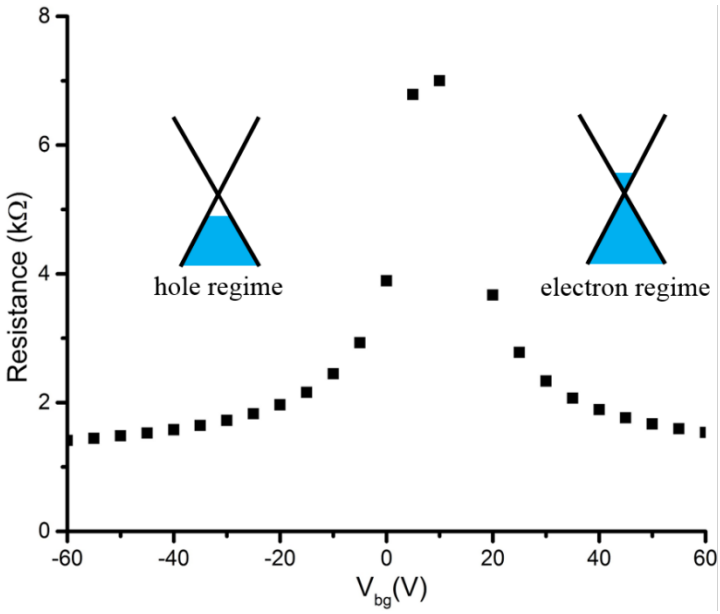

Figure 5.13 Measured graphene resistance as a function of back gate voltage.

Therefore, mobility can be verified by measuring resistivity at different back-gate voltages. The linear relationship between mobility and conductivity (the inverse of electrical resistivity) can be gleaned from the equation above. Therefore, one can directly fit conductance as a function of back-gate voltage to estimate the mobility of electrons and holes.

In Figure 5.13, we show a typical measurement of resistance as a function of back-gate voltage. From the figure, it is evident that the Dirac point is around 10 V, which corresponds to an

initial Fermi level of 0.198 eV according to the above equations. Further, values of ~ 3250 $cm^2V^{-1}s^{-1}$ and 3013 $cm^2V^{-1}s^{-1}$ are extracted from the measured curve for the mobility of electrons and holes respectively.

Compared with the simulation of graphene plasmons with different Fermi levels in Chapter 4, we conclude that the Fermi level can be effectively tuned and a value of 0.5 eV is experimentally achieved with our fabricated devices. This is because the initial Fermi level is 0.198 eV and an increase of 0.3 eV can be achieved when adding a 100 V back-gate voltage. However, as demonstrated in the previous section, the AFM images show there is a ~ 4 nm thick PMMA residual on the GNM layer, which will also affect the tunability of the GNM structure.

5.5 Optical characterisation

Two aspects of characterisation were discussed in previous sections: geometric characterisation explored the fabrication quality of GNM structures and gave the exact experimental size of the devices, while electrical characterisation elucidated the transport property of the GNM layer with the measurement of the initial Fermi level and carrier mobility. Moreover, varying resistance also proved the tunable ability of our fabricated GNM photodetectors. Here, we measure the transmission spectra of GNM structures under different back-gate voltages and the spectra of pure substrates to characterise the tunable intrinsic graphene plasmons supported by the GNM structure.

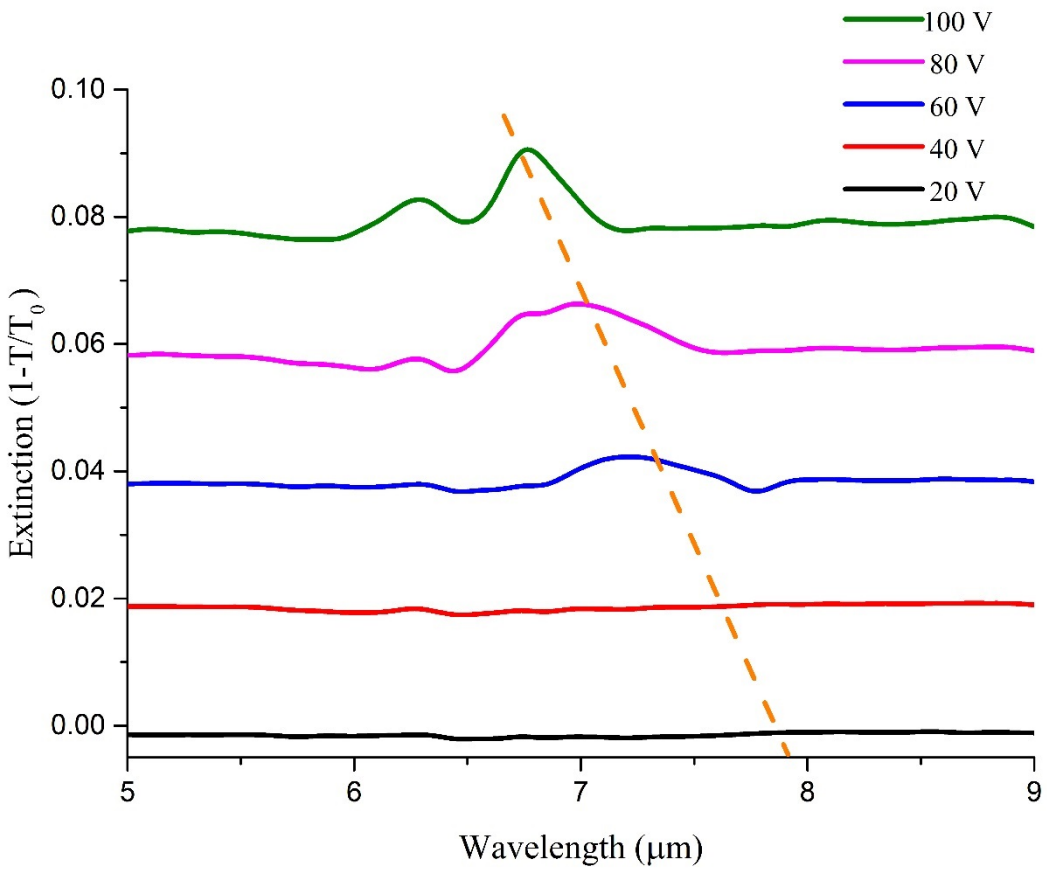

Figure 5.14 Extinction spectra for GNM arrays with hole diameter of 50 nm and period of 100 nm at varying back gate voltage (chemical doping level/Fermi level) as indicated.

Figure 5.14 shows an extinction spectrum measured on a GNM array with hole diameter of 50 nm and period of 100 nm. The extinction is defined as the ratio between the transmission through the array and the transmission through the bare substrate of same size without graphene[100, 156-158]. This extinction spectrum indicates the enhanced light absorption corresponds to the resonance due to the excitation of intrinsic graphene plasmons[100].

The graphene plasmons mode was shifted by changing the Fermi level via back-gate voltage from 6.8 μm with 1.2% absorption to 8.2 μm with 0.12% absorption (see Figure 5.14). furthermore, absorption was enhanced up to one order of magnitude at resonant wavelength compared with the general absorption at MIR wavelength range.

Compared with the simulation results in Chapter 4, we conclude that the Fermi level of our GNM photodetector is only ~ 0.3eV when the applied back gate voltage is 100 V while the absorption resonant peak is lower. This is because of the effect of the PMMA residual and because the sizes do not perfectly match our design.

At a back gate voltage greater than 100 V, the oxide layer of the substrate begins to break down permanently, catastrophically destroying the detector. It is also necessary to ensure that the oxide layer is free from defects to avoid providing an avenue for the gating charge to leak out to ground and return the Fermi level to its original substrate doped level. For the silicon wafers purchased in this experiment, the quality of the oxide layer was poor such that only a handful of detectors that were fabricated were capable of Fermi level tuning to the extent needed for surface plasmon resonances. The use of higher quality silicon, or the deposition of pure oxide layers would provide a resolution to the discharge, but could not be carried out in the timeframe of this project.

5.6 Photodetection characterisation system

To validate the photo-response property of our fabricated device, after the geometric, electrical and optical characterisation, we performed the photocurrent characterisation with our home-made MIR photocurrent characterisation system. The femtosecond source laser (pulse rate is 5 kHz) was produced by the Astrella and transformed to MIR wavelength after it go through the Non-collinear Difference Frequency Generator (NDFG). This was used as the excitation source light to illuminate the samples mounted on a motorised stage.

Each electrode was electrically wired to a photocurrent measurement system which is used to characterise the sign and magnitude of the generated photocurrent. Figure 5.11 shows a schematic of the optical and electronic characterisation system. MIR light is generated by difference frequency generation (DFG) from the output of an optical parametric amplifier (Light Conversion Topas + DFG1) pumped by a Coherent Astrella amplified Ti-Sapphire laser. A broadband linear polarizer (Thorlabs WP25H-B) was used to lower the laser power of incident light. A 75 mm CaF2 singlet lens was used to illuminate a variable size of the detector. The beam diameter entering the lens was 10 mm such that the numerical aperture of the illumination was 0.07. The illumination area was adjusted by translating the detector along the optical axis and a broadband 50:50 beamsplitter (Thorlabs BSW521) was used to enable visible light imaging via a LED/CCD based reflection microscope. The photocurrent generated by the detector was amplified by a low noise current preamplifier and detected by a lock-in amplifier (Stanford Research Systems SR570/SR530) locked to the 5 kHz frequency of the pump laser.

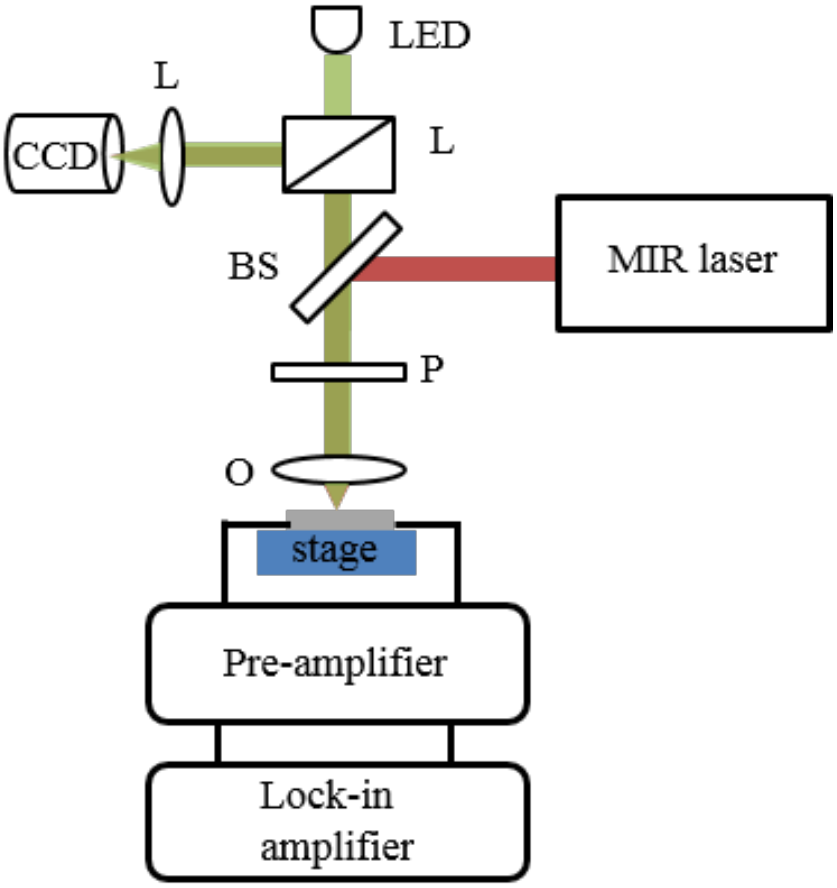

Figure 5.15 Schematic of the MIR photodetector measurement setup.

Do to the presence of silicon impurities in the oxide layer of bought wafers, the detectors fabricated at the end for use in photocurrent measurements did not show signs of surface plasmon resonance. Accordingly, no resonances were detected in the photocurrent. Future work on this project will involve the deposition of a pure oxide layer onto the silicon substrates such that the fermi level can be regularly tuned to the levels needed to support surface plasmon resonances.

5.7 Discussion

In this chapter, we successfully developed a recipe and fabricated the proposed photodetectors based on the GNM structure which were investigated in Chapter 4. To provide feedback for the fabrication recipe and guarantee that the fabricated structure is consistent with the design, a characterisation with AFM and SEM was conducted. The results show that there is only ± 5 nm error when the hole diameter of the nanomesh array is 50 nm and the error can be reduced to ± 2 nm if the hole diameter of the nanomesh array is 100 nm. Regarding the circularity of the fabricated nanomesh array, the aspect ratios between the shortest axis and longest axis are 0.73, 0.87, 0.93 and 0.95 for radii 20 nm, 30 nm, 40 nm and 50 nm, respectively. Hence, the fabricated GNM is quite circular especially when the diameter is above 50 nm.

Using the geometric characterisation to confirm the successful fabrication of desirable GNM structures, electrical and optical electrical characterisation have also been proceeded. The change of resistance shows the effective tunability of Fermi level via back gate voltage. And the tunable range of Fermi level from 0 to 0.5 eV has been experimentally achieved. Most importantly, we characterise the graphene plasmons on our device with FTIR and it consists with simulation result. A tuneable range of Fermi level of 0.3 eV and the corresponding resonant wavelength range from 6.8 μm to 8.2 μm have been achieved. And absorption magnitude up to 1.2 % has been achieved at resonant wavelength of 6.8 μm.

However, because of the impurity of the silicon oxide layer (that grew organically on the silicon layer), there was a current leakage problem that prevented us from characterising the photocurrent properties when applying back-gate voltage. These impurities, located under the graphene, provide an avenue for the injected charge to escape, and thus, there was no doping in the graphene layer and no change in the Fermi level when we applied a back-gate voltage to measure the photocurrent. Unfortunately, this problem was not able to be resolved during this PhD. However, we have formulated several possible approaches to solve the problem: we could either purchase a high-quality SiO_2/Si wafer or deposit the 300 nm thick silicon oxide layer on a silicon wafer.

Chapter 6

Conclusion

6.1 Thesis conclusions

In this thesis, we have theoretically and experimentally investigated the optoelectronic properties of proposed graphene photodetectors. A broad range of contents, such as the interaction between light and graphene, the development of nanofabrication methods for delicate devices, the design and optimisation of graphene photodetectors and the construction of characterisation systems, have been investigated and exploited. Several innovative achievements towards the development of room temperature MIR photodetectors that have been made in this thesis can be summarised in the following contents.

Circularly polarised light has been extensively used in multiple areas, such as spin optical communication and quantum computing, however, there is an inherent difficulty for the conventional photodetectors that based on traditional semiconductors to distinguish the circular polarisation states of circularly polarised light due to the reason that traditional semiconductors lack of intrinsic chirality. Moreover, mid-infrared photodetectors often suffer from inferior performance compared with their visible or near-infrared counterparts due to the reasons of less mature materials processing protocols and more susceptible to thermal fluctuations. These limitations not only impede the development of miniature and integration of photonic devices but also reduce the detection efficiency. Therefore, the exploration and

investigation of new materials or new design for the mid-infrared spin angular momentum detection is necessary and needed.

To solve the issues of less mature materials processing protocols and lacking intrinsic chirality of current MIR photodetector, we took advantage of graphene and metal chiral structure to fabricate MIR photodetectors and achieve the direct deduction of photon spin angular momentum at the first atmosphere transmission window.

In the first work of our research, we have designed and fabricated an integrated mid-infrared graphene photodetector which can directly detect the SAM states associated with incident LCP and RCP light. In this work, we utilised zig-zag surface plasmon electrodes of opposite handedness to enhance graphene absorption by one order of magnitude to a maximum of 41% for LCP and minimum of 7.5 % for RCP to produce a CD of 69% after optimizing the structure sizes. Then we fabricate the designed devices and observe a peak responsivity of 0.80 μA/W and photocurrent circular dichroism up to 66.7% at a resonant wavelength of 3.8 μm, corresponding to the first atmospheric transparency window useful for emerging high bandwidth applications such as LiFi and LiDAR. With this detector, we have shown that the SAM states associated with LCP and RCP can been directly distinguished by the sign of the produced photocurrent. Due to the reason that the chirality and resonant wavelength of our photodetector results from the chirality and size of the surface plasmon electrodes instead of the intrinsic properties of any of the materials, many other electrode geometries can be incorporated into the one device to enable detection of other multiplexed states, such as wavelength and orbital angular momentum (OAM). Hence, our work shows one novel solution for the detection of angular momentum states of mid-infrared light.

Because the surface plasmons supported by gold metal chiral structures is parasitic, therefore, in order to effectively utilise the enhancement function of surface plasmons, we investigate the graphene plasmons to improve the performance of mid-infrared photodetection. Then we proposed the GNM structure which not only possess an energy band gap but also supports plasmons as the photodetection platform to improve the photodetection performance. For the first time, we propose to combine band gap engineering and graphene plasmons for photodetection and theoretically proved that they can simultaneously improve the absorption enhancement and restrict dark current.

We have theoretically investigated the relationship between the sizes of GNM structure, the arrangement pattern and band gap size. In addition, we simulate the graphene plasmons for

GNM platform with different defect shapes and arrangement shapes. It is shown that the energy of opened band gap is larger than the energy of thermal fluctuation at room temperature whilst smaller than the corresponding energy of resonant wavelength of surface plasmons. This comparison means that the introduced band gap can effectively restrain the dark current at room temperature while band gap engineering and graphene plasmons still can work side by side. Furthermore, by considering the size of band gap and our achievable fabrication resolution, we choose the GNM structure with circular defect shape and square arrangement shape. Although, this structure array exhibits the second largest band gap, it is much more achievable and repeatable. Therefore, we choose this type of GNM structure to fabricate graphene photodetector working at the mid-infrared (5-7 μm).

Then the GNM structure with circle diameter of 50 nm and period of 100 nm on SiO_2/Si substrate is fabricated and characterised. And with optimised recipe, the error range is only ± 5 nm when the fabrication diameter is 50 nm or even 40 nm. Due to the neck width of GNM structure determines the remaining carbon atoms which contributes the size of introduced band gap, we can experimentally achieve the neck width down to 10 nm when the diameter is 50 nm. Furthermore, the average aspect ratio between the shortest axis and longest axis of 0.95 is achieved when the diameter is 50 nm, which proves that the fabricated circle is very uniform and circular. Electronic characterisation shows the tuneability of Fermi level of our fabricated GNM platform like graphene layer. And the relationship between resistance and back gate voltage shows the initial Fermi level is 0.198 eV for our normal fabricated GNM structure. Most importantly, the graphene plasmons supported by this nanomesh structure has been experimentally characterised with the optical method. The extinction spectrum shows that the resonant wavelength shifts from 8.1 μm to 6.9 μm when the back-gate voltage changes from 20 V to 100 V.

In summary, this PhD thesis has focussed on the innovative research of mid-infrared graphene photodetection enhanced by surface plasmons. In particular we have experimentally achieved the direct detection of photon spin angular momentum by a chiral graphene MIR photodetector which solved the problems of low working temperature of current MIR photodetection and lacking intrinsic chirality of semiconductors. Moreover, we also experimentally fabricated the GNM photodetectors and achieved the tunability of intrinsic graphene plasmons via back gate voltage. All these researches open up new avenues for multifunctional MIR photodetection with high performance.

6.2 Future work

In this section, we discuss the future work of this research and proposing several possible research projects based on the results of this PhD thesis.

We have shown the work of direct detection of photon spin angular momentum with the demonstrated graphene photodetector in chapter 3. Compraed with spin angular momentum, the detection of orbital angular momentum with compact optoelectronic components is much more exciting and yet to be investigated. And we have shown the novle way of combing the plasmonic structures with graphene material. Therefore, the direct detection of orbital angular momentum can also be achived with delibrate designed some surface plasmon structure and combine with graphene layer to achieve this goal. Furthermore, more unit cells can be integragted within one chip to achive multiple channels detectoin for different modes of orbital angular momentum. Similarly, fabricated graphene nanostructures can also support resonant plasmons with strong near field enhancement, which menas that the novel graphene structure can be designed and utilised to achieve the same function as the metal surface plasmon to detect orbital angular momentum.

We have shown the fabrication work of graphene nanoemsh detector and some related characterisation work has also been demonstrated. However, we haven't characterise the photocurrent characteristic of this grapheen nanomesh photodetector. Therefore, one future work is to fullly characterise the photocurrent property of the graphene nnaomesh photodetector.

Due to the reason that many other 2D materials, such as TMDCs, black phosphorus and h-BN thrived in the past few years, and some of them have unique property, such as intrinsic band gap, compared with graphene. Therefore, how to utilise the advantages of each 2D materials and combined them together to achive photodetectors with high performance is another future work.

References

[1]. Fournel T, Javidi B. *Information optics and photonics: algorithms, systems, and applications*. Springer Science & Business Media (2010).

[2]. Stanley R. Plasmonics in the mid-infrared. *Nature Photonics* **6**, 409, 2012.

[3]. Hoffman A, Gmachl C. Extending opportunities. *Nature Photonics* **6**, 407, 2012.

[4]. Xia F, Wang H, Xiao D, Dubey M, Ramasubramaniam A. Two-dimensional material nanophotonics. *Nature Photonics* **8**, 899-907, 2014.

[5]. Buscema M. Photodetection with novel materials colloidal quantum dots nanoribbons and layered materials. 2015.

[6]. Konstantatos G, Sargent EH. Nanostructured materials for photon detection. *Nat Nanotechnol* **5**, 391-400, 2010.

[7]. Kato K, Hata S, Kawano K, Kozen A. Design of Ultrawide-Band, High-Sensitivity pin Protodetectors (Special Issue on Optical/Microwave Interaction Devices, Circuits and Systems). *IEICE transactions on electronics* **76**, 214-221, 1993.

[8]. Manga KK, Wang S, Jaiswal M, Bao Q, Loh KP. High-gain graphene-titanium oxide photoconductor made from inkjet printable ionic solution. *Adv Mater* **22**, 5265-5270, 2010.

[9]. Sze SM, Ng KK. *Physics of semiconductor devices*. John wiley & sons (2006).

[10]. Hartmann JM, Abbadie A, Papon AM, Holliger P, Rolland G, Billon T, Fédéli JM, Rouvière M, Vivien L, Laval S. Reduced pressure–chemical vapor

deposition of Ge thick layers on Si(001) for 1.3–1.55-μm photodetection. *Journal of Applied Physics* **95**, 5905-5913, 2004.

[11]. Humamatsu Photonics K. Characteristics and use of Infrared Detectors. *Hamamatsu City*, 2011.

[12]. Barnes WL, Dereux A, Ebbesen TW. Surface plasmon subwavelength optics. *Nature* **424**, 824-830, 2003.

[13]. Koppens FH, Chang DE, Garcia de Abajo FJ. Graphene plasmonics: a platform for strong light-matter interactions. *Nano Lett* **11**, 3370-3377, 2011.

[14]. Ozbay E. Plasmonics: merging photonics and electronics at nanoscale dimensions. *science* **311**, 189-193, 2006.

[15]. Castro Neto AH, Guinea F, Peres NMR, Novoselov KS, Geim AK. The electronic properties of graphene. *Reviews of Modern Physics* **81**, 109-162, 2009.

[16]. Bolotin KI, Sikes KJ, Jiang Z, Klima M, Fudenberg G, Hone J, Kim P, Stormer HL. Ultrahigh electron mobility in suspended graphene. *Solid State Communications* **146**, 351-355, 2008.

[17]. Bonaccorso F, Sun Z, Hasan T, Ferrari AC. Graphene photonics and optoelectronics. *Nature Photonics* **4**, 611-622, 2010.

[18]. Geim AK, Novoselov KS. The rise of graphene. In: *Nanoscience and Technology: A Collection of Reviews from Nature Journals* (ed^(eds). World Scientific (2010).

[19]. Gusynin VP, Sharapov SG, Carbotte JP. Magneto-optical conductivity in graphene. *Journal of Physics: Condensed Matter* **19**, 026222, 2007.

[20]. Horng J, Chen C-F, Geng B, Girit C, Zhang Y, Hao Z, Bechtel HA, Martin M, Zettl A, Crommie MF, Shen YR, Wang F. Drude conductivity of Dirac fermions in graphene. *Physical Review B* **83**, 2011.

[21]. Kuzmenko AB, van Heumen E, Carbone F, van der Marel D. Universal Optical Conductance of Graphite. *Physical Review Letters* **100**, 2008.

[22]. Nair RR, Blake P, Grigorenko AN, Novoselov KS, Booth TJ, Stauber T, Peres NM, Geim AK. Fine structure constant defines visual transparency of graphene. *Science* **320**, 1308, 2008.

[23]. Li ZQ, Henriksen EA, Jiang Z, Hao Z, Martin MC, Kim P, Stormer HL, Basov DN. Dirac charge dynamics in graphene by infrared spectroscopy. *Nature Physics* **4**, 532-535, 2008.

[24]. Wang F, Zhang Y, Tian C, Girit C, Zettl A, Crommie M, Shen YR. Gate-variable optical transitions in graphene. *Science* **320**, 206-209, 2008.

[25]. Yang L, Deslippe J, Park C-H, Cohen ML, Louie SG. Excitonic Effects on the Optical Response of Graphene and Bilayer Graphene. *Physical Review Letters* **103**, 2009.

[26]. Peres N. Colloquium: The transport properties of graphene: An introduction. *Reviews of modern physics* **82**, 2673, 2010.

[27]. Mak KF, Ju L, Wang F, Heinz TF. Optical spectroscopy of graphene: from the far infrared to the ultraviolet. *Solid State Communications* **152**, 1341-1349, 2012.

[28]. Peplow M. Graphene: The quest for supercarbon. *Nature* **503**, 327-329, 2013.

[29]. Son Y-W, Cohen ML, Louie SG. Energy Gaps in Graphene Nanoribbons. *Physical Review Letters* **97**, 2006.

[30]. Bai J, Zhong X, Jiang S, Huang Y, Duan X. Graphene nanomesh. *Nat Nanotechnol* **5**, 190-194, 2010.

[31]. Oswald W, Wu Z. Energy gaps in graphene nanomeshes. *Physical Review B* **85**, 2012.

[32]. Dvorak M, Oswald W, Wu Z. Bandgap opening by patterning graphene. *Sci Rep* **3**, 2289, 2013.

[33]. Jablan M, Buljan H, Soljačić M. Plasmonics in graphene at infrared frequencies. *Physical Review B* **80**, 2009.

[34]. Jablan M, Buljan H, Soljačić M. Plasmonics in graphene at infrared frequencies. *Physical review B* **80**, 245435, 2009.

[35]. Fei Z, Andreev GO, Bao W, Zhang LM, A SM, Wang C, Stewart MK, Zhao Z, Dominguez G, Thiemens M, Fogler MM, Tauber MJ, Castro-Neto AH, Lau CN, Keilmann F, Basov DN. Infrared nanoscopy of dirac plasmons at the graphene-SiO(2) interface. *Nano Lett* **11**, 4701-4705, 2011.

[36]. Fei Z, Rodin AS, Andreev GO, Bao W, McLeod AS, Wagner M, Zhang LM, Zhao Z, Thiemens M, Dominguez G, Fogler MM, Castro Neto AH, Lau CN, Keilmann F, Basov DN. Gate-tuning of graphene plasmons revealed by infrared nano-imaging. *Nature* **487**, 82-85, 2012.

[37]. Chen J, Badioli M, Alonso-Gonzalez P, Thongrattanasiri S, Huth F, Osmond J, Spasenovic M, Centeno A, Pesquera A, Godignon P, Elorza AZ, Camara N, Garcia de Abajo FJ, Hillenbrand R, Koppens FH. Optical nano-imaging of gate-tunable graphene plasmons. *Nature* **487**, 77-81, 2012.

[38]. Koppens FH, Mueller T, Avouris P, Ferrari AC, Vitiello MS, Polini M. Photodetectors based on graphene, other two-dimensional materials and hybrid systems. *Nat Nanotechnol* **9**, 780-793, 2014.

[39]. Mueller T, Xia F, Avouris P. Graphene photodetectors for high-speed optical communications. *Nature Photonics* **4**, 297-301, 2010.

[40]. Gan X, Shiue R-J, Gao Y, Meric I, Heinz TF, Shepard K, Hone J, Assefa S, Englund D. Chip-integrated ultrafast graphene photodetector with high responsivity. *Nature Photonics* **7**, 883-887, 2013.

[41]. Peters EC, Lee EJH, Burghard M, Kern K. Gate dependent photocurrents at a graphene p-n junction. *Applied Physics Letters* **97**, 193102, 2010.

[42]. Rao G, Freitag M, Chiu HY, Sundaram RS, Avouris P. Raman and photocurrent imaging of electrical stress-induced p-n junctions in graphene. *ACS Nano* **5**, 5848-5854, 2011.

[43]. Mueller T, Xia F, Freitag M, Tsang J, Avouris P. Role of contacts in graphene transistors: A scanning photocurrent study. *Physical Review B* **79**, 2009.

[44]. Xia F, Mueller T, Lin YM, Valdes-Garcia A, Avouris P. Ultrafast graphene photodetector. *Nat Nanotechnol* **4**, 839-843, 2009.

[45]. Urich A, Unterrainer K, Mueller T. Intrinsic response time of graphene photodetectors. *Nano Lett* **11**, 2804-2808, 2011.

[46]. Sun D, Wu Z-K, Divin C, Li X, Berger C, de Heer WA, First PN, Norris TB. Ultrafast Relaxation of Excited Dirac Fermions in Epitaxial Graphene Using Optical Differential Transmission Spectroscopy. *Physical Review Letters* **101**, 2008.

[47]. Xu X, Gabor NM, Alden JS, van der Zande AM, McEuen PL. Photo-thermoelectric effect at a graphene interface junction. *Nano Lett* **10**, 562-566, 2010.

[48]. Yuan H, Liu X, Afshinmanesh F, Li W, Xu G, Sun J, Lian B, Curto AG, Ye G, Hikita Y, Shen Z, Zhang SC, Chen X, Brongersma M, Hwang HY, Cui Y. Polarization-sensitive broadband photodetector using a black phosphorus vertical p-n junction. *Nat Nanotechnol*, 2015.

[49]. Lopez-Sanchez O, Lembke D, Kayci M, Radenovic A, Kis A. Ultrasensitive photodetectors based on monolayer MoS2. *Nat Nanotechnol* **8**, 497-501, 2013.

[50]. Youngblood N, Chen C, Koester SJ, Li M. Waveguide-integrated black phosphorus photodetector with high responsivity and low dark current. *Nature Photonics*, 2015.

[51]. Britnell L, Gorbachev RV, Jalil R, Belle BD, Schedin F, Mishchenko A, Georgiou T, Katsnelson MI, Eaves L, Morozov SV, Peres NM, Leist J, Geim AK, Novoselov KS, Ponomarenko LA. Field-effect tunneling transistor based on vertical graphene heterostructures. *Science* **335**, 947-950, 2012.

[52]. Britnell L, Ribeiro RM, Eckmann A, Jalil R, Belle BD, Mishchenko A, Kim YJ, Gorbachev RV, Georgiou T, Morozov SV, Grigorenko AN, Geim AK, Casiraghi C, Castro Neto AH, Novoselov KS. Strong light-matter interactions in heterostructures of atomically thin films. *Science* **340**, 1311-1314, 2013.

[53]. Geim AK, Grigorieva IV. Van der Waals heterostructures. *Nature* **499**, 419-425, 2013.

[54]. Roy K, Padmanabhan M, Goswami S, Sai TP, Ramalingam G, Raghavan S, Ghosh A. Graphene-MoS2 hybrid structures for multifunctional photoresponsive memory devices. *Nat Nanotechnol* **8**, 826-830, 2013.

[55]. Yu WJ, Liu Y, Zhou H, Yin A, Li Z, Huang Y, Duan X. Highly efficient gate-tunable photocurrent generation in vertical heterostructures of layered materials. *Nat Nanotechnol* **8**, 952-958, 2013.

[56]. Xia F, Mueller T, Golizadeh-Mojarad R, Freitag M, Lin YM, Tsang J, Perebeinos V, Avouris P. Photocurrent imaging and efficient photon detection in a graphene transistor. *Nano Lett* **9**, 1039-1044, 2009.

[57]. Park J, Ahn YH, Ruiz-Vargas C. Imaging of photocurrent generation and collection in single-layer graphene. *Nano Lett* **9**, 1742-1746, 2009.

[58]. Lee EJ, Balasubramanian K, Weitz RT, Burghard M, Kern K. Contact and edge effects in graphene devices. *Nat Nanotechnol* **3**, 486-490, 2008.

[59]. Gabor NM, Song JC, Ma Q, Nair NL, Taychatanapat T, Watanabe K, Taniguchi T, Levitov LS, Jarillo-Herrero P. Hot carrier-assisted intrinsic photoresponse in graphene. *Science* **334**, 648-652, 2011.

[60]. Freitag M, Low T, Avouris P. Increased responsivity of suspended graphene photodetectors. *Nano Lett* **13**, 1644-1648, 2013.

[61]. Sun Z, Liu Z, Li J, Tai GA, Lau SP, Yan F. Infrared photodetectors based on CVD-grown graphene and PbS quantum dots with ultrahigh responsivity. *Adv Mater* **24**, 5878-5883, 2012.

[62]. Zhang BY, Liu T, Meng B, Li X, Liang G, Hu X, Wang QJ. Broadband high photoresponse from pure monolayer graphene photodetector. *Nat Commun* **4**, 1811, 2013.

[63]. Konstantatos G, Badioli M, Gaudreau L, Osmond J, Bernechea M, De Arquer FPG, Gatti F, Koppens FH. Hybrid graphene–quantum dot phototransistors with ultrahigh gain. *Nature nanotechnology* **7**, 363, 2012.

[64]. Patil V, Capone A, Strauf S, Yang EH. Improved photoresponse with enhanced photoelectric contribution in fully suspended graphene photodetectors. *Sci Rep* **3**, 2791, 2013.

[65]. Prechtel L, Song L, Schuh D, Ajayan P, Wegscheider W, Holleitner AW. Time-resolved ultrafast photocurrents and terahertz generation in freely suspended graphene. *Nat Commun* **3**, 646, 2012.

[66]. Pospischil A, Humer M, Furchi MM, Bachmann D, Guider R, Fromherz T, Mueller T. CMOS-compatible graphene photodetector covering all optical communication bands. *Nature Photonics* **7**, 892-896, 2013.

[67]. Wang XM, Cheng ZZ, Xu K, Tsang HK, Xu JB. High-responsivity graphene/silicon-heterostructure waveguide photodetectors. *Nature Photonics* **7**, 888-891, 2013.

[68]. Engel M, Steiner M, Lombardo A, Ferrari AC, Lohneysen HV, Avouris P, Krupke R. Light-matter interaction in a microcavity-controlled graphene transistor. *Nat Commun* **3**, 906, 2012.

[69]. Ferreira A, Peres NMR, Ribeiro RM, Stauber T. Graphene-based photodetector with two cavities. *Physical Review B* **85**, 2012.

[70]. Furchi M, Urich A, Pospischil A, Lilley G, Unterrainer K, Detz H, Klang P, Andrews AM, Schrenk W, Strasser G, Mueller T. Microcavity-integrated graphene photodetector. *Nano Lett* **12**, 2773-2777, 2012.

[71]. Gan X, Mak KF, Gao Y, You Y, Hatami F, Hone J, Heinz TF, Englund D. Strong enhancement of light-matter interaction in graphene coupled to a photonic crystal nanocavity. *Nano Lett* **12**, 5626-5631, 2012.

[72]. Liu Y, Cheng R, Liao L, Zhou H, Bai J, Liu G, Liu L, Huang Y, Duan X. Plasmon resonance enhanced multicolour photodetection by graphene. *Nat Commun* **2**, 579, 2011.

[73]. Shi SF, Xu X, Ralph DC, McEuen PL. Plasmon resonance in individual nanogap electrodes studied using graphene nanoconstrictions as photodetectors. *Nano Lett* **11**, 1814-1818, 2011.

[74]. Fang Z, Liu Z, Wang Y, Ajayan PM, Nordlander P, Halas NJ. Graphene-antenna sandwich photodetector. *Nano letters* **12**, 3808-3813, 2012.

[75]. Youngblood N, Anugrah Y, Ma R, Koester SJ, Li M. Multifunctional graphene optical modulator and photodetector integrated on silicon waveguides. *Nano letters* **14**, 2741-2746, 2014.

[76]. Wang X, Cheng Z, Xu K, Tsang HK, Xu J-B. High-responsivity graphene/silicon-heterostructure waveguide photodetectors. *Nature Photonics* **7**, 888, 2013.

[77]. Majumdar A, Kim J, Vuckovic J, Wang F. Electrical control of silicon photonic crystal cavity by graphene. *Nano letters* **13**, 515-518, 2013.

[78]. Luo LB, Zou YF, Ge CW, Zheng K, Wang DD, Lu R, Zhang TF, Yu YQ, Guo ZY. A Surface Plasmon Enhanced Near-Infrared Nanophotodetector. *Advanced Optical Materials* **4**, 763-771, 2016.

[79]. Ward DR, Hüser F, Pauly F, Cuevas JC, Natelson D. Optical rectification and field enhancement in a plasmonic nanogap. *Nature nanotechnology* **5**, 732, 2010.

[80]. Echtermeyer T, Britnell L, Jasnos P, Lombardo A, Gorbachev R, Grigorenko A, Geim A, Ferrari AC, Novoselov K. Strong plasmonic enhancement of photovoltage in graphene. *Nature communications* **2**, 458, 2011.

[81]. Echtermeyer T, Milana S, Sassi U, Eiden A, Wu M, Lidorikis E, Ferrari AC. Surface plasmon polariton graphene photodetectors. *Nano Letters* **16**, 8-20, 2015.

[82]. Nian Q, Gao L, Hu Y, Deng B, Tang J, Cheng GJ. Graphene/PbS-Quantum Dots/Graphene Sandwich Structures Enabled by Laser Shock Imprinting for High Performance Photodetectors. *ACS applied materials & interfaces* **9**, 44715-44723, 2017.

[83]. Nikitskiy I, Goossens S, Kufer D, Lasanta T, Navickaite G, Koppens FH, Konstantatos G. Integrating an electrically active colloidal quantum dot photodiode with a graphene phototransistor. *Nature communications* **7**, 11954, 2016.

[84]. Che Y, Zhang Y, Cao X, Zhang H, Song X, Cao M, Yu Y, Dai H, Yang J, Zhang G. Ambipolar Graphene–Quantum Dot Hybrid Vertical Photodetector with a Graphene Electrode. *ACS applied materials & interfaces* **9**, 32001-32007, 2017.

[85]. Wu J, Lu Y, Feng S, Wu Z, Lin S, Hao Z, Yao T, Li X, Zhu H, Lin S. The Interaction between Quantum Dots and Graphene: The Applications in Graphene-Based Solar Cells and Photodetectors. *Advanced Functional Materials* **28**, 1804712, 2018.

[86]. Yan H, Xia F, Zhu W, Freitag M, Dimitrakopoulos C, Bol AA, Tulevski G, Avouris P. Infrared spectroscopy of wafer-scale graphene. *ACS Nano* **5**, 9854-9860, 2011.

[87]. Cai J, Ruffieux P, Jaafar R, Bieri M, Braun T, Blankenburg S, Muoth M, Seitsonen AP, Saleh M, Feng X. Atomically precise bottom-up fabrication of graphene nanoribbons. *Nature* **466**, 470, 2010.

[88]. Wang X, Dai H. Etching and narrowing of graphene from the edges. *Nature chemistry* **2**, 661, 2010.

[89]. Vo TH, Shekhirev M, Kunkel DA, Morton MD, Berglund E, Kong L, Wilson PM, Dowben PA, Enders A, Sinitskii A. Large-scale solution synthesis of narrow graphene nanoribbons. *Nature communications* **5**, 3189, 2014.

[90]. Abramova V, Slesarev AS, Tour JM. Meniscus-mask lithography for narrow graphene nanoribbons. *ACS nano* **7**, 6894-6898, 2013.

[91]. Kosynkin DV, Lu W, Sinitskii A, Pera G, Sun Z, Tour JM. Highly conductive graphene nanoribbons by longitudinal splitting of carbon nanotubes using potassium vapor. *Acs Nano* **5**, 968-974, 2011.

[92]. Li X, Rui M, Song J, Shen Z, Zeng H. Carbon and graphene quantum dots for optoelectronic and energy devices: a review. *Advanced Functional Materials* **25**, 4929-4947, 2015.

[93]. Chen W, Lv G, Hu W, Li D, Chen S, Dai Z. Synthesis and applications of graphene quantum dots: A review. *Nanotechnology Reviews* **7**, 157-185, 2018.

[94]. Yang J, Ma M, Li L, Zhang Y, Huang W, Dong X. Graphene nanomesh: new versatile materials. *Nanoscale* **6**, 13301-13313, 2014.

[95]. Chen Z, Lin Y-M, Rooks MJ, Avouris P. Graphene nano-ribbon electronics. *Physica E: Low-dimensional Systems and Nanostructures* **40**, 228-232, 2007.

[96]. Han MY, Özyilmaz B, Zhang Y, Kim P. Energy Band-Gap Engineering of Graphene Nanoribbons. *Physical Review Letters* **98**, 2007.

[97]. Liao AD, Wu JZ, Wang X, Tahy K, Jena D, Dai H, Pop E. Thermally Limited Current Carrying Ability of Graphene Nanoribbons. *Physical Review Letters* **106**, 2011.

[98]. Ryzhii V, Mitin V, Ryzhii M, Ryabova N, Otsuji T. Device Model for Graphene Nanoribbon Phototransistor. *Applied Physics Express* **1**, 063002, 2008.

[99]. Chitara B, Panchakarla LS, Krupanidhi SB, Rao CN. Infrared photodetectors based on reduced graphene oxide and graphene nanoribbons. *Adv Mater* **23**, 5419-5424, 2011.

[100]. Freitag M, Low T, Zhu W, Yan H, Xia F, Avouris P. Photocurrent in graphene harnessed by tunable intrinsic plasmons. *Nat Commun* **4**, 1951, 2013.

[101]. Mihalache I, Radoi A, Pascu R, Romanitan C, Vasile E, Kusko M. Engineering graphene quantum dots for enhanced ultraviolet and visible light p-Si

nanowire-based photodetector. *ACS applied materials & interfaces* **9**, 29234-29247, 2017.

[102]. Kim CO, Hwang SW, Kim S, Shin DH, Kang SS, Kim JM, Jang CW, Kim JH, Lee KW, Choi S-H. High-performance graphene-quantum-dot photodetectors. *Scientific reports* **4**, 5603, 2014.

[103]. Liu X, Liu N, Liu M, Tao Z, Kuang W, Ji X, Chen J, Lei W, Dai Q, Li C, Li X, Nathan A. Graphene nanomesh photodetector with effective charge tunnelling from quantum dots. *Nanoscale* **7**, 4242-4249, 2015.

[104]. Liu W, Wang ZF, Shi QW, Yang J, Liu F. Band-gap scaling of graphene nanohole superlattices. *Physical Review B* **80**, 2009.

[105]. Kim M, Safron NS, Han E, Arnold MS, Gopalan P. Fabrication and characterization of large-area, semiconducting nanoperforated graphene materials. *Nano Lett* **10**, 1125-1131, 2010.

[106]. Kazemi A, He X, Alaie S, Ghasemi J, Dawson NM, Cavallo F, Habteyes TG, Brueck SR, Krishna S. Large-Area Semiconducting Graphene Nanomesh Tailored by Interferometric Lithography. *Sci Rep* **5**, 11463, 2015.

[107]. Mangadlao JD, de Leon AC, Felipe MJ, Advincula RC. Electrochemical fabrication of graphene nanomesh via colloidal templating. *Chem Commun (Camb)* **51**, 7629-7632, 2015.

[108]. Nikitin AY, Guinea F, García-Vidal FJ, Martín-Moreno L. Edge and waveguide terahertz surface plasmon modes in graphene microribbons. *Physical Review B* **84**, 2011.

[109]. Christensen J, Manjavacas A, Thongrattanasiri S, Koppens FH, de Abajo FJ. Graphene plasmon waveguiding and hybridization in individual and paired nanoribbons. *ACS Nano* **6**, 431-440, 2012.

[110]. Brar VW, Jang MS, Sherrott M, Lopez JJ, Atwater HA. Highly confined tunable mid-infrared plasmonics in graphene nanoresonators. *Nano Lett* **13**, 2541-2547, 2013.

[111]. Fang Z, Thongrattanasiri S, Schlather A, Liu Z, Ma L, Wang Y, Ajayan PM, Nordlander P, Halas NJ, Garcia de Abajo FJ. Gated tunability and hybridization of localized plasmons in nanostructured graphene. *ACS Nano* **7**, 2388-2395, 2013.

[112]. Yan H, Xia F, Li Z, Avouris P. Plasmonics of coupled graphene micro-structures. *New Journal of Physics* **14**, 125001, 2012.

[113]. Yan H, Li Z, Li X, Zhu W, Avouris P, Xia F. Infrared spectroscopy of tunable Dirac terahertz magneto-plasmons in graphene. *Nano letters* **12**, 3766-3771, 2012.

[114]. Fang Z, Thongrattanasiri S, Schlather A, Liu Z, Ma L, Wang Y, Ajayan PM, Nordlander P, Halas NJ, García de Abajo FJ. Gated tunability and hybridization of localized plasmons in nanostructured graphene. *ACS nano* **7**, 2388-2395, 2013.

[115]. Yan H, Li X, Chandra B, Tulevski G, Wu Y, Freitag M, Zhu W, Avouris P, Xia F. Tunable infrared plasmonic devices using graphene/insulator stacks. *Nature nanotechnology* **7**, 330, 2012.

[116]. Thongrattanasiri S, Manjavacas A, Garcia de Abajo FJ. Quantum finite-size effects in graphene plasmons. *ACS Nano* **6**, 1766-1775, 2012.

[117]. Yan H, Li X, Chandra B, Tulevski G, Wu Y, Freitag M, Zhu W, Avouris P, Xia F. Tunable infrared plasmonic devices using graphene/insulator stacks. *Nat Nanotechnol* **7**, 330-334, 2012.

[118]. Grigorenko AN, Polini M, Novoselov KS. Graphene plasmonics. *Nature Photonics* **6**, 749-758, 2012.

[119]. Partoens B, Peeters F. From graphene to graphite: Electronic structure around the K point. *Physical Review B* **74**, 075404, 2006.

[120]. Nevius M, Conrad M, Wang F, Celis A, Nair M, Taleb-Ibrahimi A, Tejeda A, Conrad E. Semiconducting graphene from highly ordered substrate interactions. *Physical review letters* **115**, 136802, 2015.

[121]. Giovannetti G, Khomyakov PA, Brocks G, Kelly PJ, Van Den Brink J. Substrate-induced band gap in graphene on hexagonal boron nitride: Ab initio density functional calculations. *Physical Review B* **76**, 073103, 2007.

[122]. Zhou SY, Gweon G-H, Fedorov A, First P, de, De Heer W, Lee D-H, Guinea F, Neto AC, Lanzara A. Substrate-induced bandgap opening in epitaxial graphene. *Nature materials* **6**, 770, 2007.

[123]. Ohta T, Bostwick A, Seyller T, Horn K, Rotenberg E. Controlling the electronic structure of bilayer graphene. *Science* **313**, 951-954, 2006.

[124]. Zhang Y, Tang TT, Girit C, Hao Z, Martin MC, Zettl A, Crommie MF, Shen YR, Wang F. Direct observation of a widely tunable bandgap in bilayer graphene. *Nature* **459**, 820-823, 2009.

[125]. McCann E. Asymmetry gap in the electronic band structure of bilayer graphene. *Physical Review B* **74**, 2006.

[126]. Castro EV, Novoselov KS, Morozov SV, Peres NM, dos Santos JM, Nilsson J, Guinea F, Geim AK, Neto AH. Biased bilayer graphene: semiconductor with a gap tunable by the electric field effect. *Phys Rev Lett* **99**, 216802, 2007.

[127]. Taychatanapat T, Jarillo-Herrero P. Electronic transport in dual-gated bilayer graphene at large displacement fields. *Phys Rev Lett* **105**, 166601, 2010.

[128]. Mak KF, Sfeir MY, Misewich JA, Heinz TF. The evolution of electronic structure in few-layer graphene revealed by optical spectroscopy. *Proc Natl Acad Sci U S A* **107**, 14999-15004, 2010.

[129]. Son YW, Cohen ML, Louie SG. Energy gaps in graphene nanoribbons. *Phys Rev Lett* **97**, 216803, 2006.

[130]. Han MY, Ozyilmaz B, Zhang Y, Kim P. Energy band-gap engineering of graphene nanoribbons. *Phys Rev Lett* **98**, 206805, 2007.

[131]. Lopata K, Thorpe R, Pistinner S, Duan X, Neuhauser D. Graphene nanomeshes: Onset of conduction band gaps. *Chemical Physics Letters* **498**, 334-337, 2010.

[132]. Ouyang F, Peng S, Liu Z, Liu Z. Bandgap opening in graphene antidot lattices: the missing half. *ACS Nano* **5**, 4023-4030, 2011.

[133]. Yeung KY, Chee J, Yoon H, Song Y, Kong J, Ham D. Far-infrared graphene plasmonic crystals for plasmonic band engineering. *Nano Lett* **14**, 2479-2484, 2014.

[134]. Pedersen TG, Flindt C, Pedersen J, Mortensen NA, Jauho AP, Pedersen K. Graphene antidot lattices: designed defects and spin qubits. *Phys Rev Lett* **100**, 136804, 2008.

[135]. Fedotov VA, Schwanecke AS, Zheludev NI, Khardikov VV, Prosvirnin SL. Asymmetric Transmission of Light and Enantiomerically Sensitive Plasmon Resonance in Planar Chiral Nanostructures. *Nano Letters* **7**, 1996-1999, 2007.

[136]. Yang S, Chen W, Nelson RL, Zhan Q. Miniature circular polarization analyzer with spiral plasmonic lens. *Opt Lett* **34**, 3047-3049, 2009.

[137]. Zhukovsky SV, Kremers C, Chigrin DN. Plasmonic rod dimers as elementary planar chiral meta-atoms. *Opt Lett* **36**, 2278-2280, 2011.

[138]. Konishi K, Bai B, Toya Y, Turunen J, Svirko YP, Kuwata-Gonokami M. Surface-plasmon enhanced optical activity in two-dimensional metal chiral networks. *Opt Lett* **37**, 4446-4448, 2012.

[139]. Zhukovsky SV, Kremers C, Chigrin DN. Plasmonic rod dimers as elementary planar chiral meta-atoms. *Optics letters* **36**, 2278-2280, 2011.

[140]. Yang S, Chen W, Nelson RL, Zhan Q. Miniature circular polarization analyzer with spiral plasmonic lens. *Optics letters* **34**, 3047-3049, 2009.

[141]. Fedotov V, Schwanecke A, Zheludev N, Khardikov V, Prosvirnin S. Asymmetric transmission of light and enantiomerically sensitive plasmon resonance in planar chiral nanostructures. *Nano Letters* **7**, 1996-1999, 2007.

[142]. Zu S, Bao Y, Fang Z. Planar plasmonic chiral nanostructures. *Nanoscale* **8**, 3900-3905, 2016.

[143]. Konishi K, Bai B, Toya Y, Turunen J, Svirko YP, Kuwata-Gonokami M. Surface-plasmon enhanced optical activity in two-dimensional metal chiral networks. *Optics letters* **37**, 4446-4448, 2012.

[144]. Arteaga O, Sancho-Parramon J, Nichols S, Maoz BM, Canillas A, Bosch S, Markovich G, Kahr B. Relation between 2D/3D chirality and the appearance of chiroptical effects in real nanostructures. *Optics express* **24**, 2242-2252, 2016.

[145]. Li W, Coppens ZJ, Besteiro LV, Wang W, Govorov AO, Valentine J. Circularly polarized light detection with hot electrons in chiral plasmonic metamaterials. *Nature communications* **6**, 8379, 2015.

[146]. Zu S, Bao Y, Fang Z. Planar plasmonic chiral nanostructures. *Nanoscale* **8**, 3900-3905, 2016.

[147]. Khanikaev AB, Arju N, Fan Z, Purtseladze D, Lu F, Lee J, Sarriugarte P, Schnell M, Hillenbrand R, Belkin MA, Shvets G. Experimental demonstration of the microscopic origin of circular dichroism in two-dimensional metamaterials. *Nat Commun* **7**, 12045, 2016.

[148]. Khanikaev A, Arju N, Fan Z, Purtseladze D, Lu F, Lee J, Sarriugarte P, Schnell M, Hillenbrand R, Belkin M. Experimental demonstration of the microscopic origin of circular dichroism in two-dimensional metamaterials. *Nature communications* **7**, 12045, 2016.

[149]. Xia F, Mueller T, Golizadeh-Mojarad R, Freitag M, Lin Y-m, Tsang J, Perebeinos V, Avouris P. Photocurrent imaging and efficient photon detection in a graphene transistor. *Nano letters* **9**, 1039-1044, 2009.

[150]. Novoselov K, Jiang D, Schedin F, Booth T, Khotkevich V, Morozov S, Geim A. Two-dimensional atomic crystals. *Proceedings of the National Academy of Sciences* **102**, 10451-10453, 2005.

[151]. Novoselov KS, Geim AK, Morozov SV, Jiang D, Zhang Y, Dubonos SV, Grigorieva IV, Firsov AA. Electric field effect in atomically thin carbon films. *Science* **306**, 666-669, 2004.

[152]. Li X, Cai W, An J, Kim S, Nah J, Yang D, Piner R, Velamakanni A, Jung I, Tutuc E. Large-area synthesis of high-quality and uniform graphene films on copper foils. *science* **324**, 1312-1314, 2009.

[153]. Kim KS, Zhao Y, Jang H, Lee SY, Kim JM, Kim KS, Ahn J-H, Kim P, Choi J-Y, Hong BH. Large-scale pattern growth of graphene films for stretchable transparent electrodes. *nature* **457**, 706, 2009.

[154]. Hass J, Feng R, Li T, Li X, Zong Z, De Heer W, First P, Conrad E, Jeffrey C, Berger C. Highly ordered graphene for two dimensional electronics. *Applied Physics Letters* **89**, 143106, 2006.

[155]. Berger C, Song Z, Li T, Li X, Ogbazghi AY, Feng R, Dai Z, Marchenkov AN, Conrad EH, First PN. Ultrathin epitaxial graphite: 2D electron gas properties and a route toward graphene-based nanoelectronics. *The Journal of Physical Chemistry B* **108**, 19912-19916, 2004.

[156]. Ju L, Geng B, Horng J, Girit C, Martin M, Hao Z, Bechtel HA, Liang X, Zettl A, Shen YR, Wang F. Graphene plasmonics for tunable terahertz metamaterials. *Nat Nanotechnol* **6**, 630-634, 2011.

[157]. Yan H, Low T, Zhu W, Wu Y, Freitag M, Li X, Guinea F, Avouris P, Xia F. Damping pathways of mid-infrared plasmons in graphene nanostructures. *Nature Photonics* **7**, 394, 2013.

[158]. Rodrigo D, Limaj O, Janner D, Etezadi D, De Abajo FJG, Pruneri V, Altug H. Mid-infrared plasmonic biosensing with graphene. *Science* **349**, 165-168, 2015.

[159]. Lee B, Chen Y, Duerr F, Mastrogiovanni D, Garfunkel E, Andrei E, Podzorov V. Modification of electronic properties of graphene with self-assembled monolayers. *Nano letters* **10**, 2427-2432, 2010.

[160]. Chen J-H, Jang C, Xiao S, Ishigami M, Fuhrer MS. Intrinsic and extrinsic performance limits of graphene devices on SiO_2. *Nature nanotechnology* **3**, 206, 2008.

[161]. Kotov VN, Uchoa B, Pereira VM, Guinea F, Neto AC. Electron-electron interactions in graphene: Current status and perspectives. *Reviews of Modern Physics* **84**, 1067, 2012.

[162]. Avouris P. Graphene: electronic and photonic properties and devices. *Nano letters* **10**, 4285-4294, 2010.

[163]. Li X, Colombo L, Ruoff RS. Synthesis of graphene films on copper foils by chemical vapor deposition. *Advanced Materials* **28**, 6247-6252, 2016.

[164]. Ferrari AC, Meyer J, Scardaci V, Casiraghi C, Lazzeri M, Mauri F, Piscanec S, Jiang D, Novoselov K, Roth S. Raman spectrum of graphene and graphene layers. *Physical review letters* **97**, 187401, 2006.

[165]. Sun Z, Yan Z, Yao J, Beitler E, Zhu Y, Tour JM. Growth of graphene from solid carbon sources. *Nature* **468**, 549, 2010.

[166]. Berciaud S, Ryu S, Brus LE, Heinz TF. Probing the intrinsic properties of exfoliated graphene: Raman spectroscopy of free-standing monolayers. *Nano letters* **9**, 346-352, 2008.

[167]. Ferrari AC, Basko DM. Raman spectroscopy as a versatile tool for studying the properties of graphene. *Nature nanotechnology* **8**, 235, 2013.

[168]. Ferrari AC. Raman spectroscopy of graphene and graphite: disorder, electron–phonon coupling, doping and nonadiabatic effects. *Solid state communications* **143**, 47-57, 2007.

Appendix A Conferences and publications

Conferences

- 2018 AIP Congress , Perth, Western Australia, Oral presentation
- 2018 FIO conference, Washington, District of Columbia, USA, Oral presentation
- 2017 RPGR conference, Grand Copthorne Waterfront Hotel, Singapore, poster presentation
- 2017 Annual CUDOS workshop, Sydney, Kooindah Water Resort, New South Wales, Poster presentation
- 2017 Conference, Beyond Research - Pathways to Impact Conference, Melbourne, Melbourne Convention and Exhibition Centre. Attendee
- 2016 Conference, 5th International Symposium on Graphene Devices (ISGD-5), Brisbane, Griffith university, oral presentation
- 2016 Conference, IONS-KOALA 2016, Melbourne, Monash University, oral presentations
- 2016 Workshop, Annual CUDOS Workshop 2016, Sydney, Kooindah Waters Resort, New South Wales. Poster presentation
- 2015 Conference, IONS-KOALA 2014, Auckland, University of Auckland Poster

Conference paper

Jingyang Peng, Bebjamin P. Cumming, Min Gu, MIR spin angular momentum detection by a chiral graphene plasmonic nanostructure, Frontiers in Optics, paper FW5E. 4

Journal articles

Direct detection of photon spin angular momentum by a chiral graphene mid-infrared photodetector; J Peng, BP Cumming, M Gu; Optics letters 44 (12), 2998-3001